

Xe-129 NMR Study on Xenon Monolayers and Thin Films Adsorbed on Single Crystal Metals and Carbonaceous Ad-Layers

Dissertation

Presented in Partial Fulfillment
of the Requirements for the Degree of

Doctor of Natural Sciences
(Dr. rer. nat.)

Submitted to the Faculty of Physics
Philipps-University Marburg

by

Lars P. Kraft

from
Gießen

Marburg/Lahn, 2018

Vom Fachbereich Physik der Philipps-Universität als Dissertation
angenommen am: 19.11.2018
Erstgutachter: Prof. Dr. Heinz J. Jänsch
Zweitgutachter: Prof. Dr. Gregor Witte
Tag der mündlichen Prüfung: 22.11.2018
Hochschulkennziffer 1180

Abstract

The essential core of this work is the study on xenon monolayers adsorbed on defined surfaces of single crystal metals and carbonic cover layers by means of Nuclear Magnetic Resonance (NMR). ^{129}Xe is utilized as the probe nucleus because of its many excellent properties. First and foremost ^{129}Xe can readily be polarized far above the thermodynamic equilibrium, which is also referred to as hyperpolarization. The rise in polarization is connected with an increase of the NMR signal strength up to five orders of magnitude. Only by these means the signal of a monolayer, containing not more than 10^{15} atoms, is able to pass the detection threshold, corresponding to a signal from about 10^{20} nuclei in a solid, of common NMR spectrometers.

Furthermore xenon is a heavy noble gas that adsorbs on substrates at temperatures of about 80–90 K, without inducing chemical reactions. Nevertheless, the electron environment of the ^{129}Xe is perturbed which causes a sensitive change in the magnetic field at the nuclear site. Especially in the immediate vicinity of metals the effect is so strong that the NMR signals, also called spectral lines, are frequency shifted up to the order of 1000 parts per million (ppm). Therefore, xenon NMR is not only a non-invasive chemical analysis method but also a local probe.

Xenon NMR is performed on a Xe monolayer in contact with a copper single crystal with a surface oriented in the [100] direction. Two distinct and strong signals have been found. These lines are respectively shifted by 687 ppm and 772 ppm with respect to the xenon gas line. Hence, both shifts surpass clearly the typical physisorption range which means that ^{129}Xe is in contact with the metal electrons. Further the signal of the second layer is also made visible in the spectra showing a non metallic shift of 235 ppm.

Another NMR experiment is performed on a xenon monolayer adsorbed on a CO buffer layer deposited on Cu(100). An NMR line is revealed at 163 ppm.

^{129}Xe is also probed on graphene that has been created on an Ir(111) surface. Here, the presence of metallic electrons cannot be detected on basis of an extraordinary NMR line shift. In particular, the shift of the ^{129}Xe signal in the monolayer on graphene has been determined to 173 ppm.

For comparison xenon film surface layers are analyzed by NMR during their growth at substrate temperatures below 50 K. The results give information about the temporary configuration of the xenon atoms on the film surface and the corresponding line shifts. Two, thus far unknown, signals are found at 160 ppm and 240 ppm. Besides, the signal of the bulk at 320 ppm and the smooth film surface at 200 ppm are also visible in the spectra.

In addition, an order phenomenon within a xenon film is demonstrated on the basis of the ^{129}Xe NMR linewidth. By strongly diluting the ^{129}Xe with ^{132}Xe , all other solid effects on the linewidth are sufficiently diminished to reveal a heat induced structure change. The lowest temperature measured is 25 K. Starting from this temperature up to 45 K, the change is observed.

Kurzfassung

Der wesentliche Kern dieser Arbeit ist die Untersuchung von Xenonmonolagen, die auf definierten Oberflächen von einkristallinen Metallen und kohlenstoffhaltigen Deckschichten adsorbiert sind mit Methoden der Nuclear Magnetic Resonance (NMR). ^{129}Xe wird verwendet als Sondenkern wegen seiner vielen hervorragenden Eigenschaften. Vor allem kann ^{129}Xe mit Leichtigkeit weit über das thermische Gleichgewicht polarisiert werden, was auch Hyperpolarisieren genannt wird. Der Anstieg der Polarisierung ist verknüpft mit einer Erhöhung der NMR-Signalstärke von bis zu fünf Größenordnungen. Nur auf diesem Weg kann das Signal einer Monolage, welche nicht mehr als 10^{15} Atome beinhaltet, die Detektionsschwelle von gebräuchlichen NMR-Spektrometern, die dem Signal von etwa 10^{20} Atomkernen in einem Festkörper entspricht, überwinden.

Des Weiteren ist Xenon ein schweres Edelgas, das auf Substraten bei Temperaturen um 80 K adsorbiert, ohne chemische Reaktionen auszulösen. Trotzdem wird die elektronische Umgebung der ^{129}Xe gestört, was eine sensible Änderung des Magnetfeldes am Ort des Kerns verursacht. Besonders in der unmittelbaren Nähe von Metallen ist der Effekt so stark, dass das NMR-Signal, auch Spektrallinie genannt, in seiner Frequenz verschoben wird bis zu einer Größenordnung von 1000 parts per million (ppm). Daher ist die Xenon-NMR nicht nur eine nichtinvasive chemische Analysemethode, sondern auch eine lokale Sonde.

Xenon NMR wird durchgeführt an einer Xe-Monolage in Kontakt mit einem Kupfereinkristall mit einer Oberfläche, die in die [100] Richtung orientiert ist. Zwei unterscheidbare und starke Signale sind gefunden worden. Diese Linien sind um 687 ppm bzw. um 772 ppm bezüglich der Xenongaslinie verschoben. Damit überschreiten beide Verschiebungen klar den typischen Physisorptionsbereich, was bedeutet, dass das ^{129}Xe in Kontakt mit den Metallelektronen steht. Der Abstand zwischen den beiden Linien ist erklärbar durch den Aufenthalt der Xenonatome an zwei verschiedenartigen Adsorptionsplätzen. Desweiteren ist auch die Linie der zweiten Lage, die eine nichtmetallische Verschiebung um 235 ppm zeigt, in den Spektren sichtbar gemacht worden.

Ein weiteres NMR-Experiment wird durchgeführt an einer Xenonmonolage adsorbiert auf einer CO-Pufferschicht, die auf Cu(100) abgeschieden worden ist. Eine NMR-Linie zeigt sich bei 163 ppm.

^{129}Xe wird auch auf Graphen, das auf einer Ir(111) Oberfläche erzeugt wurde, sondiert. Hier kann die Anwesenheit von Metallelektronen nicht festgestellt werden anhand einer außergewöhnlichen NMR-Linienverschiebung. Insbesondere ist die Verschiebung des ^{129}Xe -Signals in der Monolage auf Graphen mit 173 ppm bestimmt worden.

Zum Vergleich werden Xenonfilmoberflächenlagen mit NMR analysiert während ihres Wachstums bei Substrattemperaturen unter 50 K. Die Ergebnisse geben Aufschluss über die temporäre Konfiguration der Xenonatome auf der Filmoberfläche und die entsprechenden Linienverschiebungen. Zwei bis dahin unbekannte Signale werden gefunden bei 160 ppm und 240 ppm. Im Übrigen sind auch die Signale des Festkörpers bei 320 ppm und der gleichmäßigen Oberfläche bei 200 ppm sichtbar in den Spektren.

Außerdem wird ein Ordnungsphänomen innerhalb eines Xenonfilms gezeigt anhand der ^{129}Xe -NMR-Linienbreite. Durch starke Verdünnung des ^{129}Xe mit ^{132}Xe werden alle anderen Auswirkungen des Festkörpers auf die Linienbreite ausreichend vermindert, um die durch Hitze induzierte Strukturänderung aufzuzeigen. Die niedrigste gemessene Temperatur ist 25 K. Von dieser Temperatur ab bis 45 K ist die Veränderung zu beobachten.

Contents

List of Figures	12
List of Tables	13
Acronyms	15
1 Introduction	17
2 Fundamentals	21
2.1 NMR in General	21
2.1.1 Pulse NMR	21
2.1.2 Spin Precession	22
2.1.3 Rotating Frame	23
2.1.4 Rotating Wave Approximation	23
2.1.5 $\pi/2$ -pulse, π -pulse	24
2.1.6 Polarization	25
2.1.7 Bloch Equations	25
2.2 Types of Interactions	27
2.2.1 Chemical Shift	27
2.2.2 Dipole-Dipole Interaction	29
2.2.3 Knight Shift	30
2.2.4 Korringa Relation	31
2.2.5 Susceptibility Effects	32
2.2.6 Miscellaneous Couplings	34
2.3 Line Coalescence and Motional Narrowing	34
2.4 Hyperpolarization	34
2.4.1 Optical Pumping	35
2.4.2 Spin Transfer	36
2.4.3 Spin Exchange Optical Pumping	37
3 Materials and Methods	39
3.1 NMR Probe	39
3.2 Sample Crystals	39

3.2.1	Susceptibility of the environmental materials	40
3.3	Laboratory Overview	41
3.4	UHV Chamber	43
3.5	The Magnet	43
3.6	NMR Electronics	45
3.6.1	Electronic Network	45
3.6.2	Probe Head	45
3.6.3	Receive Line	46
3.6.4	Noise Treatment	47
3.7	Data Analysis Methods	47
3.8	Production of Hyperpolarized ^{129}Xe	48
3.9	Gas Transfer	50
3.10	Dynamic Exchange of the Sample	51
3.11	NMR Techniques on Cold Metallic Samples	52
3.12	Determination of the Nuclear Polarization	55
4	NMR at Single Crystal Surfaces	59
4.1	^{129}Xe NMR in Xe/CO/Cu(100)	60
4.1.1	Experiment	60
4.1.2	Results	62
4.1.3	Discussion	64
4.2	^{129}Xe NMR in Xe/Cu(100)	65
4.2.1	Experiment	65
4.2.2	Results	65
4.2.3	Discussion	67
4.3	^{129}Xe NMR in Xe/Graphene/Ir(111)	74
4.3.1	Preparation	74
4.3.2	Experiment	75
4.3.3	Results	75
4.3.4	Discussion	77
5	Order Phenomena on and in Xenon Films	79
5.1	Xenon Film Surfaces	80
5.1.1	Experiments	80
5.1.2	Results and Discussion	81
5.2	Xenon Crystal Structure	85
5.2.1	Experiment	85
5.2.2	Results and Discussion	86
6	Conclusion	91
7	Outlook	93

A	Validation	95
A.1	Signal Validation by Field Shift	95
A.1.1	Xe/Cu(100) Monolayer Line	95
A.1.2	Xe/Graphene/Ir(111) Monolayer Line	95
A.2	Signal Validation by Repetition	97
A.2.1	Xe/Cu(100)	97
A.2.2	Xe/graphene	97
B	Accuracy of Measurements	99
B.1	Xe/Cu(100) Second Layer Line	99
B.2	Xe/Graphene/Ir(111) Monolayer Line	100
C	Setup Imperfections	101
C.1	Temperature Measurement	101
C.2	Background Signal	101
D	Supplementary Materials	103
D.1	Synthesis of Graphene	103
D.2	Estimation of Adsorption/Desorption Equilibria	104
D.3	Calculation of the Linewidth in a Rigid Xenon Solid	105
D.4	Temperature Dependent Polarization Measurement	105
D.4.1	Experiment	106
D.4.2	Evaluation	106
D.4.3	Discussion	106
D.5	Comments on the SEOP Setup	106
D.6	Probe Head Double Resonance Extension Box	109

List of Figures

2.1	Common NMR setup	22
2.2	An FID and its spectrum	26
2.3	^{129}Xe Chemical Shift Table	28
2.4	Line coalescence and motional narrowing	35
2.5	Optical pumping of rubidium – term diagram	36
2.6	Principle of spin transfer	36
3.1	Sample holder scheme, iridium crystal, copper crystal	40
3.2	Overview of the xenon NMR laboratory	42
3.3	Sketch of the UHV setup	44
3.4	Scheme of the electronic network	45
3.5	The probe head	46
3.6	Optical pumping setup	49
3.7	Gas admission system	50
3.8	Single layer experiments at low temperatures – a sketch	52
3.9	Xenon monolayer dynamically exchanged under desorption/adsorption equilibrium conditions – a sketch	52
3.10	Effect of 3 ampere heating current on the linewidth	53
3.11	RIDE sequence	54
3.12	RIDE and no RIDE – a comparison	55
3.13	'Common' polarization determination	57
3.14	Justification for the use of the Lorentz function	57
4.1	TDS: Xe/Cu(100), Xe/CO/Cu(100)	62
4.2	ML experiment on CO/Cu(100) @ T=64...72 K; Xe dosage: 40 ML/s	63
4.3	ML experiment on CO/Cu(100) @ 68 K; Xe dosage: 40 ML/s	64
4.4	Xe monolayer signals on Cu(100)	66
4.5	TDS: Xe/Cu(100)	67
4.6	ML experiment on Cu(100) @ T=84...102 K; Xe dosage: 40 ML/s	68
4.7	ML experiment on Cu(100) @ T=65...73 K; Xe dosage: 40 ML/s	69
4.8	ML experiment on Cu(100); Xe dosage: 40 ML/s – Function Fit	71
4.9	Xe/Cu(100)–adsorbate structures	73
4.10	TPD: Xe/Ir(111), Xe/Graphene/Ir(111)	74

4.11	Xe monolayer signal on graphene	75
4.12	ML experiment on graphene @ $T=80\ldots 99$ K; Xe dosage: 40 ML/s	76
5.1	ML experiment on graphene @ 25 K; Xe dosage: 4 ML/s	81
5.2	ML experiment on graphene @ $T \leq 50$ K; Xe dosage: 4 ML/s	83
5.3	ML experiment on graphene @ 32 K; Xe dosage: 40 ML/s	84
5.4	Simulated linewidth dependence on isotope abundance and polarization	85
5.5	Influence of annealing on the linewidth of a $^{129}\text{Xe}/^{132}\text{Xe}$ mixed film	86
5.6	Justification for the Lorentz function fit in diluted samples	87
5.7	Influence of annealing on the linewidth of a $^{129}\text{Xe}/^{132}\text{Xe}$ layered film	88
5.8	Influence of annealing on the linewidth of a $^{129}\text{Xe}/^{132}\text{Xe}$ mixed film	89
7.1	RIDEPT sequence	94
A.1	ML experiment on Cu(100) @ 93 K; Xe dosage: 40 ML/s –field shift	96
A.2	ML experiment on graphene @ 87 K; Xe dosage: 40 ML/s – field shift	96
A.3	ML experiment on Cu(100) @ $T=91\ldots 98$ K; Xe dosage: 40 ML/s –freq. shift	97
A.4	2nd layer examination on Cu(100) @ $T=69$ K; Xe dosage: 40 ML/s –freq. shift	98
A.5	ML experiment on graphene @ $T=78\ldots 84$ K; Xe dosage: 40 ML/s	98
B.1	ML experiment on Cu(100) @ 70 K; Xe dosage: 40 ML/s – Lorentz fit	99
B.2	ML experiment on graphene; Xe dosage: 40 ML/s – Lorentz fit	100
C.1	ML experiment on Cu(100) @ 70 K; Xe dosage: 40 ML/s – background signal	102
D.1	Line shift dependency on temperature and polarization	107
D.2	Double resonance mode extendable circuit box	109
D.3	Probe head in principle	109

List of Tables

3.1	Calculated and measured shifts arising from the sample susceptibility . . .	41
D.1	An estimated realization of the probe head	110

Acronyms

ADC Analog-to-Digital Converter

AES Auger electron spectroscopy

CIC Cascaded Integrator-Comb

CVD Chemical Vapor Deposition

CW Continuous Wave

DFT Density Functional Theory

EPDM Ethylene Propylene Diene Monomer rubber

EPR Electron Paramagnetic Resonance

EXSY Exchange Spectroscopy

fcc face centered cubic

FID Free Induction Decay

FT Fourier Transform

FWHM Full Width Half Maximum

HP Hyperpolarization

LED Light Emmitting Diode

LEED Low Energy Electron Diffraction

ML Monolayer

NEXAFS Near Edge X-ray Adsorption Fine Structure

NF Noise Figure

NMR Nuclear Magnetic Resonance

PID Proportional-Integral-Derivative

ppm parts per million

PTFE Polytetrafluoroethylene

QMS Quadrupole Mass Spectrometer

RF Radio Frequency

RIDE Ring Down Elimination

RIDEPT Ring Down Elimination and Polarization Transfer

SEOP Spin Exchange Optical Pumping

SNR Signal to Noise Ratio

STM Scanning Tunneling Microscopy

TD Thermal Desorption

TDS Thermal Desorption Spectroscopy

TPD Temperature Programmed Desorption

UHV Ultra High Vacuum

vdW van der Waals

XPS X-ray Photoelectron Spectroscopy

Chapter 1

Introduction

In 1946 the first NMR experiments were successfully performed on protons by Purcell [1] and Bloch [2]. They received the noble price in 1952 because this new technique was appreciated by many researchers and used immediately to determine nuclear magnetic moments. In particular, Proctor [3] already studied the nuclear moment of ^{129}Xe in 1951. Since then it took some time till 1961 when Carr et al. [4] realized that ^{129}Xe has a huge chemical shift range connected to the polarizability of its electron shell. It also became obvious that the nuclear relaxation was faster than expected in xenon gas. In 1963 Torrey [5] ruled out paramagnetic impurities as a cause and stated an intrinsic relaxation process simply by temperature induced atomic collisions. Thereby another opportunity emerged to probe the xenon environment. Thus, ^{129}Xe qualified as an attractive NMR probe for chemical analysis. Additionally ^{129}Xe has a relatively large magnetic moment and a rather simple field interaction originated from its $1/2$ spin quantum number. Furthermore xenon is inert and it contains naturally 26% of ^{129}Xe .

From then on, the interest of numerous researchers was focused on ^{129}Xe NMR. Investigations on xenon in compounds were firstly performed in 1963 [6]. Jameson and coworkers started to calculate theoretical predictions on the chemical shifts in various samples since 1964 [7]. Xenon in different aggregate states was also studied [8]. These are only a tiny selection of examples from the experiments of the next decades.

Up to this time NMR still suffered from a poor Signal to Noise Ratio (SNR) which could only be improved by using large sample sizes. Not until 1980, when Fraissard [9] pointed out his idea to perform NMR in zeolithes (porous solids with a huge interior surface) by soaking them in xenon, it became thinkable to use ^{129}Xe as a probe even for solid surfaces. However, well defined surfaces could still not be investigated because they did not provide enough space for a detectable amount of adsorbed nuclei. For instance, on a Cu(100) crystal surface with 1 cm in diameter $4 \cdot 10^{14}$ xenon atoms may adsorb [10]. In contrast 10^{18} – 10^{20} nuclei are needed for detection [11].

At the same time, research was conducted on the optical pumping [12] of alkali metal atoms and the simultaneous transfer of polarization to noble gas nuclei. In 1978 Grover developed this technique to facilitate the transfer from rubidium to ^{129}Xe which caused a dramatic increase in NMR signal strength [13]. Hence, by hyperpolarization the potential

was given to overcome the detector sensitivity threshold for investigation of monolayer sized samples. Decades passed till 2004 when ^{129}Xe was probed on a single crystal metal surface [14], here in this research group.

Despite the successful application of ^{129}Xe NMR as a surface scientific method, it is challenging after all. This is due to the combination of techniques of three different physical subject areas. In particular, the functional interaction of the NMR spectroscopy, the hyperpolarization and the Ultra High Vacuum (UHV) technique, to maintain sample cleanliness, is required to perform a ^{129}Xe NMR surface experiment. Nevertheless, surface NMR is an attractive tool because ^{129}Xe is directly sensitive to the local density of electron states.

The proof of this statement is one major task of this thesis. Therefore the comparison between a Cu(100) surface and a Cu(111) surface is drawn by means of respective ^{129}Xe NMR measurements. Cu(100) is known for its missing surface state [15], i.e. the electron density is low, in contrast to Cu(111) [16]. This should be reflected in the effect on ^{129}Xe . The experiment was already performed on Cu(111) [17], where a huge shift of the resonance line was found. So, the ^{129}Xe line shift on Cu(100) has to be determined here and it is expected to be far less.

Another task of this thesis is the ^{129}Xe NMR on carbon structures. Since Novoselov, Geim and coworkers conducted their 'groundbreaking experiments', for that they won the Noble Price, on a hexagonal carbon structure [18], nowadays called 'graphene', the analysis of graphene gained a center stage in surface science [19]. However, experimental NMR data are neither available of ^{129}Xe adsorbed on graphene nor of ^{13}C situated in the 2D crystal, until now.

Certainly, ^{129}Xe NMR results of comparable carbonaceous samples are to mention. The first in the row is xenon adsorbed on graphite. Hereof NMR studies were made with thermally polarized ^{129}Xe [20, 21], pointing out complicated effects arising from the graphite bulk susceptibility. In contrast, an improved sensitivity by hyperpolarization was achieved by Raftery and coworkers [22] in a similar study. Here, short sticking times of xenon on graphite, however, lead to a rather small effect. Pines et al. [23] demonstrated in a comparable examination of polyacrylic acid that the influence on the ^{129}Xe is increased at lower temperatures. Further investigations in amorphous carbon materials, conducted by Ryoo et al. [24], showed that the effect is not solely introduced by the xenon-carbon contact but also by xenon-xenon interactions at higher density. Further investigations of amorphous carbon structures by Boehm et al. [25] summarize the firstly found result, namely that the bulk influences strongly broaden the lines which is mainly connected to interactions in complicated structures. Resonance line shifts, measured under the mentioned conditions, were in the scope of 10 to 170 parts per million (ppm) with respect to the xenon gas line.

Examples for a reduction of the carbon sample dimensionality and a slight decrease of the xenon-xenon contact are also available. On the one hand, the research of Romanenko et al. [26] on ^{129}Xe diffusing in carbon nanotubes showed a temperature dependent shift of 10 ppm, for the highest temperature, and 130 ppm, for the lowest temperature measured. On the other hand, Saunders and coworkers [27] found a shift of 180 ppm of ^{129}Xe caged in a fullerene.

The NMR investigation of ^{129}Xe in contact with a single layer of graphene synthesized on an Ir(111) surface is done within this theses. For this purpose the choice of this substrate is not arbitrary. In fact Ir(111) was selected because NMR data of ^{129}Xe on Ir(111) are available [28] and because recipes for the graphene growth are well established on this surface. One way to synthesize graphene is Chemical Vapor Deposition (CVD) of ethylene (C_2H_4) on a hot Ir(111) surface [29]. At a temperature of about 1100 K ethylene is cleaved pyrolytically [30]. Graphene islands grow by means of the catalytic effect of the Ir(111) surface which is why this process is limited to the point when the metal surface is fully covered. Under careful dosing and temperatures of 1300 K, CVD can lead to a large area growth of single layer graphene with only one domain that even extends over the substrate step edges [31].

Carbon in graphene could be probed directly by means of its spin carrying isotope ^{13}C . But ^{13}C NMR is afflicted with the very same issue of insufficient signal strength analogous to ^{129}Xe . The key advantage of ^{129}Xe is the implementation of hyperpolarization. Though it sounds like probing ^{129}Xe was the method of choice, ^{13}C is not marginalized. Quite the contrary is the case. An application of both nuclei in combination could bring NMR forward in a considerable way. In particular, if the polarization can be transferred from hyperpolarized ^{129}Xe to ^{13}C situated in the specimen, then carbonaceous monolayer layers could be investigated directly by ^{13}C NMR. This is however a task for the future.

Here, in the present thesis a theoretical introduction is given in chapter 2. The equipment and the techniques required to perform ^{129}Xe NMR experiments on monolayers and thin films are described in chapter 3. Then, in chapter 4 the above mentioned analyses of a xenon monolayer in contact with Cu(100) (written as Xe/Cu(100)), Xe/graphene, and further Xe/CO/Cu(100) by means of NMR are demonstrated. Finally, some Xe NMR studies on thin films are documented in chapter 5, in order to give additional information for interpretation of the found results.

Chapter 2

Fundamentals

The following chapter is basically filled with textbook knowledge, albeit necessary, to introduce the conventional vocabulary used in this thesis.

2.1 NMR in General

In principle NMR is feasible for all nuclei with a non vanishing angular momentum \mathbf{I} that is proportional to a magnetic moment $\boldsymbol{\mu} = \hbar\gamma\mathbf{I}$, where \hbar is the reduced Planck constant and γ is the gyromagnetic ratio. $\boldsymbol{\mu}$ will couple to an applied static field \mathbf{B}_0 , conventionally aligned to the z-axis

$$E = -\boldsymbol{\mu} \cdot \mathbf{B}_0 = \hbar\gamma I_z B_0, \quad (2.1)$$

and the spin degeneracy will be lifted $I_z = -I, -I + 1, \dots, I$. The energies connected to the respective values of I_z are also referred to as the nuclear Zeeman levels. Within the whole thesis $I = 1/2$ is assumed because that is the case for ^{129}Xe . An interaction with the nucleus is only effective if its strength corresponds to the difference $\Delta E = E_{(I_z=1/2)} - E_{(I_z=-1/2)}$ between the Zeeman energies E_{I_z} . For instance, an electromagnetic field is resonant with the splitting when it oscillates with the Larmor frequency (in rad/sec)

$$\omega_0 = \frac{\Delta E}{\hbar} = \gamma B_0 \quad (2.2)$$

2.1.1 Pulse NMR

Beside the NMR magnet, providing the quantizing field \mathbf{B}_0 , another field \mathbf{B}_1 , alternating with the Larmor frequency, is introduced by a coil aligned perpendicularly. The fields and the respective placement of the sample are depicted in figure 2.1.

Applying Continuous Wave (CW)-NMR, \mathbf{B}_1 is oscillating with a constant frequency, in the Radio Frequency (RF) range, whereas \mathbf{B}_0 is swept across a small span about the resonance condition. CW-NMR however suffers from its slowness and its limited range of applications. Therefore, Fourier Transform (FT)-NMR, also known as pulse-NMR, is

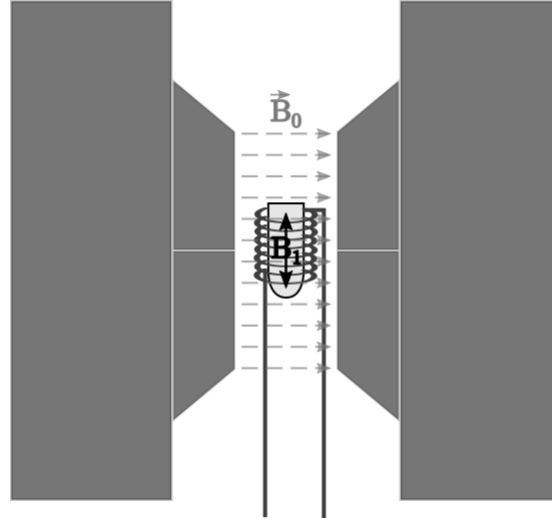


Figure 2.1: Common NMR setup in an electromagnet from a Varian XL 100 spectrometer.

preferred. In pulse NMR \mathbf{B}_0 is kept constant, and the \mathbf{B}_1 frequency is varied by application of a pulse with a wide excitation band in Fourier space. The answer, i.e. the signal, of the nuclei can be received by the same coil in which \mathbf{B}_1 is induced as it is the case here.

2.1.2 Spin Precession

The theoretical description is essentially taken from Levitt [32]. Under an applied constant field, and without any other interaction, a spin can either be in spin-up or spin-down state, or in a superposition of both. The time dependence of a spin state $|\Psi\rangle$ which has to fulfill the Schrödinger equation

$$\frac{d}{dt} |\Psi\rangle = -i\mathcal{H} |\Psi\rangle \quad (2.3)$$

is thus a phase change

$$|\Psi(t)\rangle = e^{-i\mathcal{H}t} |\Psi(0)\rangle. \quad (2.4)$$

A particular choice of

$$\mathcal{H} = \gamma \mathbf{I} \cdot \mathbf{B}_0 = \gamma B_0 I_z = \omega_0 I_z \quad (2.5)$$

makes clear that the change in phase

$$|\Psi(t)\rangle = e^{-i\omega_0 t I_z} |\Psi(0)\rangle \quad (2.6)$$

describes a free precession of the spin, or an ensemble of uncoupled spins, around the z-axis with the Larmor frequency.

An RF field is applied perpendicularly to B_0 . Consequently, it couples to the I_x and I_y components of the spins. This motivates the definition of rotation matrices

$$R_k(\phi) = e^{-i\phi I_k} \quad , \quad k = x, y, z \quad (2.7)$$

with the commutation relations

$$R_x(\phi)I_yR_x(-\phi) = I_y \cos(\phi) + I_z \sin(\phi) \quad (2.8)$$

and the cyclic analogues.

2.1.3 Rotating Frame

In order to understand the influence of a field, which is the superposition of $\mathbf{B}_0 = B_0 \mathbf{e}_z$ and $\mathbf{B}_1(t) = B_1 \cos(\omega t) \mathbf{e}_x$, one usually switches from the static point of view, the lab frame, to a coordinate system that rotates with the frequency ω of the RF. This is referred to as the rotating frame. The rotation can be expressed with help of a rotation matrix. Thus, a state in rotating frame can be written as

$$|\Psi\rangle_{\text{rot}} = R_z(-\omega t) |\Psi\rangle_{\text{lab}}. \quad (2.9)$$

For the states in the rotating frame a transformed Schrödinger equation is defined by

$$\frac{d}{dt} |\Psi\rangle_{\text{rot}} = -i\mathcal{H}_{\text{rot}} |\Psi\rangle_{\text{rot}}, \quad (2.10)$$

whereby the Hamiltonian acquires an additional term

$$\mathcal{H}_{\text{rot}} = R_z(-\omega t) \mathcal{H} R_z(\omega t) - \omega I_z. \quad (2.11)$$

2.1.4 Rotating Wave Approximation

When the RF field couples to the nucleus it is handy to express B_1 in terms of two counter-rotating fields

$$\mathbf{B}_1 = B_1 \cos(\omega t) \mathbf{e}_x = \frac{1}{2} B_1 [\cos(\omega t) \mathbf{e}_x + \sin(\omega t) \mathbf{e}_y] + \frac{1}{2} B_1 [\cos(\omega t) \mathbf{e}_x + \sin(-\omega t) \mathbf{e}_y]. \quad (2.12)$$

Depending on the sign of γ , either the one or the other term is counter-rotating to the sense of the nuclear precession, and it can be omitted since it is far from resonance. This is the so called rotating wave approximation. Defining the nutation frequency $\omega_{\text{nut}} \equiv \pm \frac{1}{2} \gamma B_1$ the Hamiltonian of the RF field becomes

$$\mathcal{H}_{\text{RF}} = \omega_{\text{nut}} [\cos(\omega t) \mathbf{e}_x + \sin(\omega t) \mathbf{e}_y]. \quad (2.13)$$

By application of the commutation rules given in eqn. (2.8) the formula can be rewritten as

$$\mathcal{H}_{\text{RF}} = \omega_{\text{nut}} R_z(\omega t) I_x R_z(-\omega t). \quad (2.14)$$

With this, the full spin Hamiltonian in rotating wave approximation becomes

$$\mathcal{H} = \omega_0 I_z + \omega_{\text{nut}} R_z(\omega t) I_x R_z(-\omega t) \quad (2.15)$$

which has a form that suggests the transformation with equation (2.11) to the rotating frame

$$\begin{aligned} \mathcal{H}_{\text{rot}} &= R_z(-\omega t) [\omega_0 I_z - \omega_{\text{nut}} R_z(\omega t) I_x R_z(-\omega t)] R_z(\omega t) - \omega I_z \\ &= (\omega_0 - \omega) I_z + \omega_{\text{nut}} I_x. \end{aligned} \quad (2.16)$$

If the RF field is exactly on resonance with the nuclei, i.e. $\omega = \omega_0$, the z-term vanishes and

$$\mathcal{H}_{\text{rot}} = \omega_{\text{nut}} I_x \quad (2.17)$$

remains. In the manner of eqn. (2.10) the effect of a resonant RF field can be expressed as a rotation around the x-axis of the rotating frame

$$|\Psi(\tau)\rangle_{\text{rot}} = R_x(\omega_{\text{nut}}\tau) |\Psi(0)\rangle_{\text{rot}} \quad (2.18)$$

In an uncoupled spin system with $I = 1/2$ nuclei it is a valid model to imagine the spin states as vectors that are flipped by the rotation matrix. As an example, if $\omega_{\text{nut}}\tau = \pi/2$ and the spin is originally in +z direction it is then turned to the -y direction after the RF pulse. This is in fact true for the magnetization because the spins follow the effective field. Here, the 'y' is just a name of an induced phase. As long as the spins 'can remember' this first phase, namely a time period of the order T_2 , subsequent pulses can align the momentary spin states to an arbitrary axis in the xy -plane

$$\mathcal{H}_{\text{rot}} = \omega_{\text{nut}} [I_x \cos(\phi) + I_y \sin(\phi)], \quad (2.19)$$

where ϕ is the phase difference of the consecutive pulse regarding the phase of the first pulse. Here, $\phi = 0, \pi/2, \pi, 3\pi/2$ are chosen, and pulses with the according phases are called -y, x, y, -x pulses respectively.

2.1.5 $\pi/2$ -pulse, π -pulse

Pulses with a defined length, so that $\omega_{\text{nut}}\tau = \pi/2$ is fulfilled, are of practical interest because, when applied, the equilibrium magnetization is flipped completely from the z-direction into the transverse plane. After the pulse the development is described by eqn. (2.24), and it can be measured by the transmitter/receiver coil (=transceiver coil) with the maximum possible signal strength. If $\omega_{\text{nut}}\tau = \pi$ is valid, then the pulse is called an inversion pulse.

2.1.6 Polarization

The NMR signal strength is proportional to the absolute value of the net magnetization

$$M_0 = \mu(n_{\uparrow} - n_{\downarrow}) \quad (2.20)$$

that is dependent on the magnetic moment μ of a single nucleus and the number densities of the nuclei in the up-state n_{\uparrow} and in the down-state n_{\downarrow} . Defining $n \equiv n_{\uparrow} + n_{\downarrow}$ and by introducing the polarization

$$P_z = \frac{n_{\uparrow} - n_{\downarrow}}{n_{\uparrow} + n_{\downarrow}} \quad (2.21)$$

the magnetization can be expressed as $M_0 = \mu n P_z$. In thermodynamic equilibrium the population of states obeys Boltzmann's principle

$$\frac{n_{\downarrow}}{n_{\uparrow}} = \exp\left(\frac{-\hbar\gamma B_0}{k_B T}\right). \quad (2.22)$$

With this the polarization can be rewritten as

$$P_z = \tanh\left(\frac{\hbar\gamma B_0}{2k_B T}\right) \approx \frac{\hbar\gamma B_0}{2k_B T} \quad (2.23)$$

where the approximation is valid for temperatures above mK.

Example:

^{129}Xe at $T = 300$ K and $B_0 = 2$ T has a thermal polarization of $P_z = 2 \cdot 10^{-6}$.

2.1.7 Bloch Equations

Pulse NMR is called so since a hard RF pulse is induced in the coil with a frequency close to ω_0 . If the frequency band of the pulse is sufficiently broad, then coherences are induced in the nuclear ensemble. The nuclear reaction to the fields is a quantum mechanical process, whereas the evolution of the magnetization after the pulse

$$\frac{d\mathbf{M}}{dt} = \gamma \mathbf{M} \times \mathbf{B}_0 - \frac{M_x}{T_2} \mathbf{e}_x - \frac{M_y}{T_2} \mathbf{e}_y - \frac{M_z - M_{\text{eq}}}{T_1} \mathbf{e}_z \quad (2.24)$$

is treated thermodynamically and can be measured. Formula (2.24) is the Bloch equation for a spin system that is coupled to a heat bath (particularly the electron environment of the nuclei), whereat M_{eq} is the magnetization in thermodynamic equilibrium. T_1 is called the spin-lattice (or longitudinal) relaxation time which describes the decay to the thermodynamic equilibrium with the 'lattice', i.e. a heat bath of fluctuating interactions with the nuclei. The other characteristic time T_2 is the spin-spin (or transversal) relaxation time which is a measure for the dephasing among the precessing nuclei, causing a vanishing

magnetization in the xy -plane. When the orientation of the magnetization is modified by a preceding RF-pulse, the nuclear spins will loose their coupling as soon as the RF is turned off. The decaying nuclei are, in turn, inducing an electromagnetic field oscillating with the Larmor frequency in the transceiver coil. This field has in general the same shape as a solution to eqn. (2.24) and is called the Free Induction Decay (FID).

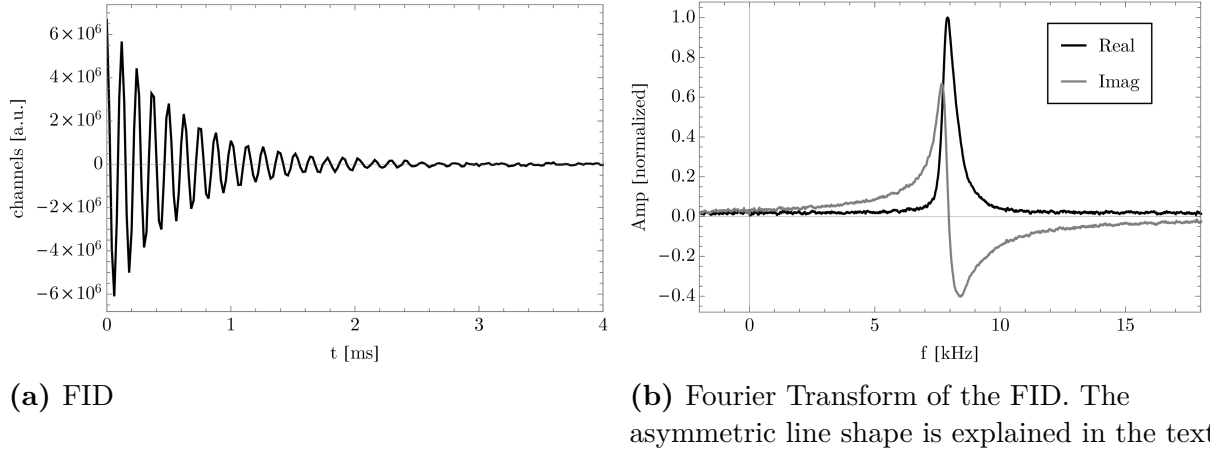


Figure 2.2: An FID and its spectrum. Answer of a small tip angle pulse applied on a highly polarized 99% isotopically pure ^{129}Xe film at 30 K. Signal frequency is down converted by mixing with 23.275 MHz.

In ideal situations the silhouette of an acquired FID, as shown in fig. 2.2a, decays exponentially with $1/T_2$. In real experimental situations, however, T_2 is shortened. $1/T_2$ is replaced by $\lambda \equiv 1/T_2^* = 1/T_2 + 1/T_2'$ where T_2' represents the relaxation due to local distortions which can be caused by setup imperfections on the one hand or further (except B_0 and B_1) nuclear interactions on the other hand.

An FID of uncoupled (or slightly coupled) spins can be described by the function

$$s(t) \sim \cos(\omega_0 t) e^{-t/T_2^*} \quad (2.25)$$

its FT receives Lorentzian line shape for the real part

$$S(\omega) \sim \frac{\lambda}{\lambda^2 + (\omega - \omega_0)^2} + i \frac{\omega_0 - \omega}{\lambda^2 + (\omega - \omega_0)^2}. \quad (2.26)$$

In contrast, when strong interactions are present, which is the case especially in solids and under hyperpolarization, the lineshape can become skewed ^a, as it is shown in fig. 2.2b.

^aThe influence of dipole interactions on lineshapes is conventionally treated by the method of moments. Under equilibrium conditions the 3rd moment vanishes [33] and thus does the skewness. However, for high polarization this assumption does not hold anymore. By means of a polarization dependent evaluation, the effective contribution of the dipole interaction to the skewness could be derived [34, 35].

2.2 Types of Interactions

The main interaction is the coupling of the nuclei to external magnetic fields, namely the high static B_0 or resonantly alternating B_1 fields. In contrast, all other contributions are treated as small perturbations.

A different process is needed to cause spin flips, for example the hyperfine interaction, thus the coupling to electrons which creates the second highest effect. Electrons can take effect on the nuclei in multiple ways. Dominant is the hyperfine interaction, followed by the shielding effect caused by the diamagnetic behavior of the electrons in complete shells surrounding the nuclei. Here, in the observed systems, nuclei in the vicinity of metals experience an additional strong field caused by the metallic paramagnetism. The next smaller contribution to the interaction is the chemical shift, which is the amount of deshielding that is introduced by the perturbation of the electron clouds, for instance by chemical bondings. Despite the fact that xenon is a noble gas, it can react chemically with certain elements like Fluorine which leads to chemical shifts of several thousands of ppm, as shown in fig. 2.3. Therefore, this effect is usually stronger than the contribution of a metal. Nevertheless, this is not the case here since xenon only physisorbs on substrates.

Next in line is the dipole-dipole interaction between the nuclei. It yields especially in solids because the atomic distances are short.

Interactions with the nuclei can cause, on the one hand, a shift of the resonance line because of an additional average field at the location of the nucleus, if the interaction Hamiltonian has nonvanishing diagonal entries. On the other hand, a resonance line broadening due to the off-diagonal contributions, which can –but not necessarily have to– be connected to a relaxation process. In the following some of the representatives for shifts and relaxations are explained in bit more detail.

2.2.1 Chemical Shift

A nucleus is embedded, at least, in the electron environment of its atom. So, a nucleus does not interact with an applied external magnetic field B_0 solely but also with the induced magnetic field B_{ind} of the electron cloud. Therefore, the Larmor frequency

$$\omega'_0 = \gamma_n(B_0 - B_{\text{ind}}) = \gamma_n B_{\text{loc}} \quad (2.27)$$

follows the local field B_{loc} . These deviations can be rewritten as small and commonly linear changes of the external field

$$\mathbf{B}_{\text{loc}} = (1 - \delta) \cdot \mathbf{B}_0. \quad (2.28)$$

δ is a tensor in general but here a scalar treatment is sufficient.

In practice these absolute shifts δ are hard to determine. So, the rather handy method to express the influence of the prevailing electron environment is to refer the shift to a standard sample, i.e. a relative shift. This difference is referred to as the chemical shift σ

since the change in the shielding is mainly due to the chemical environment of the atoms. So the chemical shift is expressed as

$$\sigma = \frac{\omega_0 - \omega_{\text{ref}}}{\omega_{\text{ref}}} \quad (2.29)$$

where σ is typically given in ppm (and can be expressed as a tensor as well).

The effect of the electrons is dominantly diamagnetic, arising from spin fluctuations obeying Lenz's law in the complete shells/bands. For ^{129}Xe in xenon gas, the electrons are shielding the bare nucleus in such a way that the frequency is lowered by 5600 ppm [36].

A paramagnetic contribution to the shift is also possible. Its strength is dependent on the localization of the electrons at the nuclear site. Truly unsaturated electron spins are beyond the meaning of a chemical shift.

All contributions to the shift, even though their origin is not necessarily of chemical nature, are small and therefore additive.

Chemical Shift Ranges of ^{129}Xe

Some examples for the chemical shifts of ^{129}Xe are given in figure 2.3.

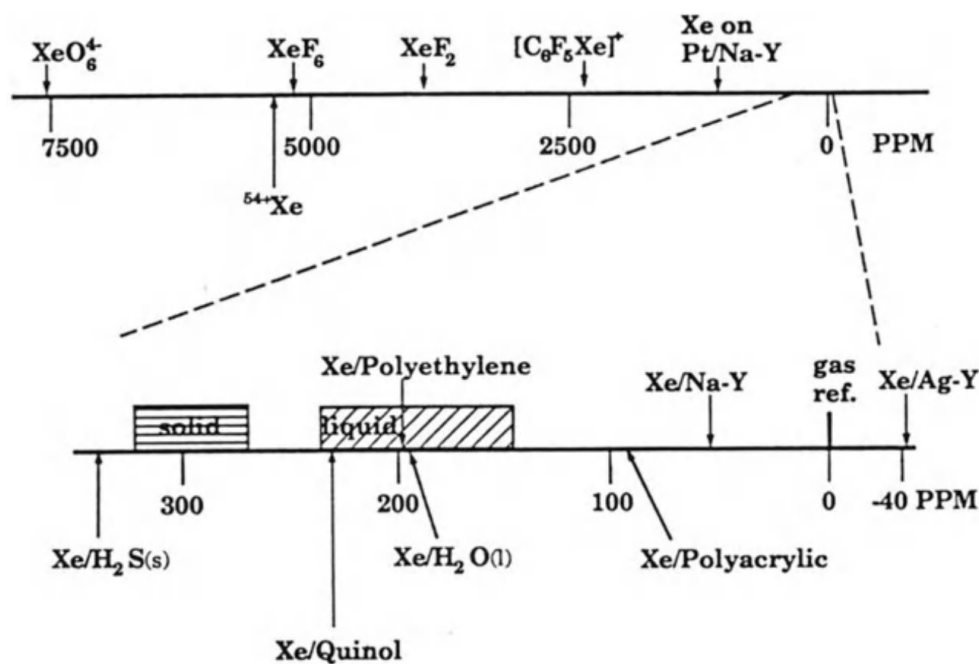


Figure 2.3: ^{129}Xe Chemical Shift Table. Zero ppm are referred to the shift of ^{129}Xe in diluted xenon gas. The picture was taken from [36]

In particular, the case of solid xenon is interesting. Due to the additivity and the Xe-Xe distance dependence [37] of the chemical shift, 25 ppm per Xe atom can be estimated for a ^{129}Xe located in a fcc structure. Thus, ^{129}Xe in a xenon fcc crystal has a shift of $\sim 12 \cdot 25 \text{ ppm} = 300 \text{ ppm}$ in the bulk and $\sim 9 \cdot 25 \text{ ppm} = 225 \text{ ppm}$ at the surface. This was empirically confirmed by [17, 28].

Comments:

- Within this thesis the Larmor frequency ω_{ref} of ^{129}Xe in xenon gas is used as the reference. A change of the electron environment by, for example, adsorbing xenon gas on a solid surface is commonly de-shielding (except for some occasions [36] which are not present here). Thus the chemical shifts σ are positive by definition.
- For nuclei with negative gyromagnetic ratios, as it is the case for ^{129}Xe , the traditional notation of the frequency scale on the abscissa is of the manner: *high freq.* \leftarrow *low freq.*. Against this, the spectra are drawn in the intuitive way from left to right with increasing (positive) frequencies, here. Therefore, the shifts rise from left to right in figures.

2.2.2 Dipole-Dipole Interaction

Formulas within this section are taken from [38] and some units are adapted by means of [32]. The interaction of two spins \mathbf{I} and \mathbf{S} with the respective gyromagnetic ratios γ_I and γ_S is expressed with the dipole Hamiltonian

$$\mathcal{H}_{\text{DD}} = -\frac{\mu_0}{4\pi} \gamma_I \gamma_S \hbar \left(\frac{\mathbf{I} \cdot \mathbf{S}}{r^3} - 3 \frac{(\mathbf{I} \cdot \mathbf{r})(\mathbf{S} \cdot \mathbf{r})}{r^5} \right), \quad (2.30)$$

where \mathbf{r} stands for the distance vector between the two spins and μ_0 is the vacuum permeability. Although eqn. (2.30) does not depend on external field strength, the operators inherit the coordinate system defined by \mathbf{B}_0 . Furthermore it becomes handy, for describing rotations, to transform J_x and J_y to $J_{\pm} = J_x \pm iJ_y$ with $J = I, S$. Writing the projections of the operators explicitly eqn. (2.30) becomes

$$\mathcal{H}_{\text{DD}} = -\frac{\mu_0}{4\pi} \frac{\gamma_I \gamma_S \hbar}{r^3} (A + B + C + D + E + F). \quad (2.31)$$

The terms A to F are:

$$A = I_z S_z (3 \cos^2(\theta) - 1) \quad (2.31a)$$

$$B = -\frac{1}{4} [I_+ S_- + I_- S_+] (3 \cos^2(\theta) - 1) \quad (2.31b)$$

$$C = -\frac{3}{2} [I_z S_+ + I_+ S_z] \sin(\theta) \cos(\theta) e^{-i\phi} \quad (2.31c)$$

$$D = -\frac{3}{2} [I_z S_- + I_- S_z] \sin(\theta) \cos(\theta) e^{+i\phi} \quad (2.31d)$$

$$E = -\frac{3}{4} [I_+ S_+] \sin^2(\theta) e^{-2i\phi} \quad (2.31e)$$

$$F = -\frac{3}{4} [I_- S_-] \sin^2(\theta) e^{+2i\phi} \quad (2.31f)$$

θ and ϕ are polar angles defined by the projection of \mathbf{r} on \mathbf{B}_0 . The terms C to F do not conserve energy in two-particle interactions. Hence, they are often ignored because they are rather improbable. For the case $\gamma_I \neq \gamma_S$ only the A term is energy conserving.

Formula (2.30) is not only valid for interactions among similar and dissimilar nuclei but also for interactions with electrons. Due to the far larger gyromagnetic ratio the dipole-dipole terms including electrons give the largest contribution to the chemical shift. This is especially valid for interactions of nuclei with localized electrons and when the electrons have a non vanishing probability to localize at the nuclear site. In the latter case the hyperfine coupling has to be added, which is discussed in the next sections.

2.2.3 Knight Shift

This section is based on the textbook knowledge taken from [39]. The resonance frequency is shifted by the so called Knight shift if NMR is performed in metals. The shift arises from polarized conduction electrons that interact with the nuclei via hyperfine interaction. When a field B_0 is applied, the electrons are polarized due to the metallic paramagnetism. Assuming the conduction band as a free electron gas the electrons are magnetized by the amount

$$M_z = \mu_B (n_+ - n_-) = \mu_B^2 B_0 D(E_F) = \frac{3n\mu_B^2}{2k_B T_F} B_0 = \frac{\chi_{\text{Pauli}}}{\mu_0} B_0, \quad (2.32)$$

where μ_B is the Bohr magneton, n_{\pm} are the number densities of electrons aligned parallel/antiparallel to B_0 , $n = n_+ + n_-$, $D(E)$ is the density of states, T_F is the Fermi temperature, and $E_F = k_B T_F$ the Fermi energy. While $T \ll T_F$ is valid, expression (2.32) is independent of temperature which is certainly a good approximation for $T \leq 300$ K.

The magnetic induction field due to the electron magnetization interacts with the nucleus in two different ways: On the one hand the s-electrons interact via the Fermi contact interaction. On the other hand the electrons with non vanishing angular momentum interact with the nucleus via dipole-dipole coupling, but this contribution to the field is usually negligible compared to the former one. The field of the s-electrons at the nuclear site is thus

$$\mathbf{B}_e = \frac{2}{3} \mu_0 \gamma_e |\Psi(\mathbf{r} = \mathbf{0})|^2 \mathbf{S}. \quad (2.33)$$

γ_e is the gyromagnetic ratio, $|\Psi(\mathbf{r} = \mathbf{0})|^2$ is the probability density at the nuclear site, and \mathbf{S} is the spin, of the electron respectively. The factor $2/3$ is originated in the demagnetization sphere^b around the nucleus. In high magnetic fields only the z-component is relevant, and for many electrons the ensemble average has to be calculated, thus eqn. (2.33) can be refined to

$$\Delta B \equiv \langle (\mathbf{B}_e)_z \rangle = \frac{2}{3} \mu_0 \gamma_e |\Psi(0)|^2 \langle S_z \rangle. \quad (2.34)$$

^bAn explanation is postponed to section 2.2.5

$\langle S_z \rangle$ is the electron polarization (in units of \hbar) that can be written alternatively as

$$\langle S_z \rangle = \frac{M}{n\gamma_e}. \quad (2.35)$$

Hence, the Knight shift $K \equiv \Delta\omega/\omega_0$ can be rewritten with the equations (2.32), (2.34), and (2.35) as

$$K = \frac{\Delta B}{B_0} = \mu_0\mu_B^2 \frac{|\Psi(0)|^2}{E_F} = \frac{2}{3} \chi_{\text{Pauli}} \frac{|\Psi(0)|^2}{n} \quad (2.36)$$

As an example, in copper: $K = 2370$ ppm or in platinum: $K = -35330$ ppm [40].

2.2.4 Korringa Relation

This section is based on the textbook knowledge taken from [39, 41]. The Korringa relation describes the connection between a relaxation process in metals and the Knight shift. The relation arises from the same original interaction, namely the hyperfine coupling

$$\mathcal{H}_{\text{HF}} = -\gamma_n \mathbf{I} \cdot \mathbf{B}_e \quad (2.37)$$

with γ_n , the gyromagnetic ratio of the nucleus. For a relaxation process binary transitions have to be regarded first, i.e. by substituting $\mathbf{B}_e \rightarrow \mathbf{B}_e/n$ the field of one electron per unit volume is considered. By using equation (2.33) and by additionally introducing generation and annihilation operators $J_{\pm} = J_x \pm iJ_y$ with $J = I, S$ equation (2.37) becomes

$$\mathcal{H}_{\text{HF}} = -\frac{2}{3} \mu_0 \gamma_n \gamma_e \frac{|\Psi(0)|^2}{n} \mathbf{I} \cdot \mathbf{S} = -\frac{2}{3} \mu_0 \gamma_n \gamma_e \frac{|\Psi(0)|^2}{n} \left[I_z S_z + \frac{1}{2} (I_+ S_- + I_- S_+) \right] \quad (2.38)$$

The coupling of the z-components yields the shift as shown in eqn. (2.34), whereas the generator/annihilator terms connect states that express spin exchanges between a nucleus and an electron. Within the ensemble relaxation rate

$$\frac{1}{T_1} = 2 \times D(E_i) f(E_i) \times \frac{2\pi}{\hbar} |\langle f | \mathcal{H}_{\text{HF}} | i \rangle|^2 \times D(E_f) [1 - f(E_f)] \quad (2.39)$$

all electrons $D(E_i) f(E_i)$ of the initial state $|i\rangle$ take part in the exchange process with the transition probability $\frac{2\pi}{\hbar} |\langle f | \mathcal{H}_{\text{HF}} | i \rangle|^2$ and end up in the final state $|f\rangle$ if unoccupied states $D(E_f) [1 - f(E_f)]$ are available. The factor 2 arises because the processes $|\uparrow, \downarrow\rangle \rightarrow |\downarrow, \uparrow\rangle$ and $|\downarrow, \uparrow\rangle \rightarrow |\uparrow, \downarrow\rangle$ contribute equally and, so, only one direction has to be derived. $D(E)$ is the density of states and $f(E)$ the Fermi distribution. In fact the energy differences between E_i and E_f are rather small compared to $k_B T$, and unoccupied states are only available in the range of $k_B T$ around E_F . Thus, the term

$$D(E_i) f(E_i) D(E_f) [1 - f(E_f)] \approx D(E_F)^2 k_B T \quad (2.40)$$

can be approximated. By substituting the terms in eqn. (2.39) with eqn. (2.38) and eqn. (2.40) and by using $D(E)$ from a free electron gas

$$\frac{1}{T_1} = \frac{\pi}{4} \mu_0^2 \gamma_n^2 \gamma_e^2 \hbar^3 |\Psi(0)|^4 \frac{k_B T}{E_F} \quad (2.41)$$

is obtained. That, considering eqn. (2.36), can be rewritten to

$$T_1 T = \frac{\hbar}{4\pi k_B} \left(\frac{\gamma_e}{\gamma_n} \right)^2 \frac{1}{K^2}. \quad (2.42)$$

This is the Korringa relation under the assumption of independent electrons. Besides, if the case is different from ideal, the right-hand side of eqn. (2.42) is extended by the factor B , referred to as Korringa ratio, to take account of all non ideal contributions.

2.2.5 Susceptibility Effects

Another effect on the nuclei, predominantly caused by the electrons, is the macroscopic magnetization \mathbf{M} of the sample materials

$$\mathbf{M} = \chi \mathbf{H} \quad (2.43)$$

in terms of the susceptibility χ and the magnetic field strength \mathbf{H} . In order to express the shift $\sigma_\chi = (B - B_0)/B_0$, the local flux density

$$\mathbf{B} = \mu_0 (\mathbf{H} + \mathbf{M}) \quad (2.44)$$

has to be calculated. \mathbf{B} is solenoidal, i.e.

$$\nabla \cdot \mathbf{B} = 0 = \mu_0 \nabla \cdot (\mathbf{H} + \mathbf{M}). \quad (2.45)$$

In absence of currents the divergences of \mathbf{H} and \mathbf{M} can be assumed to emerge from a 'magnetic charge density'

$$\rho_M = -\nabla \cdot \mathbf{M}. \quad (2.46)$$

Analogously to the electric charges, ρ_M complies with a Poisson equation

$$\nabla^2 \Phi_M = -\rho_M. \quad (2.47)$$

which can be solved by [42]

$$\Phi_M(\mathbf{r}) = \frac{1}{4\pi} \iint_{S(V)} \frac{\mathbf{M}(\mathbf{r}')}{|\mathbf{r} - \mathbf{r}'|} \cdot d\mathbf{f}' \quad (2.48)$$

under the special circumstances that the volume V is uniformly magnetized and bounded by the surface S . Here the direction of the differential surface element $d\mathbf{f}'$ points perpendicularly out of the volume.

If the magnetized material is far away, then the probe nucleus experience an additional B-field that is similar to the one of an ideal dipole. For shorter ranges the shape of the material has to be taken into account as well. However, when the nucleus is embedded in the material itself, for instance ^{129}Xe in a xenon film, an even more detailed discussion of the field contributions must be made.

The inner field and the local field are not identical in general. In order to understand the effect of the susceptibility of the material surrounding the probed nucleus, one usually makes use of the Lorentz cavity model [43]. Lorentz divided the field at the nuclear site into a 'far' and a 'close region'. For the purpose of calculating the far part, a small virtual volume surrounding the nucleus is cut out of the magnetic body. Since the shape of this volume is not crucial it can be chosen spherical, whence called the Lorentz sphere. In contrast, the choice of the radius is restricted. From a macroscopic point of view the radius must be infinitesimally small so that the magnetization of this volume can be assumed to be uniform. By a microscopic consideration the radius must be at least that large that local field variations are averaged out, if one integrates over the volume. So, the resulting field would be equal to the one of a homogeneously magnetized sphere. In practice the field of the magnetized body could be calculated by applying a macroscopic theory, for instance a scalar potential arising from magnetic charges situated on the surface. Therefore, the shape of the magnetic body has to be taken into account. Afterwards, the magnetization of the Lorentz sphere, respectively the Lorentz field, must be subtracted. Since magnetic charges compensate the external field, the contribution of the body is negative (and the Lorentz field is positive). Hence, the field is called 'demagnetization field' [39].

In general, the determination of the 'close field' is far more complicated. However, due to symmetry reasons, this field vanishes under certain circumstances. As an example, this is the case for cubic crystals like frozen xenon.

Taken all together, ^{129}Xe in a xenon film experiences a local field [39]

$$\mathbf{B}_{\text{loc}} = \mathbf{B}_0 + \mathbf{B}_{\text{dem}} + \mathbf{B}_{\text{L}} + \mathbf{B}_{\text{dip}} + \mathbf{B}_{\text{nuc}}, \quad (2.49)$$

where \mathbf{B}_{dem} is the demagnetization field, \mathbf{B}_{L} the field of the Lorentz sphere and \mathbf{B}_{dip} (here: $B_{\text{dip}} = 0$) is the close field due to electron dipoles. \mathbf{B}_{nuc} takes into account the formerly mentioned contributions, i.e. the chemical shift, the hyperfine field and the nuclear dipole dipole interaction. If the xenon crystal had the shape of a sphere the demagnetization field becomes

$$\mathbf{B}_{\text{dem}} = -\frac{1}{3}\mu_0\mathbf{M} = -\mathbf{B}_{\text{L}} \quad (2.50)$$

so that the susceptibility effect would be canceled. However, the macroscopic shape is different in general and, thus, a form factor have to be considered.

Further, a similar equation is valid for the nuclear susceptibility which is not negligible for hyperpolarized samples. The macroscopic effect of the nuclear magnetization can be utilized to determine the nuclear polarization which is explained in section 3.12.

2.2.6 Miscellaneous Couplings

Further interactions that are not present here are the quadrupolar coupling and the J-coupling. The former is a coupling of the nuclei to electric fields which is only possible if $I > 1/2$. The latter is an indirect interaction among the nuclei that is mediated by the electrons. The letter 'J' is used because it is the common way to express the total angular momentum consisting of the nuclear and the electron moments. Mainly in covalently bounded molecules J-coupling has to be considered but, using the noble gas xenon, covalent bondings can be disregarded.

2.3 Line Coalescence and Motional Narrowing

Especially in solids, the prior mentioned interactions can cause an inhomogeneous B-field throughout the sample. This is connected with broad lines and/or a distribution of the Larmor frequencies. If the linewidths are sufficiently narrow, discrete NMR lines are resolved and magnetic inequivalent sites can be distinguished.

Temperature activates the atomic motion and enables the spin carrying nuclei to visit places with different fields within the measuring time. This can have twofold effects on the nuclei. In case of a strong inhomogeneous broadening, the lines are narrowed because the locale fields are averaged. This is the motional narrowing. When magnetic inequivalent sites are present, for example due to different chemical bondings, and temperature allows for exchanging from one site to another, then the initially separated lines collapse. Due to the coalescence, the lines broaden firstly and after the merging, with more increased motion, the narrowing effect takes over secondly.

A formula to describe the effect for ideal lines, i.e. infinitely narrow, is given by Abragam [33, p. 450]. When two magnetically different places (1) and (2) with respective Larmor frequencies $\omega_1 = \omega_0 - \delta$ and $\omega_2 = \omega_0 + \delta$ are present so that the probe nuclei can interchange between (1) and (2) with the rate Ω in both directions equally, then the real part of the spectrum has the shape

$$I(\omega) = A \frac{4\delta^2\Omega}{(\omega - \omega_0)^4 + 2(\omega - \omega_0)^2(2\Omega^2 - \delta^2) + \delta^4} \quad (2.51)$$

where A is a scaling factor. This equation is visualized for various exchange rates Ω in relation to the frequency displacement δ in figure 2.4.

2.4 Hyperpolarization

One could think that the signal strength of a small nuclear sample could be increased by cooling down the sample to temperatures below millikelvin. However, this is an illusion. Even if the labor is raised, one would have to wait till the equilibrium is reached, and especially in solids T_1 can become as long as hours or days (years at mK).

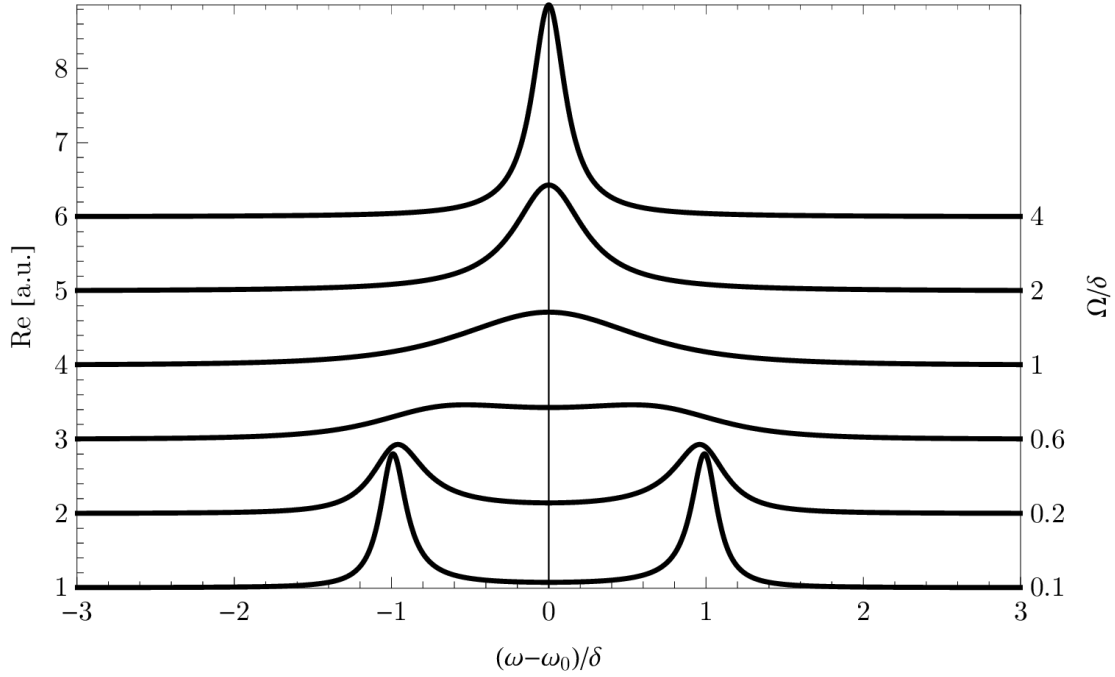


Figure 2.4: Line coalescence and motional narrowing. Eqn. (2.51) is illustrated.

In contrast, a practical solution is to work with polarization far above the thermodynamic equilibrium, which is why it is called Hyperpolarization (HP). For electron systems HP can be achieved by optical pumping, thus the transfer of angular momentum from circularly polarized laser light to electrons. However, as it is mentioned, spin flips induced by electromagnetic fields are an unlikely process in the nuclear regime. Hence, HP electrons are instead used to polarize the nuclei via hyperfine interaction while the electrons are optically pumped.

2.4.1 Optical Pumping

Optical pumping has a great number of applications, but here only the process necessary for HP of ^{129}Xe is described. Extensive explanations are given in an elegant way by W. Happer[12] and cited works.

For the process of optical pumping, firstly, a source of circularly polarized coherent light is needed. Secondly, a system to be pumped is required. Here it consists of the valence electrons of atomic rubidium. And, thirdly, a magnetic field is necessary to define an axis for the spin and the circular polarization. If the photons are tuned to the rubidium D_1 line ($\lambda = 795,4 \text{ nm}$), then the P states are populated. This excitation is selective due to the positive circularly σ^+ -polarized light in contrast to the successive relaxation back to the S state, as depicted in figure 2.5. Effectively, the states of high angular momentum are populated this way.

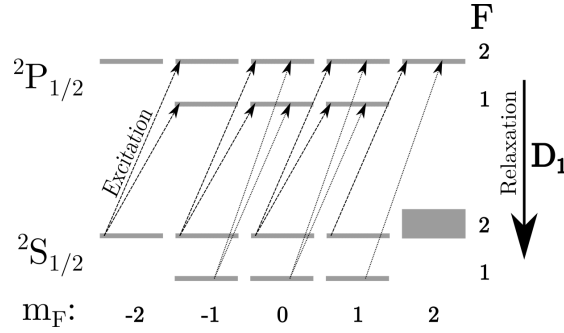


Figure 2.5: Optical pumping of rubidium: The populations (gray rectangles) of the hyperfine levels m_F in ^{87}Rb atoms under irradiation of σ^+ -polarized laser light resonantly to the Rb D_1 -line. Not shown are rates mixing the P-states originated from environmental interactions. The effective rate promotes the states of highest angular momentum. For ^{85}Rb an analog scheme is valid.

2.4.2 Spin Transfer

In a mixture of ^{129}Xe , rubidium and nitrogen the polarization can be transferred from the rubidium electrons to the xenon nuclei via Fermi contact interaction. In this process the gas proportions, pressure and temperature have to be chosen with care because these parameters determine certain process rates. Under the right conditions an Rb-Xe van der Waals (vdW) molecule can be formed by a three body collision of Xe, Rb and N_2 . Only by this type of scattering the total angular momentum is conserved whereas the Rb-Xe molecule starts to rotate. Within the lifetime of the molecule the spin is transferred from the electron to the nucleus and back. Hence, the breakup rate, also induced by a collision with another N_2 , has to match the spin transfer rate for the favored exchange. This is briefly shown in fig. 2.6.

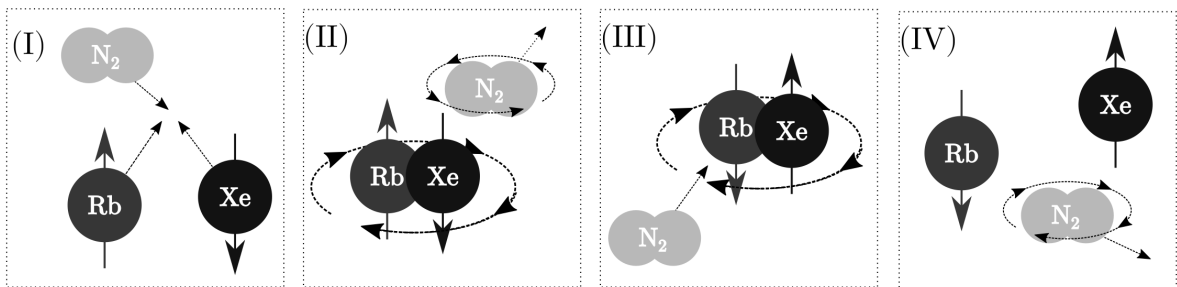


Figure 2.6: Principle of spin transfer: (I) Three body collision; (II) Formation of a vdW molecule; (III) Spin contact time limited by the next collision; (IV) Molecule break up with exchanged spin.

2.4.3 Spin Exchange Optical Pumping

The combination of the mentioned processes is called Spin Exchange Optical Pumping (SEOP). Theoretically any alkali metal can be used for optical pumping and also any noble gas, except argon, for the transfer. A key feature for the particular choice is the exchange cross section. Most crucial for the exchange is the strength of hyperfine interaction which is based on the probability of the presence of the alkaline valence electron on the site of the noble gas nucleus. Its strength depends strongly on the interatomic displacement. For the couple Cs-¹²⁹Xe the distance was found to be ideal. However, up to now no lasers are available to pump the cesium, as effectively as rubidium, which is why rubidium, with the second best cross section, is used.

Beside the facilitation of emerging vdW molecules, the presence of N₂ has further beneficial properties; namely, the quenching of statistically polarized light arising from relaxing Rb that would otherwise depolarize the residual Rb. Further depolarizing processes that are induced by collisions with the pump cell walls or the xenon itself are suppressed if N₂ pressure is kept high, since the relaxing ability of the N₂ is orders of magnitude less than that of the other scatter participants. Additionally N₂ broadens the adsorption line. This makes the polarizing process robust against small wavelength deviations.

Qualitatively the polarizations of Rb and Xe can be given respectively as

$$P_{\text{Rb}} = \frac{\gamma_{\text{OP}}}{\gamma_{\text{OP}} + \Gamma_{\text{Rb}}} \quad (2.52)$$

$$P_{\text{Xe}} = \frac{\gamma_{\text{SE}}}{\gamma_{\text{SE}} + \Gamma_{\text{Xe}}} P_{\text{Rb}}, \quad (2.53)$$

where γ_{OP} is the optical pumping rate, γ_{SE} names the spin exchange rate and $\Gamma_{\text{Rb/Xe}}$ are the respective relaxation rates. All the quantities incorporate many assumptions and dependencies. As an example, γ_{OP} depending on the laser power is much larger than the transfer rate from Xe to Rb which would make P_{Rb} dependent on P_{Xe} for low light intensities.

In Γ_{Rb} the spin transfer from Rb to Xe is included. Both rates Γ_{Rb} and Γ_{Xe} include binary collision processes. In fact under high pressure (and relatively low N₂ concentration) binary collisions can contribute to γ_{SE} . However, the total efficiency also suffers more from the mentioned relaxation process. Additionally, the transfer within the vdW molecule works better because of the far longer, and temperature controllable, contact time. Thus SEOP is applied in the low pressure regime that is about 100 mbar. Further, the xenon is strongly diluted by N₂, where xenon fractions in order of one percent work best. Contact times are defined by the molecular lifetime. The molecule yield depends on the Rb vapor pressure which is dependent on temperature. 100°C proved to be suitable.

Precise discussions of the parameters in the equations (2.52) and (2.53) are not given here since this could fill several doctoral theses. A lot of work which has already been done theoretically and practically by specialists is outlined in [44, 45, 46, 47].

The experimental conditions can be adjusted so that $P_{\text{Rb}} \approx 1$ and the spin transfer rates are high whereas wall relaxation is low. In this laboratory, results of $P_{\text{Xe}} \approx 0.5$ can be obtained on a daily basis. Also $P_{\text{Xe}} \approx 0.75$ have been measured here, see fig. 3.13, and $P_{\text{Xe}} \approx 0.88$ in another work [17].

Chapter 3

Materials and Methods

3.1 NMR Probe

The nucleus in use is ^{129}Xe which is naturally present with 26.4% in Xenon. Here the abundance is, however, enriched to 99%. Besides, 99% enriched ^{132}Xe (Spin zero) is also available. So, it is feasible to make mixtures with adjustable percentages.

^{129}Xe is a 1/2-Spin nucleus. With a gyromagnetic ratio of $-74.521 \cdot 10^6$ rad/sT the ^{129}Xe frequency is 3.59 times less than the ^1H frequency (with opposite sign) at the same field. The signal strengths behave accordingly. Nevertheless, the advantage of ^{129}Xe is its large shift range of several thousands of ppm.

Xenon is brought into contact with the samples by physisorption. Below temperatures of 60 K, Xenon freezes to stable films with face centered cubic (fcc) crystal structure. Even at higher temperatures, depending on the binding energies and the particular substrate, Xenon has a non-vanishing residence time. If the residence time is in the order of the duration of an NMR experiment, the substrate can be probed, assuming appropriate relaxation times.

3.2 Sample Crystals

An iridium single crystal, shown in fig. 3.1b, with an [111]-oriented front side, 10.1 mm diameter, and 2.1 mm height, is used as a substrate for the creation of graphene. On the crystal's back a thermocouple type E, purchased from *OMEGA Engineering inc.* ('chromel'-'constantan' = NiCr – CuNi), is laser welded. It should be noted that the constantan wire becomes slightly ferromagnetic when cooled in liquid nitrogen. This is due to the portion of approximately 1% of manganese which is added to meet the specifications. Therefore and because of the heat transfer, the wire is chosen as thin as possible. Here, the diameter is 0.08 mm. The effect on the NMR applicability is discussed in the section 3.2.1.

The sample crystal to be probed directly is a copper single crystal with an (100)-face. The Cu(100) crystal's height is 3 mm and the diameter is 11 mm. As it can be seen in figure 3.1c a copper wire is welded to the backside. This was done to displace the CuNi-

thermowire that becomes magnetic at low temperature, for a line width reduction test in prior work [35]. Nevertheless, the temperature measurement should not be affected at low temperatures because of the high thermal conductivity of copper and the missing heat radiation.

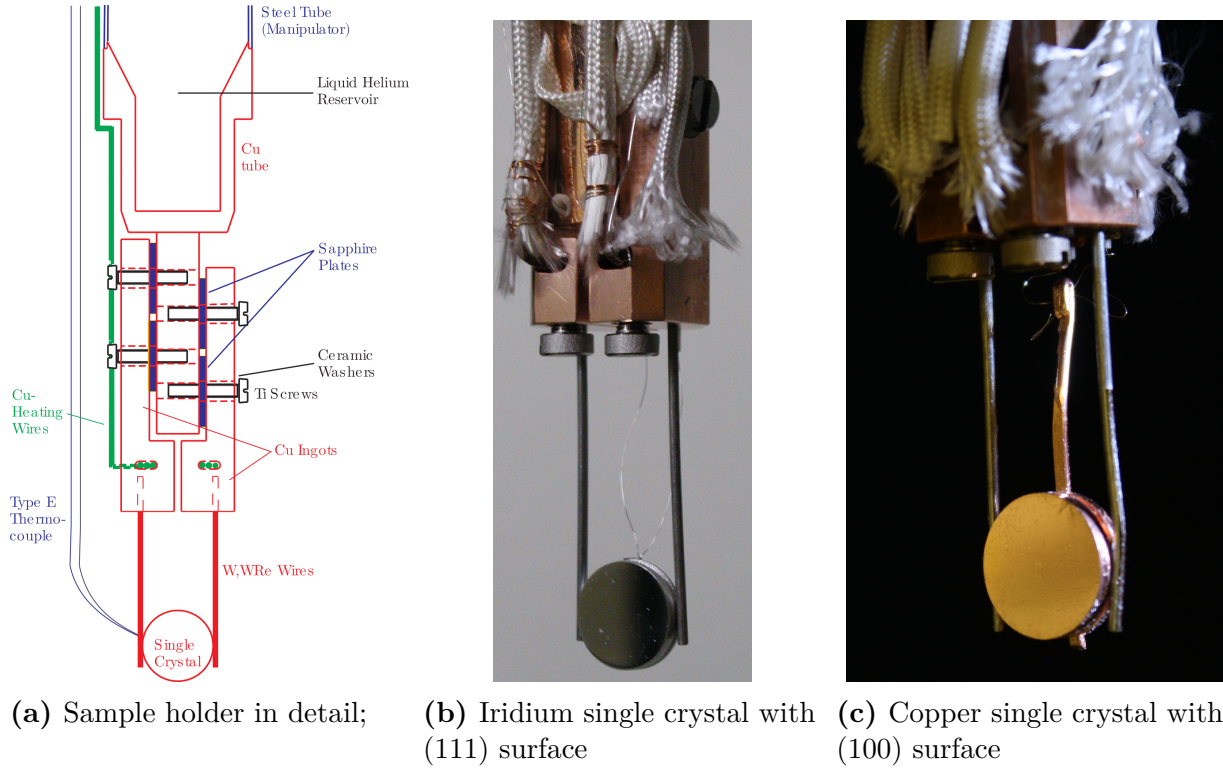


Figure 3.1: Sample holder scheme, iridium crystal, copper crystal

Both sample crystals are held in position by a tungsten wire on one side and by a tungsten-rhenium wire on the other side. The pure tungsten leg has a better heat conduction and is used for cooling, whereas the W/Re alloy has a higher electrical resistivity and is used for heating.

It must be remarked that the given temperatures, within this thesis, are noted as read on the thermometer display. So, the temperatures are consistent per experiment. The comparison with other works can be achieved by regarding appendix C.1.

3.2.1 Susceptibility of the environmental materials

Since the shape of the samples is far from rotational symmetry, any skilled NMR researcher will be skeptical at the sight of fig. 3.1. Hence, the influence of the magnetized materials was studied in previous works [28, 17]. The B-field at the position of a nucleus that is situated in a thin xenon film adsorbed on the respective sample surfaces are calculated. Therefore, equation (2.48) is deployed to calculate the local fields arising from the respective materials. For each material the calculation was performed two times: One time with the

sample surface oriented in the direction of \mathbf{B}_0 and the second time in an angle of 90° to \mathbf{B}_0^a . In table 3.1 the influences of the thermocouple (Type E), the W-WRe clamps, and the xenon film itself are presented.

	Substrate		Type E		W-WRe		Xenon		Total (calc.)		Total (meas.)	
$\theta =$	0°	90°	0°	90°	0°	90°	0°	90°	0°	90°	0°	90°
Copper	-2.1	1.4	2.9	0.2	-0.5	0.7	10	-4.9	12.6	0.0	3.8	0.0
Iridium	9	-4.5					-20	-5	-24	4.5	-30	0

Table 3.1: Calculated and measured shifts of ^{129}Xe in a xenon film arising from susceptibility of the sample, the substrate, etc. θ is the angle between the surface normal and \mathbf{B}_0 . The numeric values are taken from [28, 17] and they are given in ppm. The thermocouple is assumed to be attached directly to the back of the crystal.

The difference of the shifts regarding the two crystal orientations is a measure for the deviation induced by the susceptibility. In particular, the deviation is of the order of 10 ppm within a xenon film. However, this is in the range of the nuclear polarization shift which can be seen in figure 3.13. This means that the susceptibility cannot be distinguished if the momentary polarization is unknown during an experiment on a xenon film.

In experiments on xenon monolayers, only the substrate susceptibility has to be regarded. In comparison to a Knight shift of several hundred ppm the effect is negligible. Additionally, variations in the Xe-Xe distance, for example induced by temperature changes, amount for a the range of shifts (see fig. 2.3 or [37]) probably covering the susceptibility effect.

3.3 Laboratory Overview

The whole setup can be best seen in figure 3.2. By operating the lasers in a separate room, that is climate controlled, the output power stability can be improved. The laser beam is lead through a hole in the wall to the SEOP setup. Hyperpolarized xenon is transferred from the polarization area towards the NMR magnet via a copper tube across the lab. The samples are placed in an UHV chamber to maintain surface cleanliness. The chamber provides a glass extrusion that is put into the magnet's gap. For maintenance purposes the UHV chamber is movable on the supporting scaffolding.

The sample holder within the UHV chamber is additionally connected to a liquid helium cryostat that allows for sample temperatures below 30 K. All NMR electronics, the magnet controlling/regulation system and the electronics for supplying the vacuum are located in the same room. During the experiments the machines that generate spurious signals, i.e. turbo pumps and ion gauges, can be turned off for a sufficiently long period. More details of the particular stages are introduced in the following sections.

^aFor the remaining angles the values can be interpolated by using a $P_2^{(0)}(\cos \theta)$ Legendre polynomial.

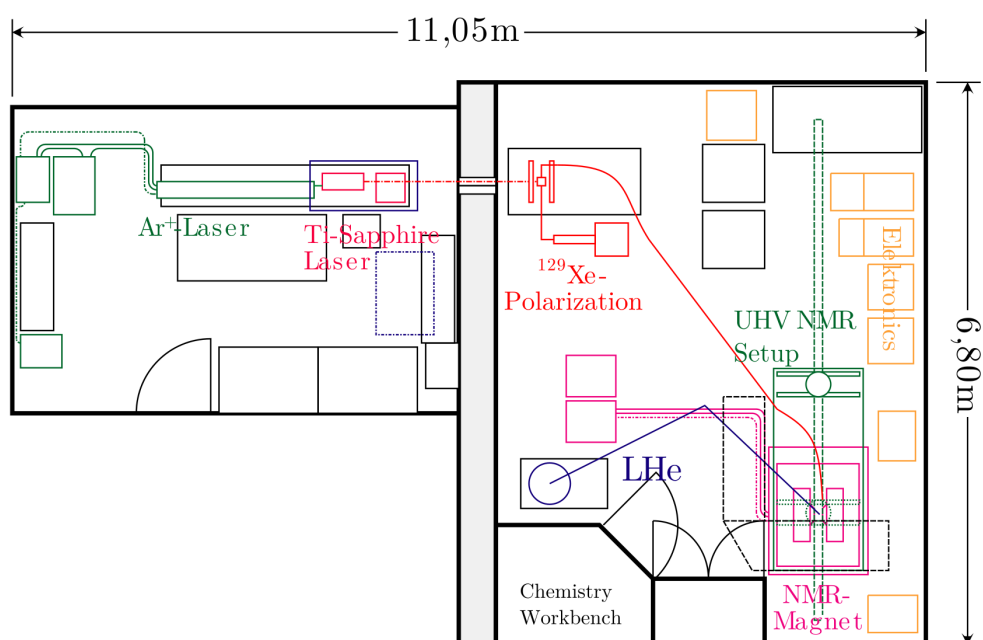


Figure 3.2: Overview of the xenon NMR laboratory

3.4 UHV Chamber

All experiments are performed in UHV to provide clean surface conditions. For sample preparation, an ion gun, working with argon as a sputter gas, is available. The cleanliness and structure of the samples can be checked by Low Energy Electron Diffraction (LEED) and also by Temperature Programmed Desorption (TPD), whereas the desorption yield is measured with a Quadrupole Mass Spectrometer (QMS). The setup scheme is shown in fig. 3.3.

Several gases are connected via leak valves to the chamber. A multi gas admission system, a small volume with several inlets usable for mixing gases, is mounted.

Conventional UHV chambers are made of steel which is not applicable for NMR since the magnetic susceptibility of steel is affecting the field homogeneity. Therefore, a glass extrusion is especially designed satisfying the UHV and NMR demands. Within the same unit the gas admission system for the polarized ^{129}Xe gas is realized, as it is described in section 3.9. The NMR coil is wound outside of the glass cylinder.

The vacuum quality can be highly increased by bake-out. In order to do so, the chamber can be moved out of the spatially constricted area of the magnet and put into a heating box. Heating temperatures are kept moderate at about 100°C to protect the glass-metal junctions. After a few days of baking a base pressure of $2 \cdot 10^{-10}$ mbar can be reached. Further improvements of the pressure, even below 10^{-10} mbar, can be achieved by cooling down the sample holder by the cryogenic flow through line that is usually run with liquid Helium. This cryogenic pumping effect is also used to get rid of depolarized xenon during NMR experiments if the surface temperature allows for desorption.

3.5 The Magnet

An electromagnet *Varian-V7405* provides a homogeneous B-field of 2 Tesla for NMR usage. The poles of the magnet are separated by a 5 cm broad air gap. The advantage of this magnet is that it can be shut down to apply conventional surface analysis and preparation methods that are dependent on well defined trajectories of charged particles.

During operation the field is regulated by means of an hydrogen NMR signal. This is provided by an *NMR Magnetometer Type 9298* [48]. The magnetometer measures the magnetic field in the vicinity of the NMR probe head by a continuous wave NMR on an ^1H probe. The error voltage is proportional to the difference of the ^1H resonance frequency and an external reference frequency. This reference frequency can be set arbitrarily with a *Rhode & Schwarz* frequency generator. In turn, the *Rhode & Schwarz* derives its frequencies from an external 10 MHz synchronization signal provided by the NMR spectrometer (for ^{129}Xe).

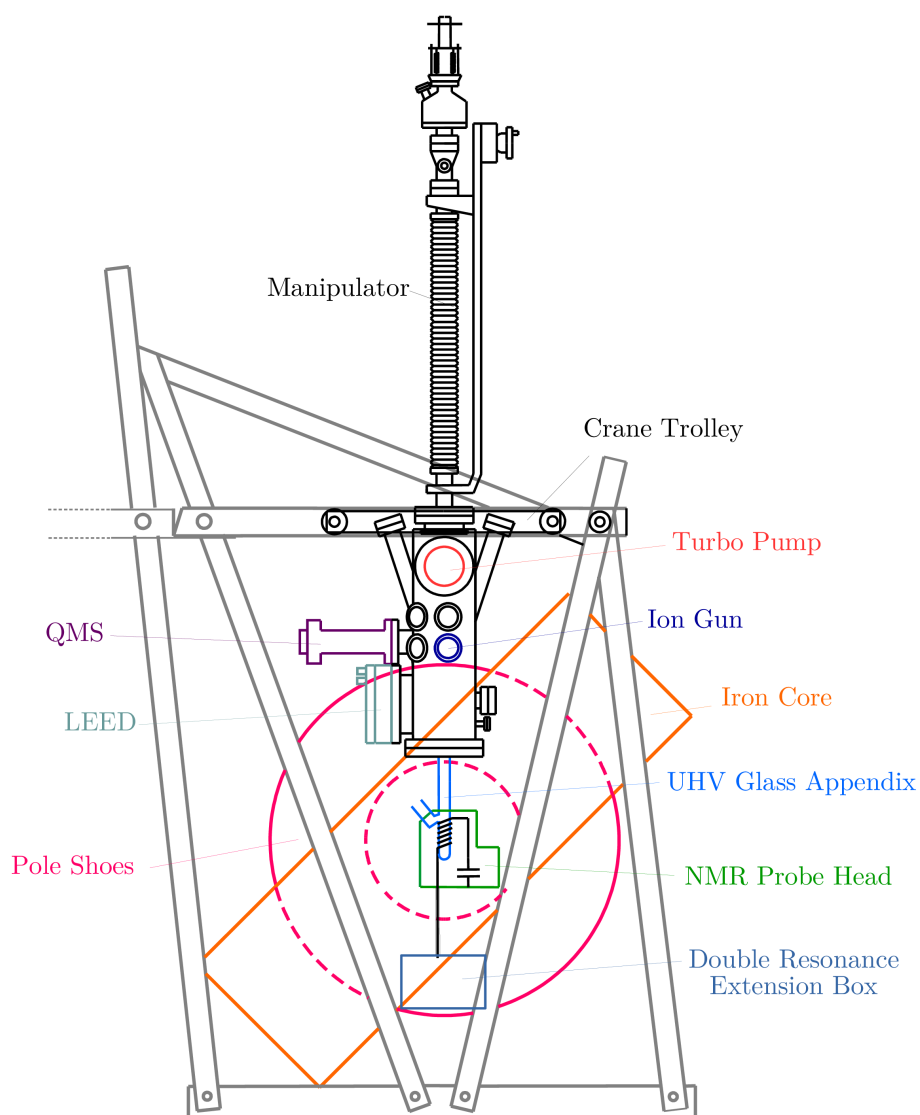


Figure 3.3: Sketch of the UHV setup used in connection with the NMR. The whole assembly is put on a trolley which allows for moving the chamber out of the magnet for maintenance purposes.

3.6 NMR Electronics

3.6.1 Electronic Network

The heart of the electronic setup is a digital spectrometer that consists of a transceiver card *SpinCore RadioProcessor*, a transmitter card *SpinCore PulseBlaster* and a 100 MHz quartz master clock, the frequency standard for all time critical devices. Well shaped pulses can be sent from the RF outputs with an amplitude of 5 to 500 mV. An *LPPA-13010* by *Dressler* amplifies RF waves linearly over a wide band with powers up to 1000 W. Due to the lower limit of the RF outputs and the upper limit of the *LPPA*'s power, the range of suitable high-power amplitudes is increased by attenuators between the *Radio-Processor/PulseBlaster* and the *LPPA*. Further a self-made bandpass, consisting of coils and capacitors, is assembled before the attenuators since spurious signals at 10 MHz and higher harmonics were found on the sending line. The scheme of the electronics is shown in figure 3.4.

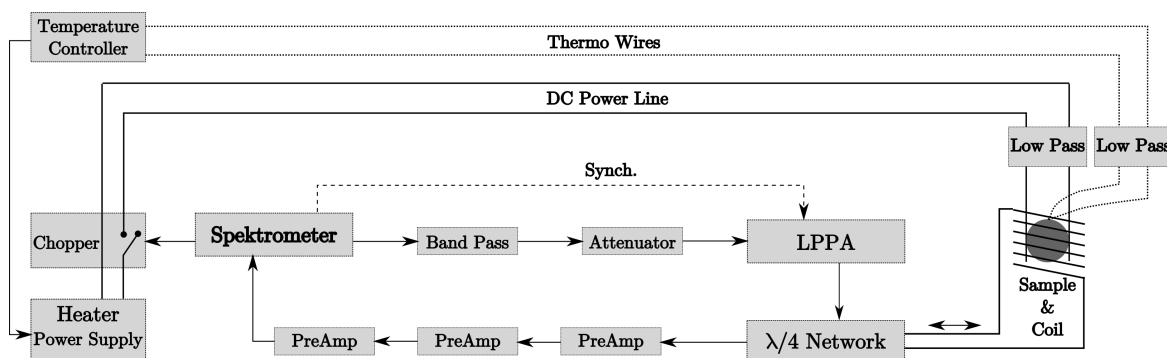


Figure 3.4: Scheme of the electronic network

The transmission and receive channel are split by an electronic switch, i.e. a duplexer. Particularly, the channels can be separated by either a discrete $\lambda/4$ -network or a $\lambda/4$ -cable, both built by the in-house electronic workshop. Which one is used depends on the kind of experiment performed: For the $\lambda/4$ -cable has a better transmission in all directions it suits to measure systems with small signal yield as it is the case with monolayers. However, this also implies that excitation pulses can reach the receive channel which is acceptable for short pulses. But with long pulses, for example spin-lock or decoupling pulses, the low power electronics are overloaded. Therefore, the application of the $\lambda/4$ -network is recommended here.

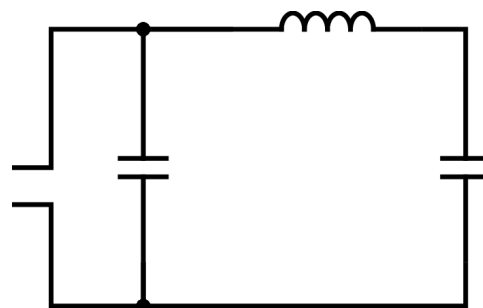
3.6.2 Probe Head

Shown in figure 3.5a, the NMR coil is attached on the outside of the glass tube where the glass outer diameter is 3 cm. The windings are made of silver covered copper wire with 1 mm in diameter. An anti-Helmholtz coil can be mounted, as well on the outside of

the evacuated glass cylinder, for application of gradient pulses aligned to the z-axis. The capacities are realized by variable Polytetrafluoroethylene (PTFE) capacitors received from *Polyflon Company* and static mica capacitors from *Siemens*.



(a) Realization of the wiring. The black snail is a gradient coil



(b) Equivalent circuit diagram of the probe head

Figure 3.5: The probe head

Additionally the probe head can be extended for double resonance purposes. The description of the double resonance work mode is relocated to the appendix D.6.

3.6.3 Receive Line

In the receive line, 2 or 3 preamplifiers obtained from *Advanced Receiver Research* are used. The first one in the line is slightly better than the following ones. It has a gain of 28 dB and a Noise Figure (NF) of 0.5 dB whereas the others amplify with 25 dB and have an NF of 1.0 dB. Overall the gain is far too large for experiments on hyperpolarized films. For this purpose 2 amplifiers are sufficient. Only in experiments whereby one atomic layers are sought that measure less than 1 cm² in area, 3 amps are necessary, albeit they only work reliably, if the setup is cleansed of disturbing signals and noise sources. Between the duplexer and the amplifiers as well as between the amplifiers and the *RadioProcessor* input, the line is connected to ground via pairs of crossed diodes that protect the sensitive electronics against overvoltage.

3.6.4 Noise Treatment

Since the probe head provides ports for the glass parts, it becomes leaky for RF. In addition the samples, the sample brackets and the manipulator are all metallic and therefore receptive for electromagnetic radiation like a big antenna. Transients are mainly received from the electronics inside the UHV chamber. So far, the noise sources, i.e. ion gauges and turbo pumps, are sufficiently treated to perform NMR. However, deviations from the 'standard procedure' occasionally demand for a reconsideration of the setup properties. Thus, the noise treatment task becomes inherently associated with the surface scientific and NMR techniques when they are combined. To perform the planned experiments the following examples had to be regarded.

To achieve a stable temperature away from the very lowest attainable one, the sample has to be heated against the sample cooling. The NMR network is galvanically isolated, as far as possible, from the heating wires. However, secondary influences have to be treated. Namely, the wiring of the thermocouple and the power cables of the heater receive noise in the range of the NMR frequency in use. Therefore, these wires are twisted, shielded, and filtered which reduces the noise background to a level below the inherent noise of a 50 Ω -termination directly connected to the first preamplifier, at least for the used receive band. In reverse, the Proportional-Integral-Derivative (PID) controller, *Temperature & Process Controller* acquired by *Newport Electronics*, benefits from being electronically separated from the RF-pulses.

The most difficult issue is that the heating current generates an additional inhomogeneous magnetic field. It is so intense that the spectral lines are broadened to an unacceptable scale, not to mention that multi pulse or long pulse experiments would dephase the probe nuclei. Hence, the current is shut off by a hard switch, i.e. the 'chopper', shortly before any NMR experiment and turned on again afterwards. Despite the interrupted heating conditions, the regulation of temperature is still possible if the integration interval of the PID controller is set far longer than the chop-and-measure-period.

3.7 Data Analysis Methods

The analog induction signal received is digitized and captured with 75 MHz and 14 bits in the RadioProcessor's Analog-to-Digital Converter (ADC) memory. Then the raw digital signal is multiplied with the sine and cosine of the transmitted frequency and respectively stored in the 'real' and 'imaginary' channels, for the purpose of the quadrature detection. Both channels are filtered separately and down sampled with a Cascaded Integrator-Comb (CIC)^b. The user can set certain parameters like the filter kernel, the aimed output data points, the spectral width and a center frequency on which the filter is dependent. In particular: All acquired FID's are down converted by the chosen center frequency of 23,275,000 Hz so that the spectra shown in this thesis are shifted downward by the same amount, unless otherwise stated.

^bThe filter/down sample process is not explicitly explained by the manual

Signal averaging is a common method to increase the SNR; if N spectra are acquired from identical experiments then the SNR is improved by \sqrt{N} . Averaging can be performed either directly on the RadioProcessor card after the down sampling process or after the data transfer on the PC. Performing the calculation on the card has the advantage of speed because the data transfer consumes several tens of milliseconds. Additionally the storing process and restart of the measurement program on the non-realtime system take an undefined amount of time in the order of 100 ms. However, when the experimental conditions change over the measurement time frame^c, it is recommended to save the data first and evaluate it later.

The data are stored on the PC in form of complex points in the time regime. Apart from the manipulations already performed on the RadioProcessor card the data are further processed, before Fourier transformation, by the following methods:

- Occasionally the first few data points have to be dropped because the signal is clipped due to artifacts, such as ringing or background signals, that are excessively amplified.
- An exponential window function is multiplied with the data array, also known as apodization ('remove the feet'), to give more weight to the FID containing part at the beginning of the array, whereas the noisy tail is suppressed. This technique can artificially broaden the spectral lines for the sake of a higher SNR.
- The mean values for the real and imaginary arrays are derived respectively, and subtracted from the respective arrays. This way a probable 'center glitch', an artifact at frequency=0 Hz, can be eliminated from the spectrum.
- If the spectral peaks are supposed to be fitted to a function it can be helpful to extend the data array and fill it with zeros, the so called zero padding.

3.8 Production of Hyperpolarized ^{129}Xe

The optical pumping setup shown in fig. 3.6 consists of a glass tubing / stop cock system that is also applicable to preparation of gas mixtures before and after the optical pumping process. The laser light, irradiating the pumping cell, is provided by a *Spectra-Physics Argon-Ion Laser BeamLok 2080* that pumps a *Spectra-Physics Ti:Sapphire Laser 3900S*. At the output of the Ti:Sapphire laser a power of 2 W is measured.

For 'usual' ^{129}Xe NMR experiments 4 mbar of xenon with 99% ^{129}Xe isotopic purity is led into the vacuum volume above the pump cell. It is mixed with nitrogen so that the pressure rises to 131 mbar in the same volume. The mixture is then expanded into the hot pump cell whereby the pressure is reduced to 100 mbar. As soon as the cell is in thermodynamic equilibrium the rubidium is polarized and hence the ^{129}Xe .

Further practical details about the setup can be found in the appendix D.5.

^cFor example, the NMR experiment is performed repetitively while xenon is dosed under 'constant' flow. In fact, the xenon flow arises and falls off at the beginning and at the end respectively. The respective data from a moment at the start, the end and the intermediate part should not be averaged.

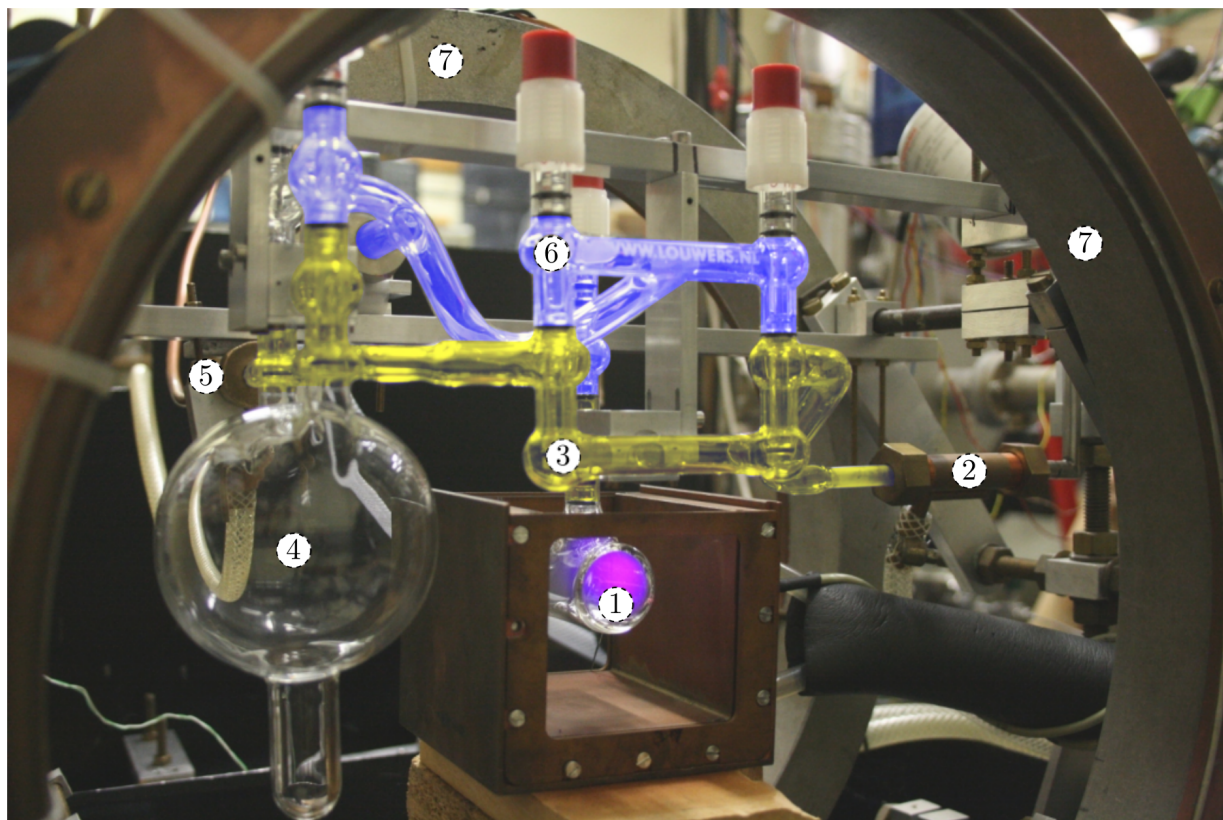


Figure 3.6: The optical pumping setup consists of (1) the pumping cell – original color for demonstration, (2) the gas admission, (3) the main vacuum/ pathway for sample gas – marked yellow, (4) the gas mixing volume, (5) the outlet directed to the NMR setup, (6) the prevacuum volume – marked blue, and (7) the pair of Helmholtz coils. The glass coloring in section 3 and 6 are photoshopped and for clarity only.

3.9 Gas Transfer

In this section the pathway of hyperpolarized ^{129}Xe from the pumping cell to the sample crystal in the NMR coil is described:

The optical pumping setup of fig. 3.6 is connected to the gas admission system depicted in fig. 3.7 via a 7 meter long copper tube across the lab.

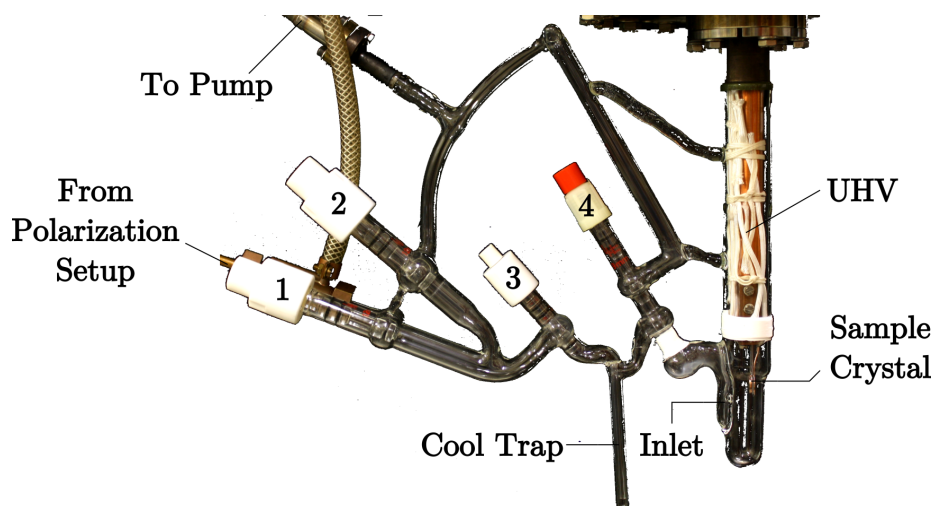


Figure 3.7: Gas admission system with UHV chamber extrusion without NMR probe head; for the gas transfer, the cool trap is put into liquid N_2 . The valves (1) and (3) are open, whereas (2) is closed and (4) is connected to the pump. When the gas has passed the trap valve (3) is closed and (4) is connected to UHV.

On the way from the Helmholtz coils to the NMR magnet, the polarized ^{129}Xe has to pass a section of low field. Even so, the polarization can be conserved consistently over several similarly prepared ^{129}Xe doses, if the gas is transferred fast. Hence, the xenon is pushed (and also protected against wall collisions) in a carrier gas, i.e. an additional amount of N_2 , that preserves the flow in a viscous regime.

Once the xenon is polarized a shot of N_2 , for the boost, is filled into the volume above the pumping cell with a pressure that is higher than in the cell itself. So, when the valve is opened the cold N_2 is spreading into the cell.

Then the valve connected to the copper tube is opened and the gas mixture flows towards the glass manifold, i.e. the low pressure region, whereby it has to pass the cool trap. When the trap is immersed into liquid nitrogen, xenon condenses to the walls whereas the nitrogen (for the boost) is sufficiently volatile to reach the pump. This way the gases are separated. Shortly after, the cool trap valves are closed at first and then the connection to the UHV chamber is established.

Up to this point the xenon is still kept in the cool trap. Due to the xenon vapor pressure at 77 K ($\sim 10^{-3}$ mbar) the hyperpolarized gas flows into the UHV chamber and towards the surface under investigation at a rate of 4 Monolayer (ML) per second, which is also referred to as the '*slow dosage*'. Alternatively one can blow out the liquid nitrogen in the

dewar and replace it quickly by liquid argon. In this way the vapor pressure of the xenon increases by a factor of 10 and, hence, the impinge rate rises to 40 ML/sec which is called the '*fast dosage*'. These rates are estimated by P. Gerhard[28] and they are confirmed by M. Koch [17].

An additional option for dosing is to remove the cryogen from the dewar. This leads to an almost '*instant dosage*' of the xenon. Hereby the loss of polarization in the fringe field of the magnet can be reduced on the one hand. On the other hand also the water that is frozen in the cool trap will thaw a few seconds later and it can contaminate the sample if the valve is not closed sufficiently fast, what is difficult to manage. Further, if high amounts of gas are used, e.g. ^{129}Xe strongly diluted in a carrier gas, then the cooling rate of the crystal is not sufficient to freeze down all the incoming gas at once. Thus a part of the sample gas will accumulate on the sample holder or end up in the vacuum pump.

3.10 Dynamic Exchange of the Sample

Relaxation times are long in solid xenon even in our case where T_1 is reduced since the contact layer to the substrate suffers from strong relaxation due to Korringa relaxation. By spin diffusion the whole xenon film is depolarized after all [35]. Nevertheless, the relaxation times are still long compared to typical experimental times (\sim minutes).

NMR in solids is usually tricky because T_1 defines the repetition time of experiments. This is however not the problem with hyperpolarized samples, but rather the fact that the polarization is lost after a 90° -pulse. 'Repolarization in place' is not possible. So the only option is to replace the entire xenon sample. The most obvious way to replace the xenon is to heat up the substrate above the desorption temperature, cool it down again, repeat the polarization cycle, and adsorb a fresh xenon film onto the substrate. For some experiments this is practical, for example for measuring the relaxation in a film.

In contrast, for achieving a suitable SNR the spectra of hundreds of monolayer experiments must be acquired (and averaged). Thus it is suitable to deposit the xenon with the 'slow' or 'fast' dosing procedure and measure while it is adsorbed. This way a whole film is not required and several hundred experiments can be performed using one boost of xenon. The situation for low temperatures differs from the one close to the desorption temperature because, when the xenon is dosed on a cold substrate, a film is grown layer by layer. So the new, i.e. polarized, xenon layer is measured on top of the old, depolarized, xenon film, as illustrated in fig. 3.8. Hereby the movement of the xenon atoms is strongly reduced.

At high temperatures, when the xenon desorption is not negligible, the measured xenon layer is exchanged by incoming polarized xenon, on the one hand, and the atomic movement is high on the other hand. The regime of desorbing multilayers is not shown here since the dynamics are too complex for illustration.

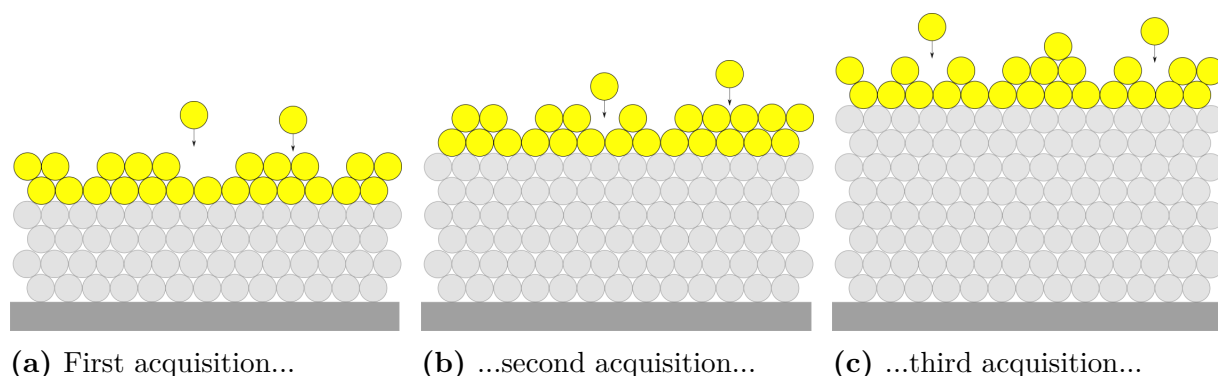


Figure 3.8: Single layer experiments at low temperatures: Only the topmost layers give a signal whereas the remaining film is depolarized in consequence of the preceding NMR measurements.

In figure 3.9 the situation of measurement in a monolayer is depicted^d. In order to perform NMR measurements, it is crucial neither to empty nor to fill the substrate surface completely. The optimized exchange of the xenon is only expected in the regime of partial coverage which is sensitively dependent on temperature and dose rate.

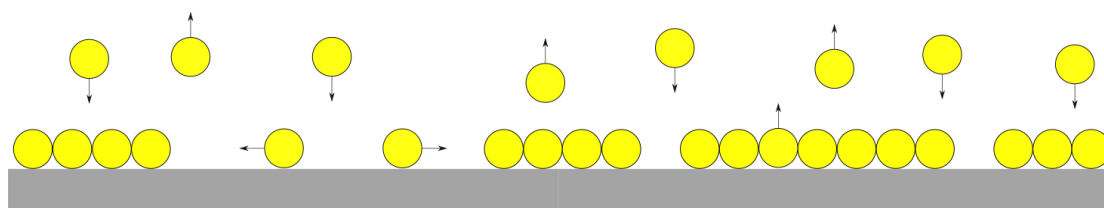


Figure 3.9: Xenon monolayer dynamically exchanged under desorption/adsorption equilibrium conditions; measured directly on a substrate;

In any case the chance is low to mix up a signal from the second or higher layers because the respective desorption processes strongly differ in temperature. For instance, a TPD reveals that the first and second layer desorptions are separated by $\Delta T \approx 30$ K on the Ir(111) surface and about 20 K separated on Cu(100) .

3.11 NMR Techniques on Cold Metallic Samples

Working on metallic substrates brings special characteristics with it. Even though the heating current is not active during the measurement the field inhomogeneity remains due to eddy currents. Especially at low temperatures the resistivity of single crystals is so low that the eddy currents persist for tens of milliseconds which is shown in figure 3.10. This has to be considered for the temperature regulation during NMR experiments. Therefore, a sufficiently long delay is included before the measurement starts.

^dHow to find an equilibrium condition is explained in the appendix D.2

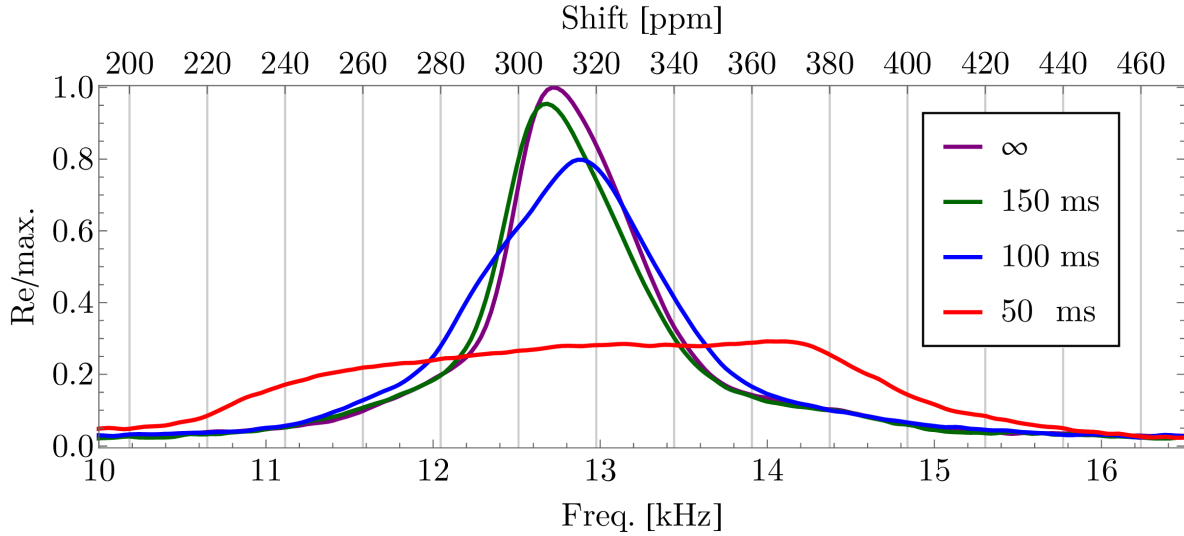


Figure 3.10: Effect of 3 ampere heating current on the linewidth of a ^{129}Xe film grown on a Cu single crystal at approximately 30 K. The waiting times, defined by the moments when the current is chopped off and when the readout pulse is set, are given in the legend. For comparison: The eddy currents in Ir survive about 1/10 of the time in Cu [17]. A measurement with enabled heating current was not performed.

Another artifact, arising in the vicinity of metallic setup components, is the so called acoustic ringing [49, 50]. In contrast to the heating current effects, acoustic ringing cannot be switched off because it is the spurious answer of electron/acoustic shear waves inherently induced by the NMR pulses. The ringing effects are in phase with the RF. Hence, an FID alike wave is acquired that competes with the real NMR signal. The ringing artifacts are known since a long time, which is why solutions are available [51, 52], namely the so called Ring Down Elimination (RIDE) [53] sequence. Their principle is described in the following.

One trick is to make use of the far different relaxation times of the nuclear and electron excitations. The very first way is thus to include a long delay ($\sim 300 \mu\text{s}$) before the acquisition. However, this is not sufficient when signals from monolayers with probably short T_2 ($\sim 1 \text{ ms}$) times are sought. In fact, if the SNR is improved by averaging spectra, then the ringing is also brought back. Hence, the more promising way is to subtract the pulse answer of a spin ensemble originally oriented in the $(-z)$ -direction from one oriented in (z) -direction. If the readout pulses are the same then the ringing will be canceled. In other words, the second trick is to perform the experiment twice with the inclusion of two different preparation processes. As an example, in one of the two experiments, an inversion pulse is applied which inverts the orientation of the magnetization. The thus called 180° -pulse does not generate an FID or, alternatively spoken, the magnetization is kept in the $(-z)$ -direction as long as the electron excitation decayed, when T_1 of the nucleus allows for.

In practice, dominantly the frequency offset and further, unknown but possible dipole interactions, chem. shift anisotropies, or the like have to be regarded in the preparation pulse sequence. Additionally, instrument-based imperfections of the pulses are likely to be

present. So, to avoid these influences, more pulse compositions are applied in the manner of [54]. In figure 3.11 the NMR sequence (or similar) applied in the following experiments is given. Figure 3.12 shows the necessity and the efficiency of a RIDE sequence.

Alternatively one could keep the sequence simple and perform the experiment twice whereat the differing spin orientations are generated by switching the polarizer in the precedent hyperpolarization process. However, the switching time takes several minutes. Thereby plenty experimental parameters can change. As an example, the spin transfer is different, the impinging rate of the xenon on the sample, the ringing characteristics because of a temperature change of the setup, etc.

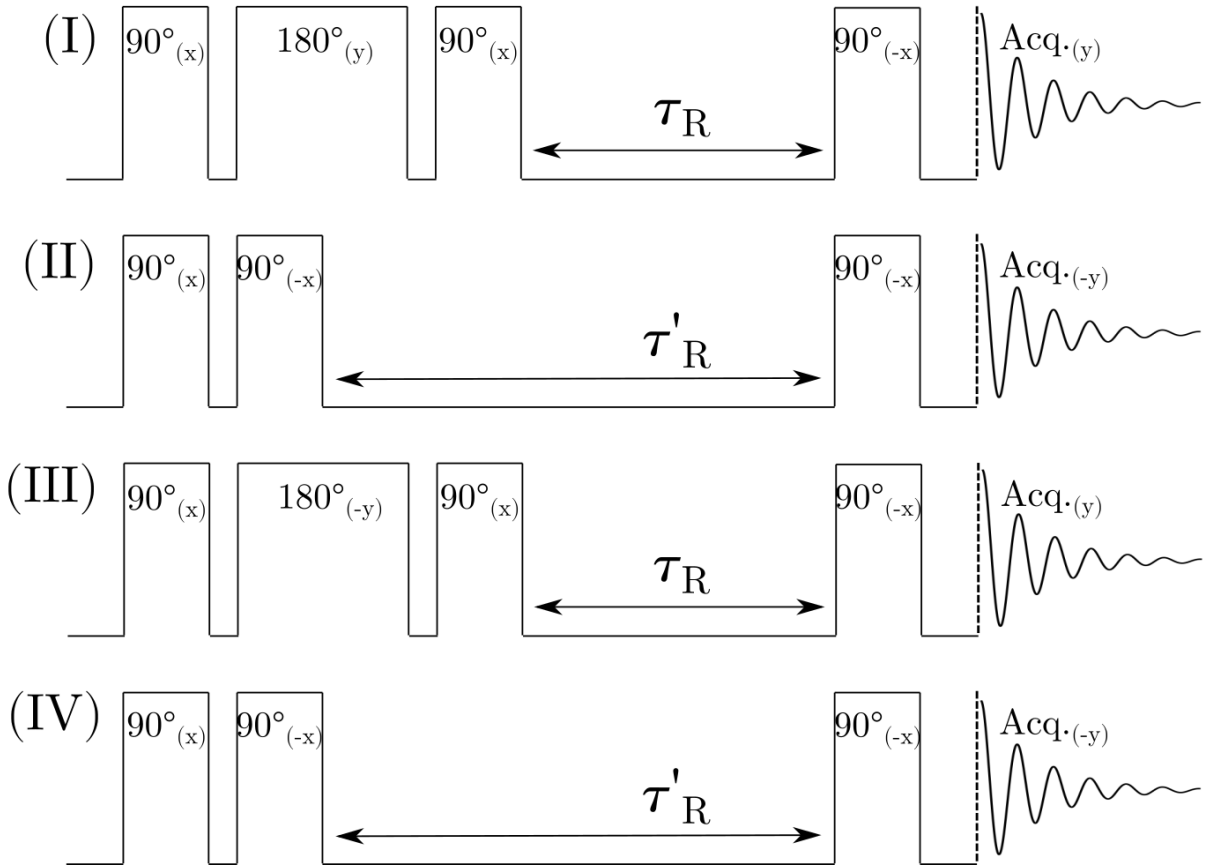


Figure 3.11: RIDE sequence applied in NMR monolayer experiments. The 4 parts are summed up directly on the detector acquisition card. The pulse phases and the dedicated ringing answers add up to zero with part I–IV, but in many cases part I–II are also sufficient to reduce the deadtime. τ_R is chosen to be $400 \mu\text{s}$ at $T \sim 30 \text{ K}$ (solids) and $300 \mu\text{s}$ at $T \sim 90 \text{ K}$ (monolayers). τ_R and τ'_R differ only in the period of the 180° pulse.

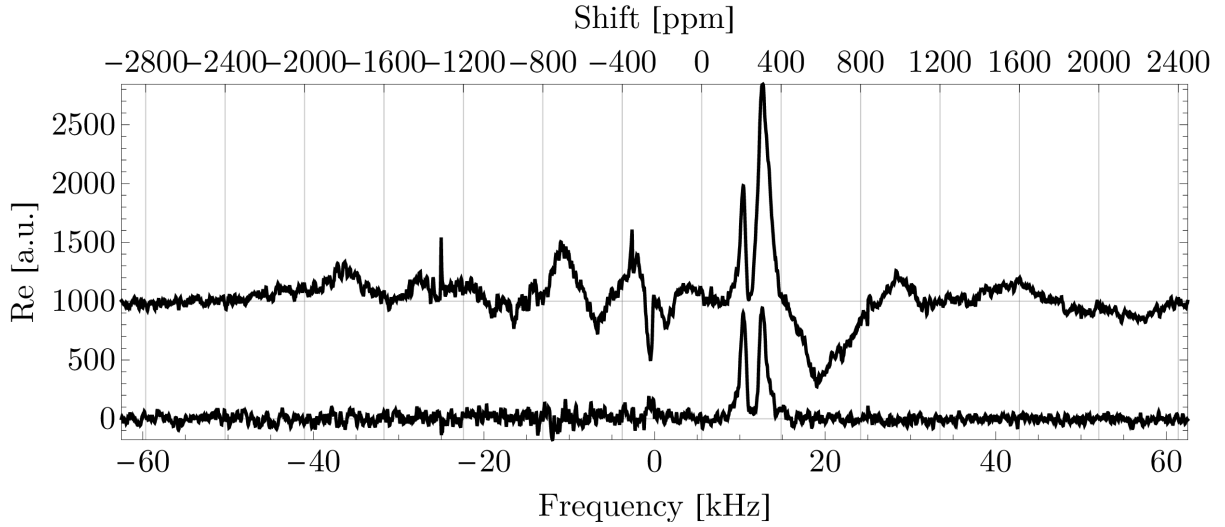


Figure 3.12: RIDE (lower curve) and no RIDE (upper curve, shifted by +1000 a.u.)— a comparison. Xe is dosed by 'fast dosage' on Cu(100) at 66 K sample temperature, measuring rate: 10/s. and 256 spectra are averaged per experiment, respectively. For the RIDE sequence: $\tau_R = 300 \mu\text{s}$. The peak pattern corresponds to a dynamically exchanged multilayer regime. Without application of the RIDE sequence, a spurious signal covers one of the NMR signals.

3.12 Determination of the Nuclear Polarization

High signal strength is an indication but not a sufficient quantity to determine the polarization of the ^{129}Xe ensemble. The total number of nuclei would be necessary which is not precisely controllable. Further, knowledge about the 'signal strength per nucleus' would be required. But this quantity is dependent on the sensitivity of the probe head which, in turn, varies with the temperature of the setup. Instead, a better way to estimate the polarization with less assumptions is to freeze the xenon to a dense film and make use of the change in the magnetic field due to the highly polarized nuclei since the nuclear magnetization is not negligible herein. This leads to a line shift in the ^{129}Xe resonance which can be quantitatively analyzed.

By applying a series of measurements using small tip angles for the readout the hyperpolarization is destroyed stepwise and so is the magnetic field arising from the nuclei themselves. Thus, the frequencies detected in the FID's shift gradually towards the equilibrium magnetization value, i.e. essentially zero.

The polarization dependent frequency shift was described by Candela et al. with the formula [55]

$$\Delta\nu = \nu - \nu_0 = A \left(3 \cos^2(\theta) - 1 \right) \gamma \mu_0 M \frac{1}{2\pi} \quad (3.1)$$

where ν is the momentary and ν_0 the equilibrium frequency. A is a form factor that has to be determined for the xenon film (see section 2.2.5). It holds $A = -1/2$ for a rotationally symmetric and infinitely expanded sheet [55]. Because xenon is frozen as a thin film with

the height of 3000 layers onto a round substrate area of 1 cm in diameter $A = -1/2$ is justified. θ is the angle between \mathbf{B}_0 and the symmetry axis of the sample. For our setup θ is set to 90° . The magnetization is $M = \mu n_s \eta P_z$ with n_s , the sample number density and η the isotopic abundance of the probe nuclei in the sample. Therefore, the polarization is

$$P_z = \frac{2\pi}{\gamma} \frac{1}{\mu_0 \mu n_s \eta} \frac{1}{A (3 \cos^2(\theta) - 1)} \Delta\nu = \frac{2\pi}{\gamma} \frac{2}{\mu_0 \mu n_s \eta} \Delta\nu. \quad (3.2)$$

Assuming an fcc crystal structure the density becomes $n_s = 4/a_0^3$, and thus the equation can be rewritten as

$$P_z = \frac{2\pi a_0^3}{\gamma^2 \hbar \mu_0 \eta} \Delta\nu. \quad (3.3)$$

As an example, here the used xenon has a ^{129}Xe isotopic abundance of $\eta = 0.99$ and a common sample temperature is 30 K. The lattice constant of xenon at 30 K is $a_0 = 6.14 \text{ \AA}$ [56]. Hence, the polarization can be calculated by

$$P_z \stackrel{T=30\text{K}}{=} \frac{\Delta\nu}{500.1 \text{ Hz}}. \quad (3.4)$$

Certainly, this estimate is criticizable because a perfect crystal is assumed whereas the true structure is unknown. A measure for the precision of the estimate can be deduced from the next section. Figure 3.13 shows a typical experiment to determine the nuclear polarization in a xenon film at 30 K.

Comments:

The polarization is determined to $P \geq 50\%$ regularly. By occasion it reaches higher values as it is the case in figure 3.13. Even Polarizations above 80% were measured in this setup [17].

The procedure in determining the polarization is criticizable, in respect to describing the line skewness, see sec. 2.1.7. Figure 3.14 suggests an underestimate of the polarization. Therefore, a suitable adjustment of the theory is proposed.

It was tried to find a temperature dependency of the line shift. The results are not conclusive but shown nevertheless in appendix D.4.

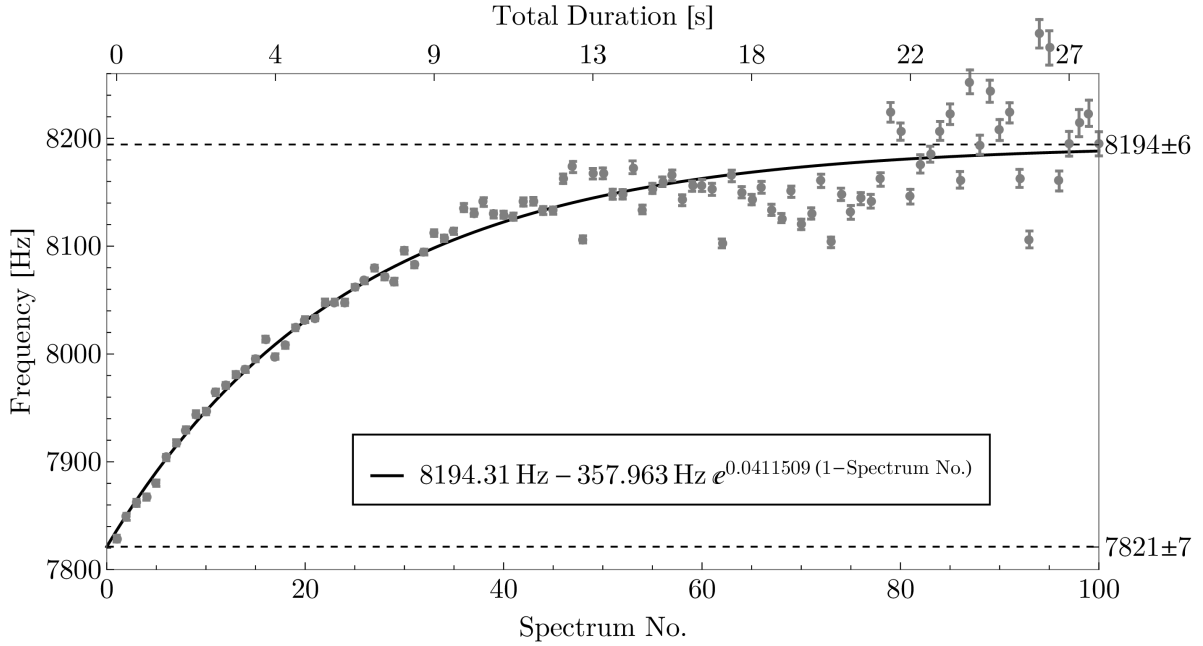


Figure 3.13: 'Common' polarization determination by application of a series of 15° -pulses and the respective readout. Lorentz functions were fitted to the spectral lines to determine the center frequencies f_c (dots). An asymptote was fitted to the f_c to extrapolate the frequency $f_s = (7821 \pm 7)$ Hz before the experiment and the frequency $f_e = (8194 \pm 6)$ Hz, where the number of spectra tends to infinity. The polarization is estimated to $P = (f_e - f_s)/500 = (75 \pm 10)\%$, with the precision given by the square root of the fit residual.

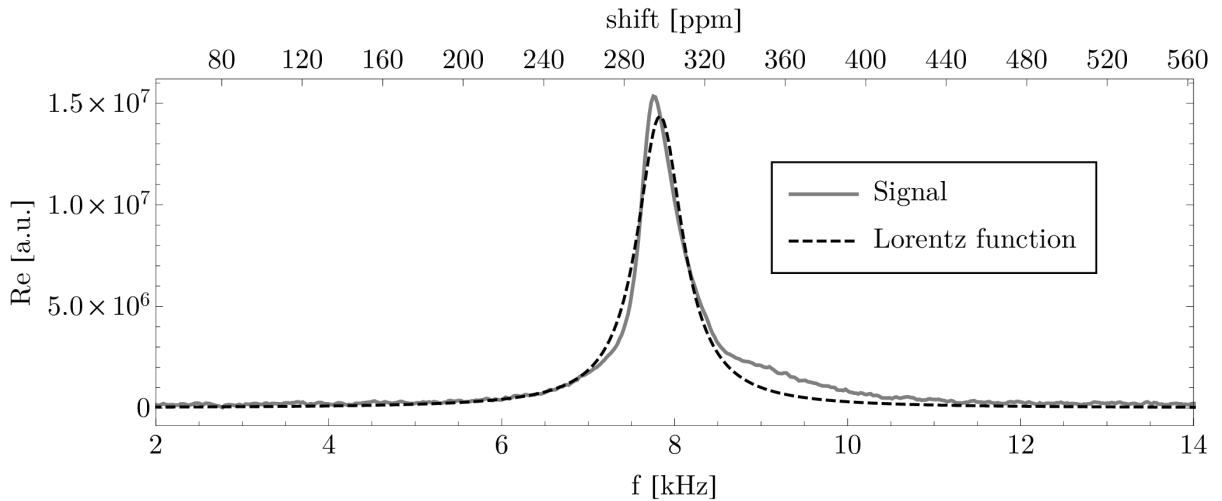


Figure 3.14: Justification for the use of the Lorentz function. Depicted is the first spectrum of fig. 3.13. By the effect of hyperpolarization, the NMR line is skewed, as mentioned in sec. 2.1.7. A better theory, than the Lorentz distribution, is necessary to describe the line shape in connection with the polarization.

Chapter 4

NMR at Single Crystal Surfaces

The following experimental series is focused on finding ^{129}Xe NMR signals in Xe monolayers on CO/Cu(100), Cu(100) and graphene/Ir(111). It is expected that ^{129}Xe , in contact with the pure Cu(100) metal surface, experience the influence of the metal electrons, probably connected to short relaxation times, i.e. broad NMR lines, and huge Knight shifts. This sample is of special interest because it is in opposition to Xe/Cu(111) [17], where the metal electrons affect the nuclei even more. In contrast, for ^{129}Xe on CO/Cu(100), the effect of the metallic electrons should be diminished. Here, mainly vdW forces and molecular motion on the surface are assumed to govern the spectra. However, little is known about ^{129}Xe on graphene/Ir(111). It can be metallic or not, occasionally dependent on the graphene sheet quality. A similarity of Cu(100) and graphene/Ir(111) might be the molecular dynamic within the Xe monolayer. That is, xenon can be present in a 2D-solid or 2D-gas phase when it is adsorbed on Cu(100) [57]. The same is valid for graphite(0001) [58] which might be comparable to graphene [59].

In order to perform NMR experiments on the specimens, hyperpolarized ^{129}Xe is applied as the probe. Xenon is dosed onto the samples with 40 ML/s, i.e. the 'fast inlet'. This rate was determined by [28]. The samples are cooled to suitable temperatures so that adsorption and desorption are in equilibrium. This way, ^{129}Xe is optimally exchanged after each measurement (which causes the loss of the hyperpolarization). So, after suitable waiting times the xenon monolayer is repolarized, allowing for a dynamic measurement. A RIDE sequence is applied for the NMR readout, to minimize artifacts arising from acoustic ringing and the like in the metallic substrates. The experimental procedure was chiefly the same for all samples.

However, measuring monolayers by NMR is a challenge! The methodology was approved at deep temperatures (see fig. 3.12), where fresh xenon is dosed on top of the already measured, and thus depolarized, one. Now, since the probed layer lies directly on the supporting surface, the old ^{129}Xe must desorb and freshly polarized xenon must adsorb in time before the next measurement. Thus, the measurement rate has to be adapted to the desorption and adsorption rates which in turn have to be chosen such that T_1 is long enough. While the NMR is performed the heating is interrupted, since the heating current broadens the lines in the range of kHz (see fig. 3.10). Chopped heating currents can cause

increased variations of the sample temperature. However, for an optimized exchange well controlled conditions are mandatory, since the desorption rate strongly depends on the sample temperature. So, the PID controller of the heater must adapt to each adjusted rate which occasionally demands for a new set of PID parameters. A range of temperatures need to be scanned since the optimum temperature for the adsorption/desorption equilibrium can only be estimated. If too extensive temperature changes are applied, the heating power and/or the duration need to be reset, and so forth. Besides, ^{129}Xe must be highly polarized and the sample must be kept clean. As a consequence the gas dosage has to be performed carefully. After all, no signal is acquired if any of these steps fails.

In order to break the cycle, a rather 'easy' study on $\text{CO}/\text{Cu}(100)$ is performed first because of the absence of metal electrons. Then Xe on $\text{Cu}(100)$ is measured. NMR on graphene is performed lastly because the creation of graphene implies the exchange of the substrate crystal. Due to the catalytic effect of the $\text{Ir}(111)$, the growth of large area graphene [29] works better on this surface than on $\text{Cu}(100)$ [60].

4.1 ^{129}Xe NMR in $\text{Xe}/\text{CO}/\text{Cu}(100)$

When ^{129}Xe is dosed on CO , its contact, to the metal electrons of the underlying substrate, is reduced. So, this 'free' xenon 2D-layer is a model for all other interactions mainly representing the effects of physisorption. The vdW interaction among the xenon atoms is dependent on the geometrical confinement of the system. Further the nuclear dipole fields at a surface differ from the bulk because of the reduced number of neighbors, the changed symmetry and the increased mobility.

The following experiment is conducted and evaluated in detail. Thus, this section shall also function as an example for the subsequent monolayer experiments.

4.1.1 Experiment

NMR on ^{129}Xe in a xenon monolayer on a CO covered $\text{Cu}(100)$ surface was performed. Therefore, the sample was cleaned and covered by a layer of CO as described below. By means of TPD the state of the sample was examined on the one hand; an appropriate temperature range for the dynamically exchanged xenon layer under 'fast dosage' conditions (see sec. 3.9) was estimated on the other hand.

Hyperpolarized ^{129}Xe was provided by the processes explained in section 3.8. By the principle of the 'fast dosage', i.e. by exchanging the liquid nitrogen in the dewar by liquid argon, xenon was dosed on the sample. The sample temperature per run was set to values of the range between 64 K and 72 K. During the measurements, the temperature could be regulated to the given values with an accuracy of $\Delta T = 0.5$ K. A RIDE sequence, consisting of part (I) and (II) shown in fig. 3.11, was used to acquire the signals.

The ppm-scale in the spectra was calibrated by the extrapolated final frequency of a previous polarization measurement, whereby the end-frequency was set to 321 ppm, i.e. the shift of the solid film.

Sample Preparation

The Cu(100) surface was cleaned by three sputtering/annealing cycles under the following conditions:

1.
 - Sputtering at room temperature with $(3.5 \pm 0.5) \cdot 10^{-5}$ mbar argon pressure^a and 1000 eV ion energy, corresponding to an ion current of approx. $2 \mu\text{A}$, for 40 min.
 - Heating up to 900 K^b for 10 min.
2.
 - Sputtering at 600 K with $(3.5 \pm 0.5) \cdot 10^{-5}$ mbar argon pressure and 800 eV ion energy, for 10 min.
 - Heating up to 900 K for 10 min.
3.
 - Sputtering at 600 K with $(3.5 \pm 0.5) \cdot 10^{-5}$ mbar argon pressure and 600 eV ion energy, for 10 min.
 - Heating up to 900 K for 10 min.

During sputtering the crystal was rotated regularly by an angle of $\pm 10^\circ$ with respect to the incident ion ray, every 3 to 5 min. After the purification process, Thermal Desorption Spectroscopy (TDS) was performed to check the cleanliness of the sample. Hereto, xenon with natural isotopic composition was used as a probe. Firstly, the substrate was covered by xenon at a pressure^a of $4.0 \cdot 10^{-7}$ mbar for 40 sec. at 30 K. Then the sample was heated up to 65 K and cooled down again to 30 K. Secondly, the sample was covered by the same dose $4.0 \cdot 10^{-7}$ mbar for 40 sec. again. Another time the sample was heated up to 50 K and cooled down again. The TPD was performed with a heating rate of 0.5 K/sec. whereat the desorption yield was recorded with a QMS set to $m/q = 129 \text{ u/e}$. For the further Thermal Desorption (TD) spectra the same procedure was repeated within the scope of preparation accuracy.

Immediately afterwards the crystal was covered by CO with a dose of $1.5 \cdot 10^{-8}$ mbar for 300 sec. at 90 K and another Xe- TPD was carried out. All mentioned spectra are depicted in figure 4.1. Here, the doses are given in units of langmuir: $\text{L} \equiv \text{torr} \cdot 10^{-6} \text{ s} = 1.33 \cdot 10^{-6} \text{ mbar} \cdot \text{s}$. The peak at 83 K is indicative of Xe on metallic Cu(100), it corresponds to the monolayer desorption. At 63 K the second layer desorbs and below 60 K the multilayer desorption is observed. Xe desorption from CO/Cu(100) does not show the metallic peak. The total amounts of Xe used is estimated to be 2–3 monolayers in both cases.

Then the NMR experiments were performed. Because the sample was heated up to approx. 140 K between every NMR experiment the state of the CO film was checked by TDS after the NMR series, though no signal from a metallic background could be found. However, an unusual increase of the xenon background pressure was noticed.

^ameasured by an ion gauge calibrated to N_2 , at a location approx. 15 cm distant from the gas admission and the sample

^bSince the temperature was measured at a remote point, and radiation is not included, a large error has to be considered

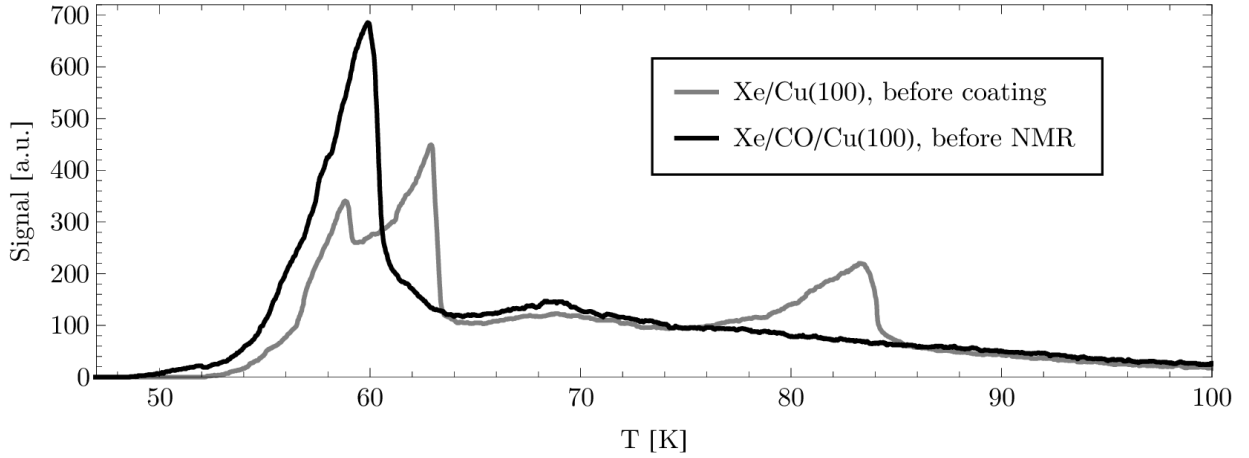


Figure 4.1: TDS: $\text{Xe}/\text{Cu}(100)$ and $\text{Xe}/\text{CO}/\text{Cu}(100)$, directly after cleaning and after coating with CO. Each dosage was: Dose (1): 4.2 L \rightarrow flash to 65 K \rightarrow cool down \rightarrow dose (2): 4.2 L \rightarrow flash to 50 K \rightarrow cool down. The heating rate was 0.5 K/s respectively. The peaks are explained in the text.

4.1.2 Results

A strong signal shifted by 315 ppm with respect to the xenon gas line was found for temperatures equal to and below 67 K. For higher temperatures this line seems to blur and to move to 340 ppm which differs from the Xe solid line. An even further increase of the temperature shows no significant effect. So the 340 ppm line is assumed to belong to a xenon reservoir situated on the sample holder which was identified later in the course of the experiments (see appendix C.2). Another signal at 215 ppm was measured distinctly between 64 and 66 K. It vanishes at temperatures of 67 K and above, analogously to the 315 ppm peak. The spectra at 62 K and 63 K are not shown in the graph, since they show essentially the same peak positions as at 64 K, but signal strength is excessively higher than in the other spectra. This is an indication for the Xe-film growth. Thus, a first simple interpretation for the found peaks is: 315 ppm is bulk like and 215 ppm Xe/Xe-film surface like.

Slight shift differences of the Xe/Xe-film and Xe-film peaks occur however in comparison to the low temperature regime. The origin could be that the bulk is less dense and more mobile which is why it is not unlikely that the bulk shift is less than 321 ppm. The same should be valid for the bulk surface. Instead, this peak has a larger shift than 200 ppm. An explanation has still to be found.

In the vicinity of 160 ppm is the sought NMR line. It appears in the range from 66 K to 70 K exactly when the other lines vanish. The coexistence of all 3 lines could be the result of small temperature variations in time. A small temperature dependent shift from 170 ppm at 66 K to 155 ppm at 70 K can be observed.

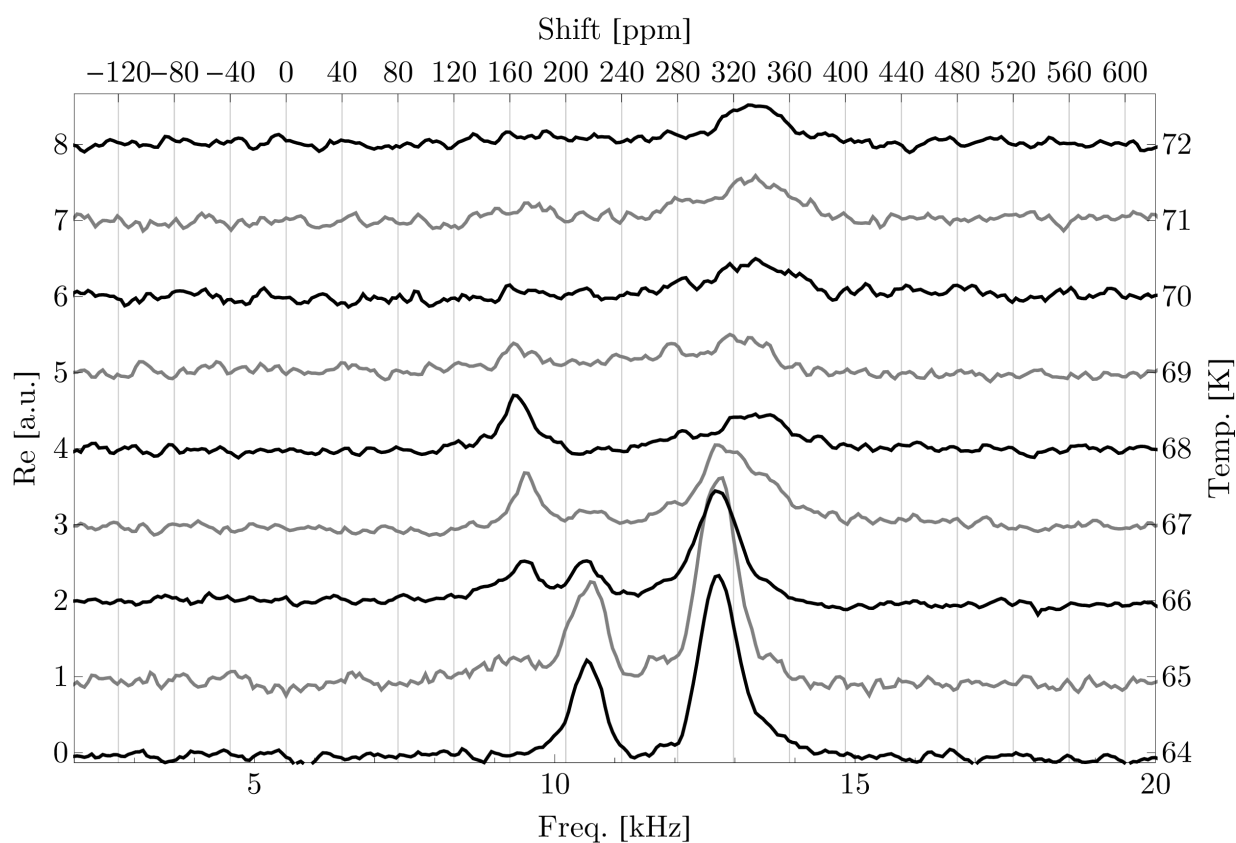


Figure 4.2: Xenon dosed on CO/Cu(100) with 40 ML/s. The acquisition rate is kept constant at 8.3/sec. The substrate temperature per run could be kept stable with an accuracy of $\Delta T = 0.6$ K respectively. For each curve a number of spectra, from 150 to 350, was averaged. The curves are shifted vertically by equal steps for clarity.

The spectrum taken at 68 K was used for the precise determination of the peak positions. 2 Lorentzian lines were fitted to the peaks, which is shown in figure 4.3. For higher temperatures the signal SNR was not sufficient to give precise statements.

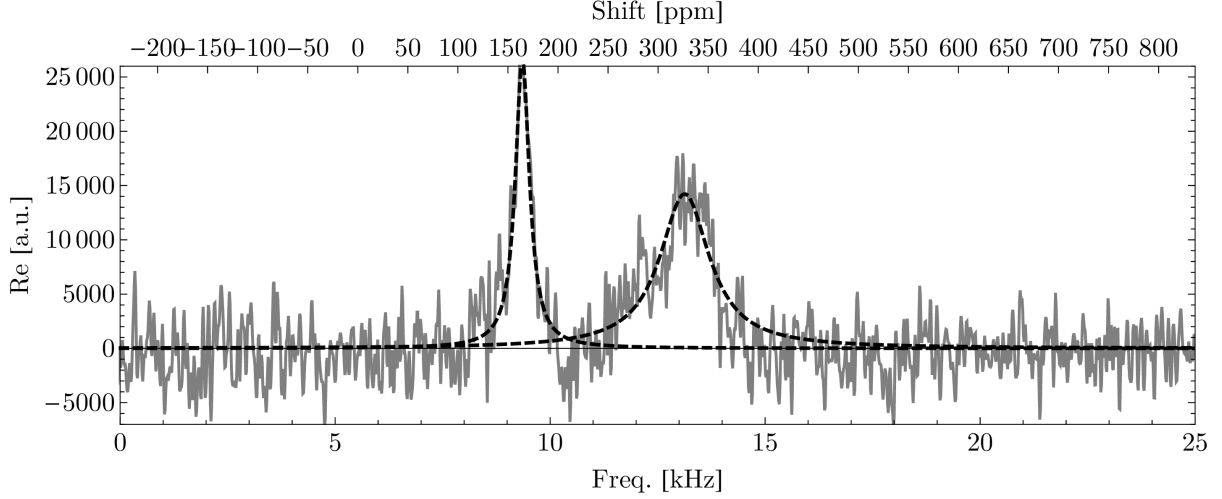


Figure 4.3: $\text{Xe}/\text{CO}/\text{Cu}(100)$ at 68 K in detail: Dashed lines are fitted Lorentzian functions. The left curve was fitted with $\sigma = (164.4 \pm 0.1)$ ppm and $\Delta f = 398 \pm 8$ Hz. It is symmetric in contrast to the right one. Yet, the right peak is disregarded since it is a feature from the background which is discussed later (see. app. C.2). The SNR (~ 6) is worse than in fig. 4.2 because a milder apodization (see sec. 3.7) was used for data filtering.

4.1.3 Discussion

A shift of approx. 155 ppm was found with $\Delta f = 400$ Hz. This result differs from $\text{CO}/\text{Ir}(111)$ [28], where the following parameters were applied: xenon (71% ^{129}Xe) 'slow dosage', $\sigma = 153$ ppm and $\Delta f = 136$ Hz. Beside the dissimilar crystals, another decisive difference is the dosing rate. Here, the 'fast dosage' was chosen which means a 10 times higher rate. Therefore, also a higher temperature has to be set to meet the required adsorption/desorption equilibrium condition ($R_A = R_D$) on the sample surface. Higher energy and faster dynamic of the adsorbate could be the reason for the far broader lines and also for the loss in signal intensity.

By utilizing formula (D.4) to estimate the temperature of the equilibrium $R_A = R_D$, one finds

$$T_{\text{eq}} = \frac{T_p \left[\ln \left(\frac{\nu T_p}{\beta} \right) - 3.64 \right]}{\ln(\nu/R_D)} = 71 \text{ K}, \quad (4.1)$$

with $\nu = 10^{13}/\text{s}$ and the parameters from the TPD in fig. 4.1: $T_p = 60$ K, $\beta = 0.5$ K/s, $R_D = 40$ ML/s. In comparison, the measured temperature was found at 68 K^c.

^cThe given temperature is not B-field corrected.

The desorption of the first, second and third layer of xenon from Cu(100) are connected to the respective peak temperatures at 83, 63 and 59 K in figure 4.1. The third layer peak temperature is comparable to the first layer desorption peak at 60 K of Xe/CO/Cu(100), wherefore a similarity could be concluded. Within the 3rd layer desorption regime, on the pure metal, a layerwise desorption could hardly be distinguished. Therefore, NMR signals from the 4th layer (that is the 2nd Xe-layer on CO) cannot be ruled out.

On the contrary the shift is less than the one of Xe/Xe-film which suggests a thinly occupied layer, here. The change in density might be connected to the development of the peak shift with increasing temperature, shown in figure 4.2. Except for the transition from 66 to 67 K, the signals do not shift stepwise but gradually connected with a strong broadening.

4.2 ^{129}Xe NMR in Xe/Cu(100)

4.2.1 Experiment

In order to perform the NMR measurement of the xenon monolayer on Cu(100) the full RIDE sequence drawn in fig. 3.11 was utilized. Apart from the deposition of CO, the preparation and experimental process was mainly the same as for Xe/CO/Cu(100) explained in section 4.1. Before and after the NMR experiments a TPD was performed respectively. A small temperature range slightly above the bulk desorption was scanned by NMR, as well as a wide temperature range in the vicinity of the monolayer desorption. While the NMR sequence was executed the set sample temperatures fluctuated with $\Delta T = 0.5$ K. Between every experiment the sample was heated up to 300 K.

The experiments were also performed at different B_0 settings and varied excitation frequencies, at selected temperatures, to confirm the found NMR peaks.

4.2.2 Results

Here only the results are presented and ad-hoc explanations are kept short. A detailed discussion can be found in section 4.2.3.

In the spectra of fig. 4.4, a peak pattern is visible within the temperature range from 86 K to 100 K. Against expectation, not only one peak but two, at 686.9 ppm and 772.4 ppm were found. Both signals show a temperature dependency within the estimated scope of desorption-adsorption equilibrium on the Cu(100) surface. The signals are shifted far out of the range of physisorption. Hence, these peaks are qualified to belong to signals from xenon in contact with metal electrons, i.e. they belong to the monolayer. In contrast, the broad and 'solid-alike' signal at approximately 320 ppm doesn't show any conclusive temperature related behavior. Additionally, a solid cannot not exist on the surface at the temperatures of the Cu-substrate. This peak is thus assumed to be connected to xenon adsorbed on the far colder sample holder which is examined further in appendix C.2.

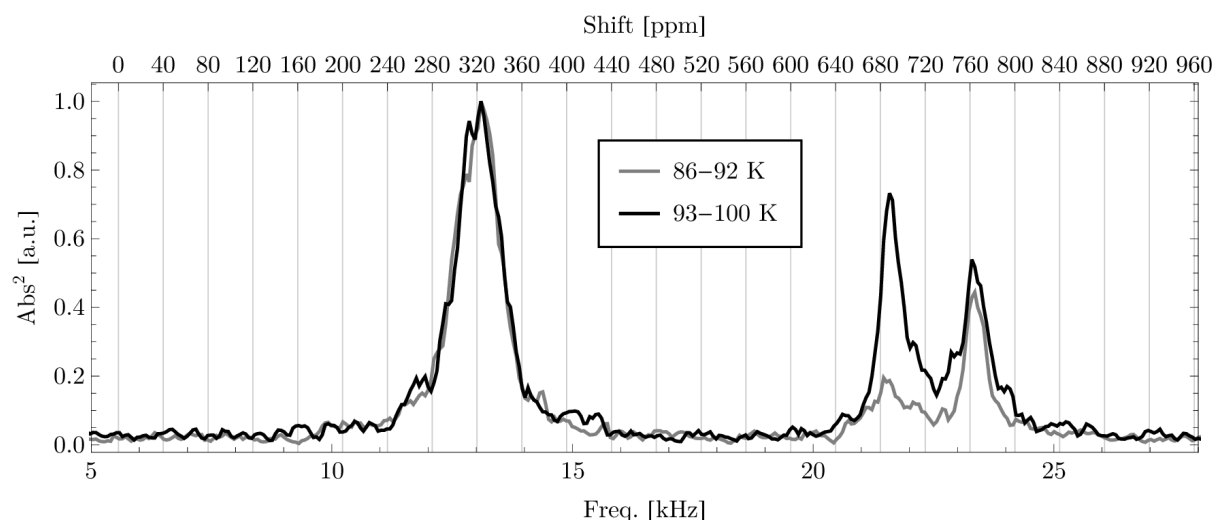


Figure 4.4: Xe monolayer signals on Cu(100). The spectra were acquired as explained in figure 4.6 and averaged over the temperature ranges given in the legend.

The TD spectra before and after the NMR experiments, which can be found in fig. 4.5, do not show any significant degradation of the surface quality and they give a good hint at which temperature a monolayer signal can be found. The temperature dependence of the adsorption/desorption ratio was probed by NMR and the results are shown in figure 4.6.

An overall decay of the surface signal intensity can be seen if one follows the chronology of the experiments noted by the numbers on the left axis of the plot. Since no striking difference in the quality of the TD spectra is seen the change of the conditions is believed to originate from the altered xenon impinge rate or the desorption rate: the increasing amount of xenon absorbs on the sample holder, therefore the cryo pumping effect is diminished^d. Also possible is the occurrence of water ice in the dewar which causes a bad exchange of the coolants ($\text{N}_2 \rightarrow \text{Ar}$) and thus an unregulated xenon flow.

The temperature range between 74 K and 83 K was probed randomly. No results are shown because the spectra only contain the 'sample holder signal' plus blurry unrevealing signals. In contrast, significant signals could be acquired at temperatures between 67 and 71 K which is shown in figure 4.7. Below 67 K it is possible to grow a voluminous structure with a far greater signal strength.

The xenon film surface signal at approx. 200 ppm is also visible. However the 200 ppm peak still exists at temperatures above the bulk desorption and a temperature dependent tendency to higher shift becomes obvious. At 70 K the signal is shifted to (235.2 ± 0.3) ppm and has a linewidth of 580 Hz, which was determined in app. B.1. Although the metal electrons do not affect this layer the SNR is worse than for the first layer, at temperatures

^dThe temporal change of the pressure conditions at the sample surface was known before. But, to defrost the sample holder wouldn't be a solution because then the sample must be cleaned again as well.

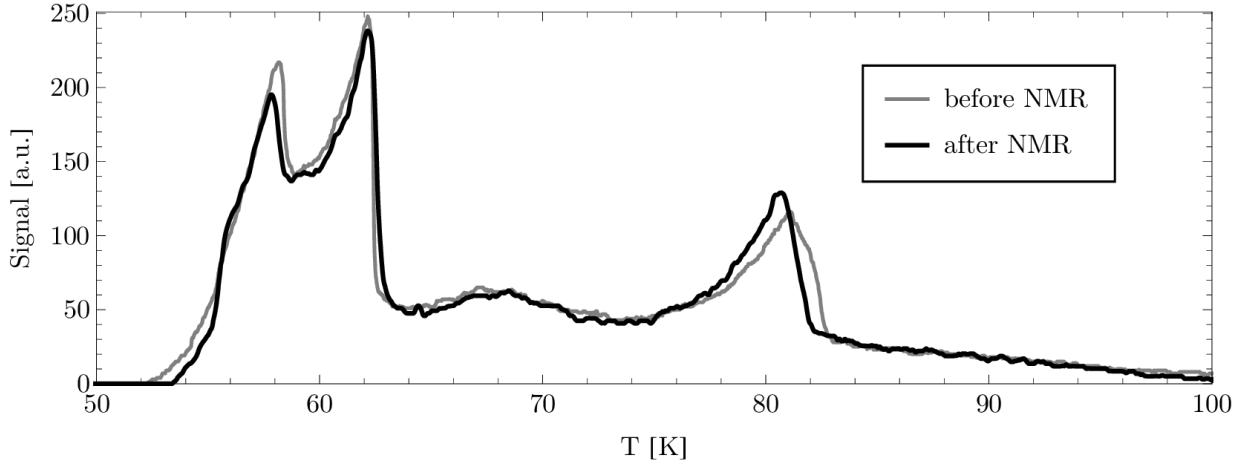


Figure 4.5: TDS: Xe/Cu(100). Heating rate: 0.5 K/sec. Dosage: Dose (1): 4.2 L \rightarrow flash to 65 K \rightarrow cool down \rightarrow dose (2): 4.2 L \rightarrow flash to 50 K \rightarrow cool down; respectively before and after the NMR experiment series. The cleaning procedure before NMR was the same as described in section 4.1.1. After NMR the sample was solely heated up to 300 K before TPD. Peak temperatures: 80.5 K (1st layer), 62.0 K (2nd layer), 58.0 K (3rd or higher layer).

of the monolayer desorption regime. Beside relaxant influences the signal strength can also be low because of a bad sample exchange of the probed layer. It is unclear, whether this is truly a signal of the second layer.

4.2.3 Discussion

Thermodynamic Considerations

In comparison to the experiment on CO the range of the adsorption/desorption equilibrium is far larger here. As already noted the pressure conditions change over the experimental time so that the equilibrium is shifted to higher temperatures. Here, the range of higher temperatures was recorded first. In contrast, the latter range shows systematically a less strong intensity. Nevertheless, the full scope of utilizable exchange truly reaches from 86 to 100 K where the optimum is expected to be at 96 K (see appendix D.2). Besides, the B-field influence on the temperature measurement has to be regarded.

It is possible to acquire a signal even if the optimized exchange condition, i.e the adsorption rate R_A equals the desorption R_D , is not matched. Even though the surface coverage is $\theta \approx 1$ when $R_A \gg R_D$ holds, occasional atoms desorb as soon as the characteristic desorption temperature (acquired from the TPD in figure 4.5) is exceeded. Incoming xenon atoms unlikely hit one of the emerged holes in the monolayer and it is not possible to form a second layer. However, the residence time t_R of an atom in the second layer is in the order of 200 μ s. This was estimated by applying eqn. (D.3) at $T = 90$ K with $T_p = 62$ K for the 2nd layer. Here, $R_D = 5000$ ML/s holds and R_D^{-1} is the mean residence time.

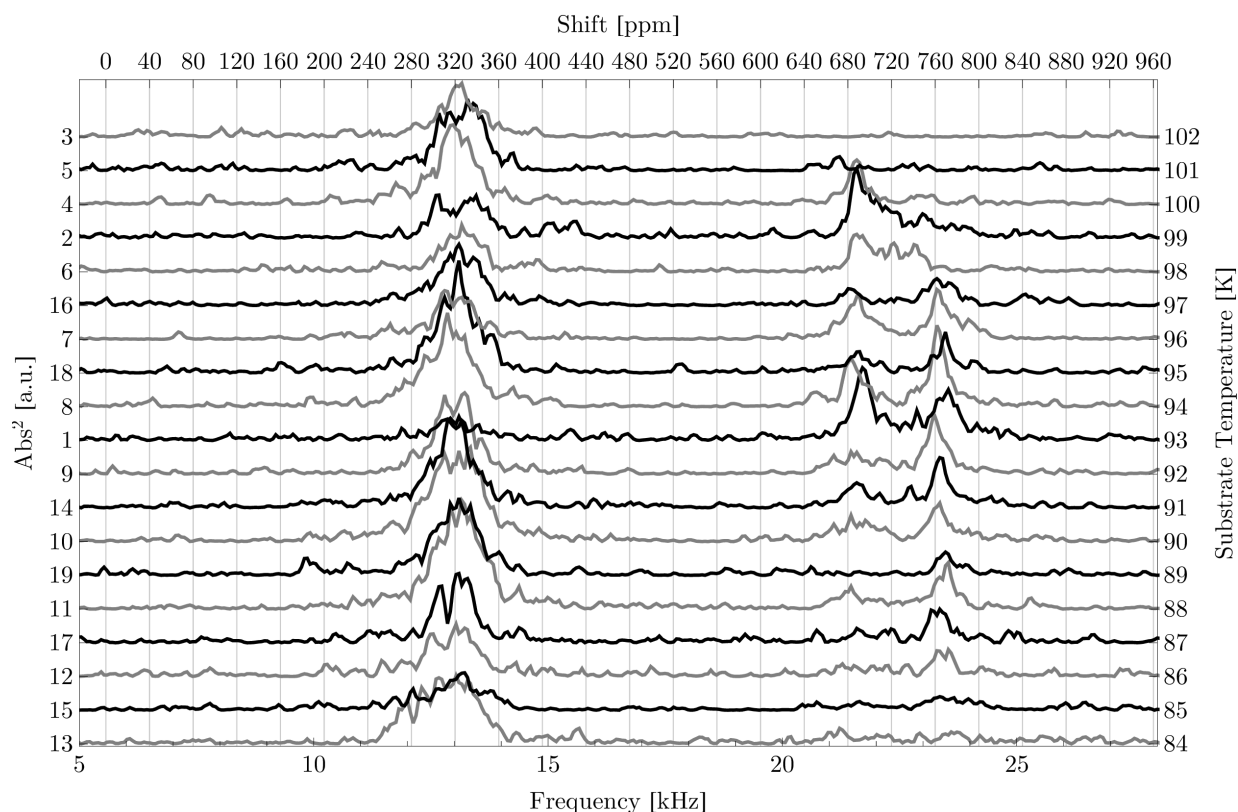


Figure 4.6: Temperature range of xenon dynamically exchanged on Cu(100): the numbers on the left ordinate represent the chronological order of measurement. For each temperature between 360 and 560 spectra are averaged. Approximately 8 spectra per second were acquired. The xenon monolayer was exchanged by desorption (temperature programmed) and adsorption (40 ML/s, provided by the unfreezing reservoir) in equilibrium. An overfilling of the layer is not possible. The signal at 320 ppm is an unavoidable background feature.

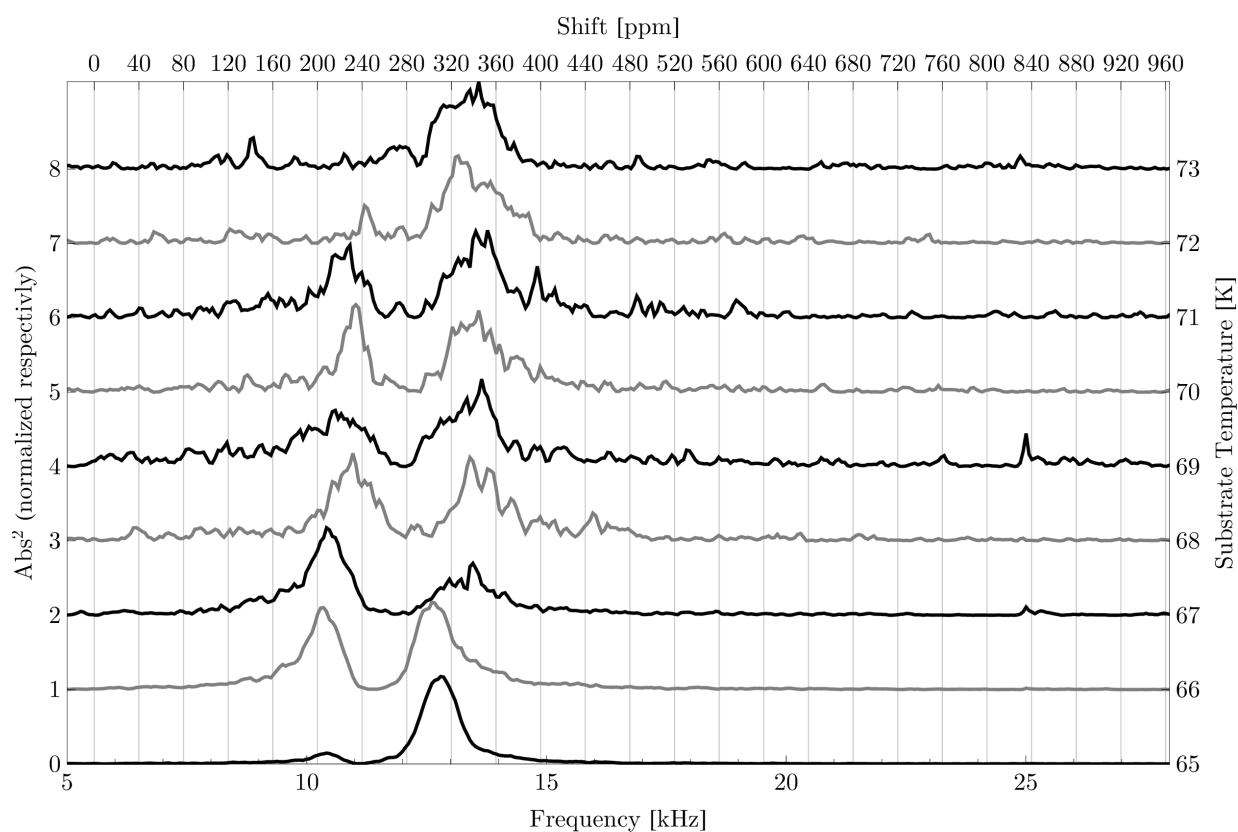


Figure 4.7: Xenon dosed on Cu(100) with 40 ML/s. Between 300 and 500 spectra were averaged per spectrum. The acquisition rate was varied between 6 and 8 spectra per second, to maximize signal strength.

At 90 K a ^{129}Xe atom has a velocity of

$$\bar{v}_{2D} = \sqrt{\frac{2k_B T}{m}} = \sqrt{\frac{2k_B 90 \text{ K}}{129u}} \approx 100 \text{ m/s} \quad (4.2)$$

on the xenon covered surface. There are 10^{14} [10] adsorption sites on 1 cm^2 available. So an atom visits

$$100 \frac{\text{m}}{\text{s}} \sqrt{10^{14}} \frac{\text{sites}}{\text{cm}} 100 \mu\text{s} = 10^7 \text{ sites} \quad (4.3)$$

during t_R . It is thus probable that a vacant spot is found and occupied by an atom from the second layer before the next measurement starts. In other words, the exchange rate is dominantly defined by the desorption rate within the temperature range below the optimized condition. Besides, it is not possible to probe the second layer because, firstly this layer is sparsely covered, for example at 90 K with

$$\theta = \frac{R_A/R_D}{1 + R_A/R_D} \approx \frac{R_A}{R_D} = \frac{40 \frac{\text{ML}}{\text{s}}}{5000 \frac{\text{ML}}{\text{s}}} = 0.8\% \quad (4.4)$$

and secondly the signal linewidth would be in the order of $1/(\pi t_R) = 1.6 \text{ kHz}$.

It cannot be claimed with certainty, whether or not $R_A = R_D$ was truly matched at a specific temperature within the range shown in figure 4.6. Though an increase in signal strength is a good hint, also the variations per experiment of the absolute amount of xenon and its polarization have to be considered, as well as the altering background pressure condition mentioned before. However, the relative intensities of the 'sample holder' peak and the monolayer signals reveal special events of the particle dynamics taking place on the surface because a bad exchange and short t_R cause a preference of the sample holder. On the opposite, if the sample holder peak intensity is relatively decreased, then the polarization must have been destroyed before, due to relaxation on the sample surface which means that t_R must have been increased.

In the thermodynamic regime where $R_A < R_D$ is valid, the signal intensity vanishes fast with increasing temperature. Above 100 K the coverage is insufficient to give a measurable signal.

Motional Narrowing or Coalescence of the Signals

Here it is assumed that the two signals arise from the presence of two different magnetic sites, called (1) and (2), with according differing resonance frequencies. In fig. 4.8, the temperature range was chosen in such a way, namely from 93 to 98 K, that the peaks have the same height. This was done in order to apply formula (2.51) which requires equal rates (and equal populations) from magnetic site (1) \rightarrow (2) and (1) \leftarrow (2). Additionally infinitely narrow lines have to be assumed which will be justified later, when all other contributions to the linewidth prove themselves to be negligible in comparison to the motional narrowing (or broadening).

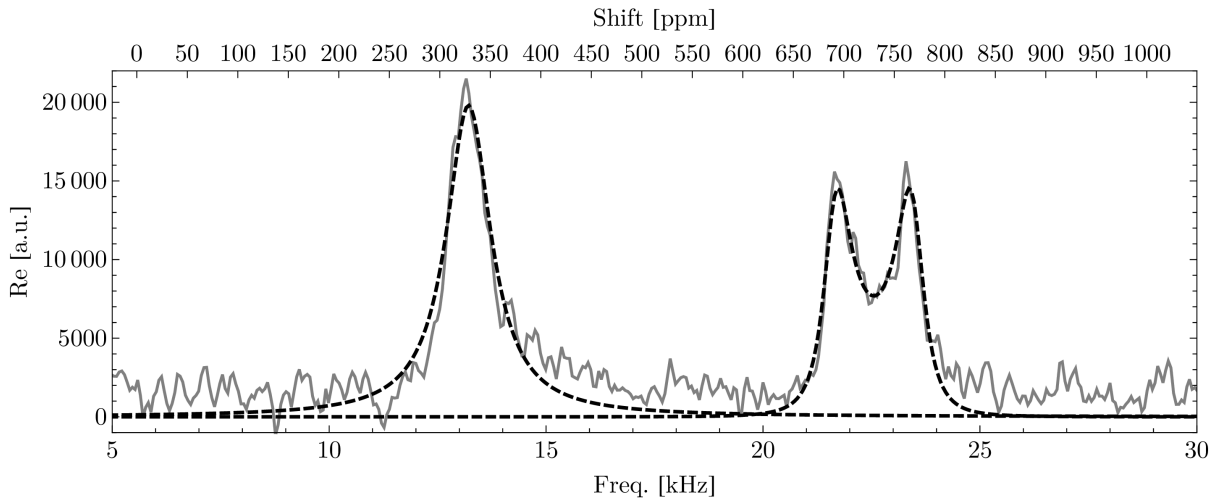


Figure 4.8: Xenon dosed with 40 ML/sec. on Cu(100) within the temperature range of 93–98 K. A Lorentz function is fitted to the curve on the left, whereas the dashed line, fitted to the coalescing peaks on the right, is based on eqn. (2.51).

By the fit parameters, the monolayer peak positions are determined to $f_1 = 21.56$ kHz, corresponding to a shift of $\sigma_1 = 687$ ppm, and $f_2 = 23.55$ kHz respectively $\sigma_2 = 772$ ppm. $\Omega = 394$ Hz is determined as the jump rate between the two magnetic inequivalent sites or a mean residence time $t_R = 2.5$ ms holds for a Xe atom at each of the sites. Considering the speed of a Xe atom of approx. 100 m/s, it is hardly believable that two signals are really resolved. By motional narrowing the peaks at 687 ppm and 772 ppm should have collapsed. A densely covered surface that suppresses the xenon movement could be an idea to explain this incident.

Order Phenomenon

Figures 4.6 and 4.4 suggest the existence of two regimes which are connected to the occurrence of either the 770 ppm peak alone at lower temperatures or both peaks, at 690 ppm and 770 ppm, at higher temperatures. This deviation of 80 ppm and the chemical shift of 120 ppm of a free standing and fully coordinated xenon layer [61] are comparable since the shift is strongly coverage dependent.

Regarding the dynamics of the measurement, the surface is almost fully covered at low temperatures where xenon is known to form 2D-solids ('islands'). These islands must be unstable and porous at the given temperatures, otherwise the exchange of xenon gas wouldn't be possible. Thus the 770 ppm peak is probably connected to xenon islands with vacancies.

At higher temperatures and less coverage the Xe density on the surface diminishes whereas mobility and length of path grow. Within this temperature scope the existence of xenon 2D-gas is possible [62]. Both reservoirs, i.e. the 2D-gas and 2D-solid, can exchange atoms by adsorption and desorption respectively. Therefore both states have a chance to

be detected simultaneously. Besides, little is known about the diffusion on the surface. Also the 2D-gas and the 2D-solid can interchange atoms. If this process is too fast, xenon at the island edges and in the 2D-gas phase cannot be distinguished. But the interior of an island is isolated from the in-plane dynamic. Thus, the emergence of two resolvable signals is possible. It is questionable whether the amount and the residence time of xenon in the 2D-gas phase are sufficiently high to surpass the detection threshold. So, the line at 690 ppm is believed to be connected to island edges or to a 2D structure with less density.

Possible adsorbate structures are shown in figure 4.9. For comparison, the chemical shift of xenon dimers is estimated to be between 20 ppm [63] and 40 ppm [37] assuming a distance of 4.5 Å which is the displacement between two xenon atoms on a Cu(100) [64]. When the distance is increased by 1 Å the chemical shift is reduced by 100 ppm.

Korringa Relaxation Estimate

Both peaks, disregarding the origin, belong to ^{129}Xe that is mainly shifted by the Knight shift K . All influences on the nuclei are small and therefore additive. So K can be estimated by subtracting the physisorption effects. I assume that a free standing 2D xenon layer is shifted comparable to 155 ppm as it was suggested from the spectra of Xe/CO . If these cases behave similar on the Cu(100) surface then the Knight shift can be estimated to

$$K \equiv 770 \text{ ppm} - 155 \text{ ppm} = 615 \text{ ppm} \quad (4.5)$$

With these estimates the lattice relaxation time T_1 can be derived by using the Korringa relation from eqn. (2.42) which is additionally corrected by applying a factor of $B = 0.9$ for non ideal conditions explained in [14]. At $T = 95 \text{ K}$ the relaxation time becomes

$$T_1 = \frac{\hbar}{4\pi k_B} \left(\frac{\gamma_e}{\gamma(^{129}\text{Xe})} \right)^2 \frac{1}{K^2} \frac{1}{T} B = 85 \text{ ms}. \quad (4.6)$$

Besides, this explains why an experiment applying the 'slow dosage' ($\sim 4 \text{ ML/s Xe}$ flow) is not possible because in the adsorption/desorption equilibrium an Xe atom remains 250 ms on the surface. Thus, it loses its hyperpolarization before the NMR measurement.

Additional Checks

In order to demonstrate the signals to be true NMR answers and not additional features arisen from the background, a series of supplementary examinations was conducted, starting from the research on the 'sample holder' peak origin, which can be found in the appendix C.2. Also the field dependency was examined, i.e. B_0 was shifted and the monolayer experiment was performed under similar conditions on the one hand. The results are relocated to the appendix A.1.1. On the other hand the experiment was performed with an alternated excitation frequency wherefore the findings are presented in app. A.2.1. Further, the emergence of the signal was connected to the xenon gas flow which can be

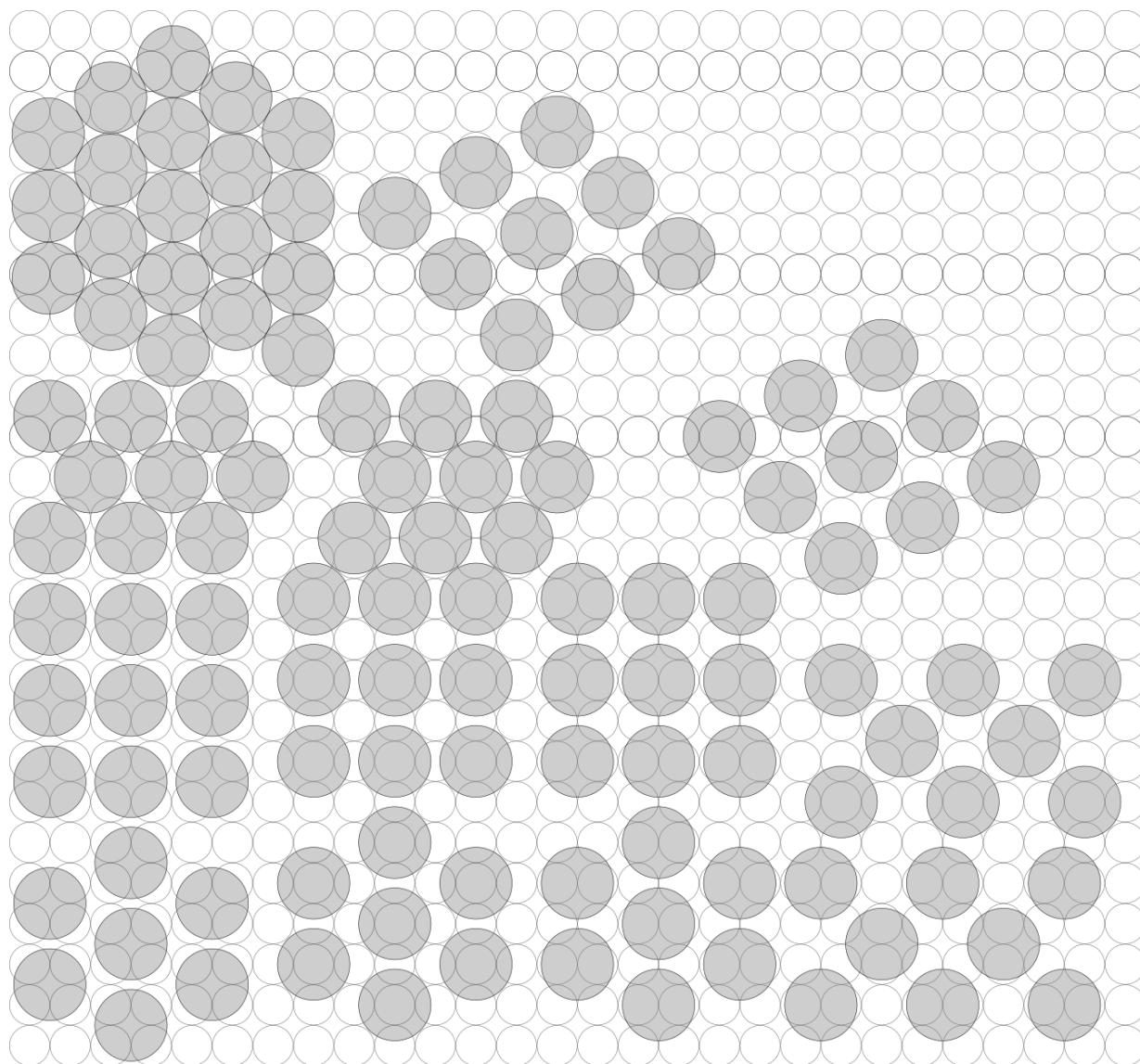


Figure 4.9: Xe/Cu(100)-adsorbate structures. Cu-Cu distance: 2.53 Å[65], Xe-Xe distance (incommensurate): 4.50 Å[64]

claimed, although not shown here, because the xenon dosage was nested in the duration of the NMR sequence, so that empty spectra were acquired before and after the dosage. Thus, artifacts from the electronics can be neglected.

The outcome of the checks prove the signal at 770 ppm to be robust. In contrast, the peak at 690 ppm was unsteady which is ascribed to deviations in the preparation process, varied hyperpolarization, from day to day, or the badly controlled pressure conditions. Additionally, the cleanliness could not be controlled while the NMR was performed whereas conspicuous features did not arise in the TPD examinations before and after the experiments.

4.3 ^{129}Xe NMR in Xe/Graphene/Ir(111)

4.3.1 Preparation

The Ir(111) surface cleaning procedure follows [29, 66] and the CVD growth process of graphene was inspired by [29, 31]. In particular, the synthesis is described in the appendix D.1. The final result was checked by TPD and is compared to the pure Ir(111) surface in figure 4.10.

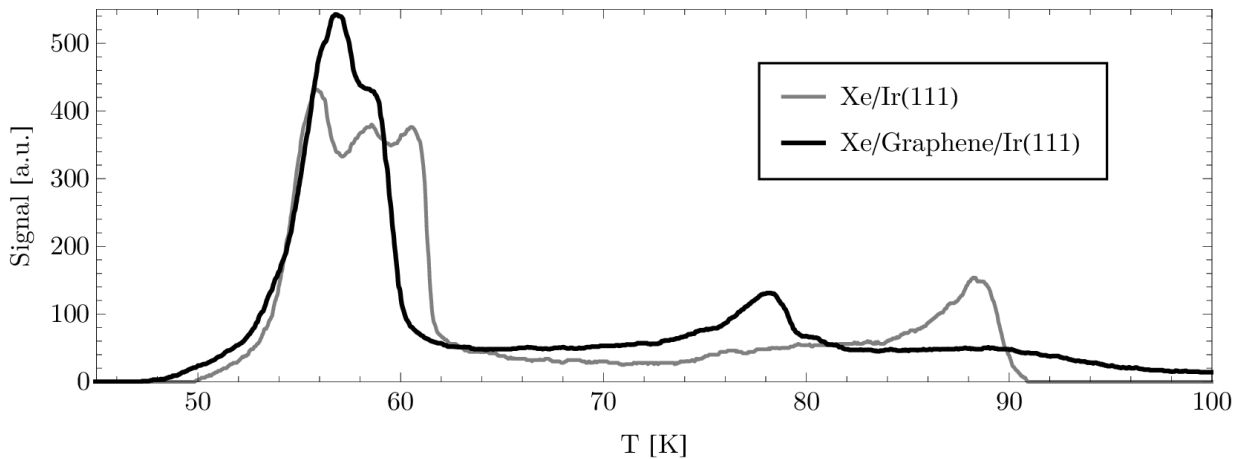


Figure 4.10: TDS: Xe/Ir(111) and Xe/Graphene/Ir(111); before and after graphene synthesis. Each dosage was: Dose (1): 4.7 L → flash to 70 K → cool down → dose (2): 4.7 L → flash to 50 K → cool down. The heating rate was 1 K/s respectively.

In the TD spectrum of Xe/graphene a signal in the range between 80 K and 95 K could be seen. It is probable that it belongs to the xenon desorption from remaining metallic areas. However, one has to keep in mind that the sample was exposed to air (see app. D.1). Compared to [28, 67] the qualitative similarities are obvious. On the contrary, a systematic temperature deviation from the literature arises which can be compensated by subtracting approx. 4 K from the given temperature scale.

4.3.2 Experiment

The experimental procedure was the same as on Cu(100) described in section 4.2.1. Because the TPD spectra showed no significant change in quality, within a period of several days, the sample cleaning before the NMR was confined to a mild heating. In particular, the substrate crystal was heated to 300 K before every experiment.

4.3.3 Results

A series of NMR experiments was performed at various temperatures and the spectra of the expected temperature regime were averaged. Thereby, a signal could be found which is shown in fig. 4.11. The ^{129}Xe resonance shift is to $\sigma = 173 \text{ ppm}^e$. At temperatures

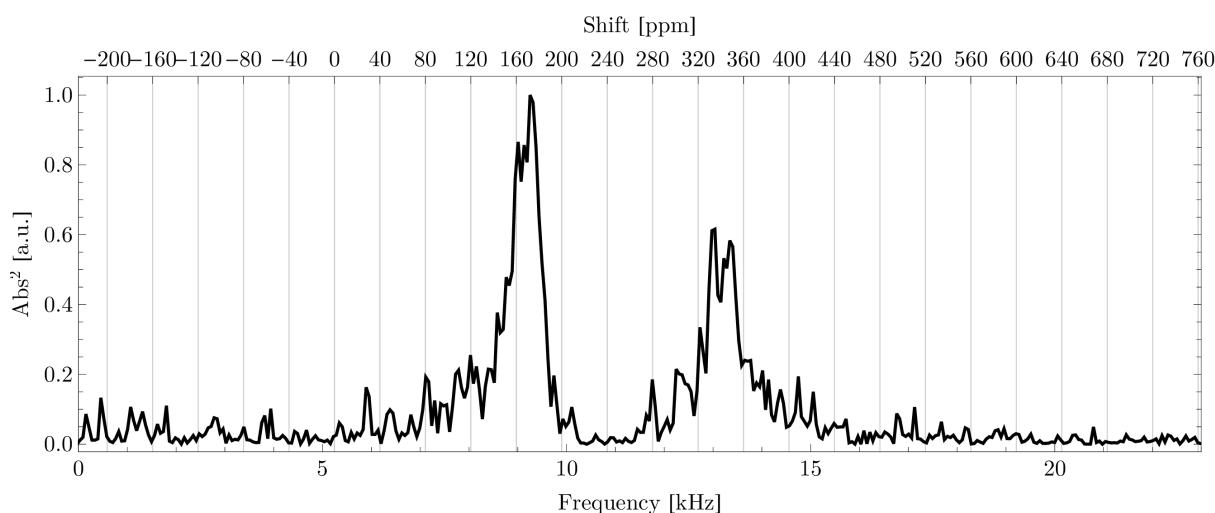


Figure 4.11: Xe monolayer signal on graphene. This is the spectrum averaged over the temperature range from 82 K to 95 K. The peak on the left is the sought signal, whereas the right one is the sample holder peak discussed in app. C.2. The explicit spectra per temperature can be found fig. 4.12.

above 80 K only the xenon monolayer can exist on the graphene under these conditions. Thus, the xenon is in direct contact with the sample surface. Similar to the preceding experiments, the signal of the sample holder is also visible.

A demonstration of the individual spectra per temperature can be found in figure 4.12. Here, the signal is visible, albeit signal strength is low. Up to now, it can only be speculated about the reason of the low intensity. Imperfections of the graphene sheet, such as dangling bonds, might be a probable explanation. Linewidths are approximately 200 Hz (determined in app. B.2), which is not in contradiction to the broad (average) line in fig. 4.11. The solution is a drift of the line, tending to lower shifts with increasing temperature.

^eA discussion about the precise determination of this value is given in the appendix B.2.

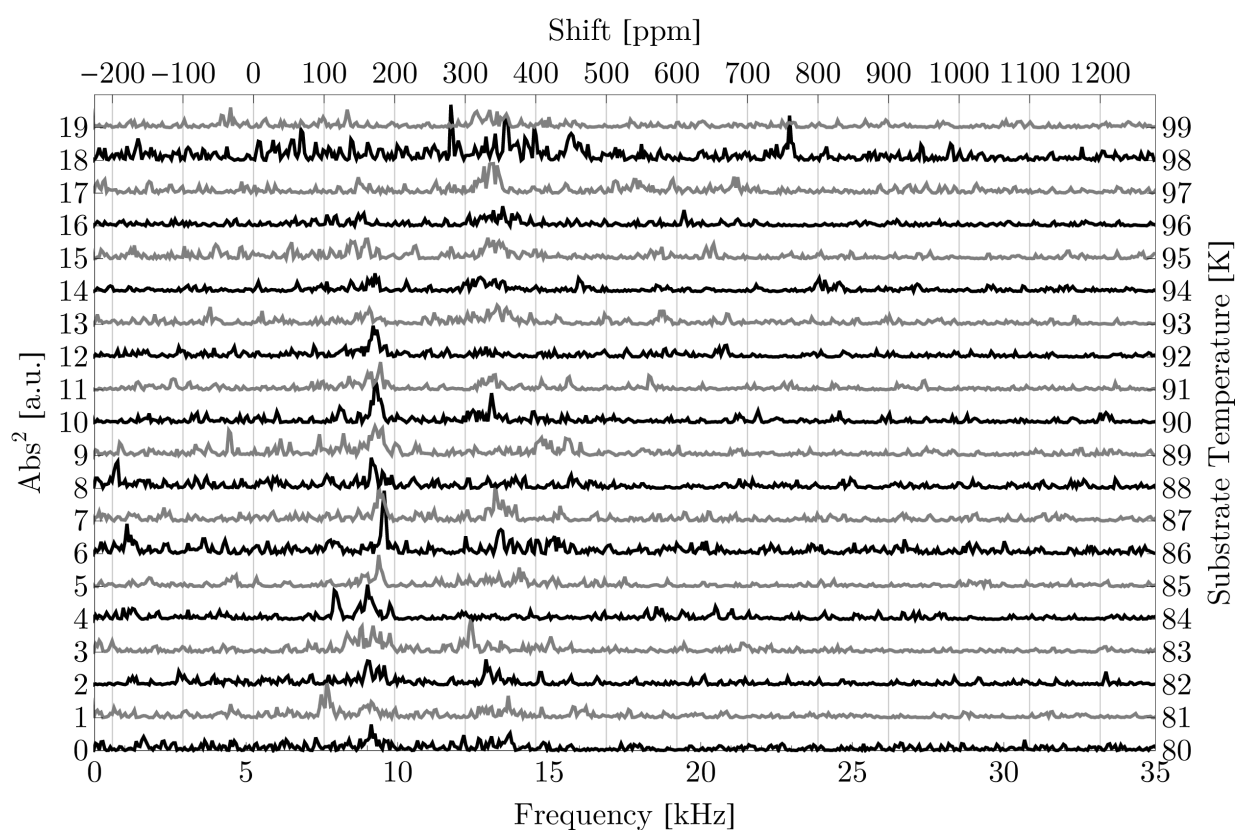


Figure 4.12: Xenon on graphene dosed with 40 ML/sec. The RIDE sequence, depicted in fig. 3.11, was utilized for readout. 8.3 spectra per second were measured and approximately 600 spectra are averaged for each substrate temperature shown. A signal could be found. The reason for the low intensity is unknown.

By the TD spectrum of figure 4.10 the peak temperature of $T_p = 78$ K and the heating rate $\beta = 1$ K/s are acquired. These values are used in eqn. (D.4) to calculate the temperature $T_{eq} = 91$ K of the desorption/adsorption equilibrium. This estimate fits well with the highest signal intensity of the NMR results that are shown in figure 4.12.

Further checks of the here presented results are postponed to the appendices A.1.2 and A.2.2.

4.3.4 Discussion

The shift is in the range of physisorption. A Knight shift of ^{129}Xe adsorbed on a metallic surface as it can be seen on Cu(100), or in other works [28, 17] was not detected. Thus the electrons of the graphene are not influencing the xenon nuclei in the fashion of a metal. Quite the contrary is the case, namely, the displacement by the graphene layer protects the xenon from the metallic electrons of the Iridium substrate.

The signal intensity is lower than in the spectra of Cu(100) or CO/Cu(100). Failures in the SEOP process or the xenon gas transfer are an unlikely explanation since the polarization was determined to approx. 60% in a preceding measurement and, as already explained, the polarization is reproducible over several experiments.

Signal loss can also arise from a poor B_0 homogeneity that has to be checked after each change of the sample. However, even at a site in 2 cm distance from the center, the magnetic field is still sufficiently uniform to resolve the signal from the sample holder.

Another reason for low signal strength could be a low adsorption rate. However, the xenon admission is well controlled and it is known that approx. 90% of the incoming xenon gas collides with the probe surface first, before it can travel to other adsorption sites in the UHV chamber [35]. An argument against an insufficient wetting behavior is the broad temperature range in which a signal could be detected, in contrast to Xe/CO. So, even if the impinging gas could not stick to the surface, for any reasons, then the sample holder would be favored. But an increase in the sample holder signal intensity was not observed.

It is thus assumed that a strong relaxation mechanism takes place on the graphene surface. A probable relaxation agent is realized by electrons that are strongly correlated with the nuclei, for instance at paramagnetic centers. In contrast to the Pauli paramagnetism, the localized electron spins cause an additional field in order of 1 kG in an atomic distance effectively. Not before ten atomic distances the influence on the nuclei is diminished. Xenon atom movement in such a zone leads to a fast dephasing. Electrons are a main source to nuclear relaxation. But, even though the electrons do not relax the nuclei, the strongly inhomogeneous field would result in such broad lines that a detection was made impossible. So, the presence of such a center is equivalent to a dead area for the NMR measurement. Many of such spots could decrease the effective sample surface area.

In crystals paramagnetic centers arise from imperfections, i.e. vacancies or defects. An imperfect graphene sheet was hinted by the absence of the characteristic pattern in the LEED spectra. In particular, after the preparation the spots connected to the Ir(111) substrate were weaker than before but no adsorbate superstructure, i.e. the typical moiré pattern, was observed. Nevertheless, a carbon structure must have been created on the

surface which was detected by means of TPD whereby a comparable desorption characteristic to single crystal graphite [58], highly oriented pyrolytic graphite [68] and graphene itself [67] was found.

Thinkable defects in graphene are, for instance, grain boundaries or dislocations [69]. These are however nonmagnetic since no unbound electrons occur. Rather suspicious are vacancies, dangling bonds and island edges. Electron Paramagnetic Resonance (EPR) and Density Functional Theory (DFT) studies [70] reveal a tendency to magnetism, especially when O_2 is adsorbed at these places. However, at the prevailing temperatures oxygen could not stick to graphene [71]. Further, the graphene electron states are strongly hybridized with the Ir(111) surface states [72]. The very same is valid for the carbon atoms at the edges [73].

It is possible that the graphene was degenerated already during the creation process because of the inevitable exposure to air (explained in the appendix D.1). If the graphene sheet was not grown in large sheets but in small islands, a reaction of the island edges with oxygen cannot be ruled out. Recent investigations [74] show that these oxidized edges cannot be recovered before heating up to 1500 K. Furthermore these edges are known to develop a manifold of magnetic properties.

Further knowledge about the sample must be gathered to make conclusions about the observed interactions.

Chapter 5

Order Phenomena on and in Xenon Films

This chapter shall give complementary material to the found results of the forgoing experiments.

Firstly, the topmost layers of xenon films are probed by NMR in a similar manner, as applied in chapter 4. That is, ^{129}Xe is hyperpolarized and dosed onto the substrate crystal with 4 ML/s, also called the 'slow dosage', or with 40 ML/s, called the 'fast dosage'. Here, the difference to the experiments before is that the substrate temperature is kept below 50 K. So, the desorption of the xenon becomes negligible and a film grows on the substrate. During the dosage, NMR measurements are performed periodically with constant time steps. So, only the topmost layers are probed since the interior layers are depolarized due to the previous measurements. This procedure was described in section 3.10 and the principle of measurement is depicted in fig. 3.8.

One goal of this experiment is to find regular structures, for example step edges, within the xenon surface layer and representative NMR lines. This could bring insight on the effects of physisorption and the connected chemical shifts. Therefore the applied RIDE sequence has to fulfill the following demands: At low temperatures, the acoustic ringing is encouraged due to the reduced electrical resistance in the metal substrate, comparable to eddy currents. Further, ^{129}Xe is not probed in a monolayer but on a solid. Hence, dipole dipole interactions between the nuclei have to be regarded because of the increased number of neighbors and the higher density. These interactions mainly cause the invalidity of the Bloch equations, i.e. NMR pulses do not reorient the magnetization by ideal angles but rather by an angle distribution, due to local field inhomogeneities. The consequences are broadened lines and dephasing. So, on the one hand the RIDE sequence has to compensate the amplified ringing. On the other hand, it has to be robust against badly defined pulse angles.

Secondly, the inner structure of the xenon film is probed. Another approach to interactions with the nuclei is the study on the linewidth. The dipole dipole interactions govern all other broadening effects in a solid, although the hyperpolarization reduces the

linewidth. In order to make the influence of the vdW forces and the underlying structure visible, dipole dipole interactions are diminished further by dilution of the ^{129}Xe (spin 1/2), with ^{132}Xe (spin zero).

5.1 Xenon Film Surfaces

Here, the xenon film surface is measured by Xe-NMR, or to put in other words: the xenon crystal is probed layer by layer during the growth. Since the film thickness is about 2000 layers, only the growth of the first few layers should depend on the choice of the substrate, which is undetectable within the measurement. This is due to the fact that the acquired spectra have to be averaged to raise the signal above the thermal noise level. Two kinds of growth speeds are applied, namely 4 ML/s and 40 ML/s, which are defined by the xenon dose rates explained in section 3.9. Further the influence of the substrate temperature on the growth is examined.

5.1.1 Experiments

The substrate in use was graphene/Ir(111) which was cooled down and held at 25 K. ^{129}Xe was hyperpolarized and provided for the NMR measurement by the regular procedure explained in the sections 3.8 and 3.9 respectively. A simplified RIDE sequence, consisting of part (I) and (II) seen in fig. 3.11, was applied to acquire the data. Before every sequence a 90°-pulse and a delay of 82 ms(= FID acquisition time) was applied to depolarize the xenon that accumulated between the experiments, hence called: Depolarization pulse^a.

1. The procedure was repeated several times. The measurement rate, which is mainly defined by the time of acquisition and the time between the depolarization pulse and the according RIDE partition, was varied within the first runs. Thus, the effective detectable layer depth was varied accordingly. In this process, the heating current was not used. Here the xenon was dosed with 4 ML/s.
2. In the later runs the rate was kept constant and heating periods were introduced after each acquisition when other than the lowest attainable temperature was used. Again, the Xe dosage of 4 ML/s was chosen.
3. For comparison, similar experiments were performed with 40 ML/sec xenon dosage without heating. Hereby the measurement was started before the liquid argon was poured into the dewar and the xenon flow wore off before the measurement was stopped. As a consequence the first and the last files of the range of acquired data are lacking of signal intensity. Thus, only the files in the middle were selected for the signal averaging.

^aIt was not dared to use a 90°-pulse train to erase the polarization or remaining transversal components because of the introduction of additional complicated ringing artifacts

5.1.2 Results and Discussion

Figure 5.1 shows unambiguous signals for all used measuring rates. Hence, further counter checks of the signal reliability are spared. Because of the low temperature and the position of the crystal in front of the doser it can be assumed that the xenon mainly sticks to the crystal's front side without noticeable loss. This was tested by [35] in an experiment applying a field gradient over the crystal, so that signals from the front and back site could be distinguished.

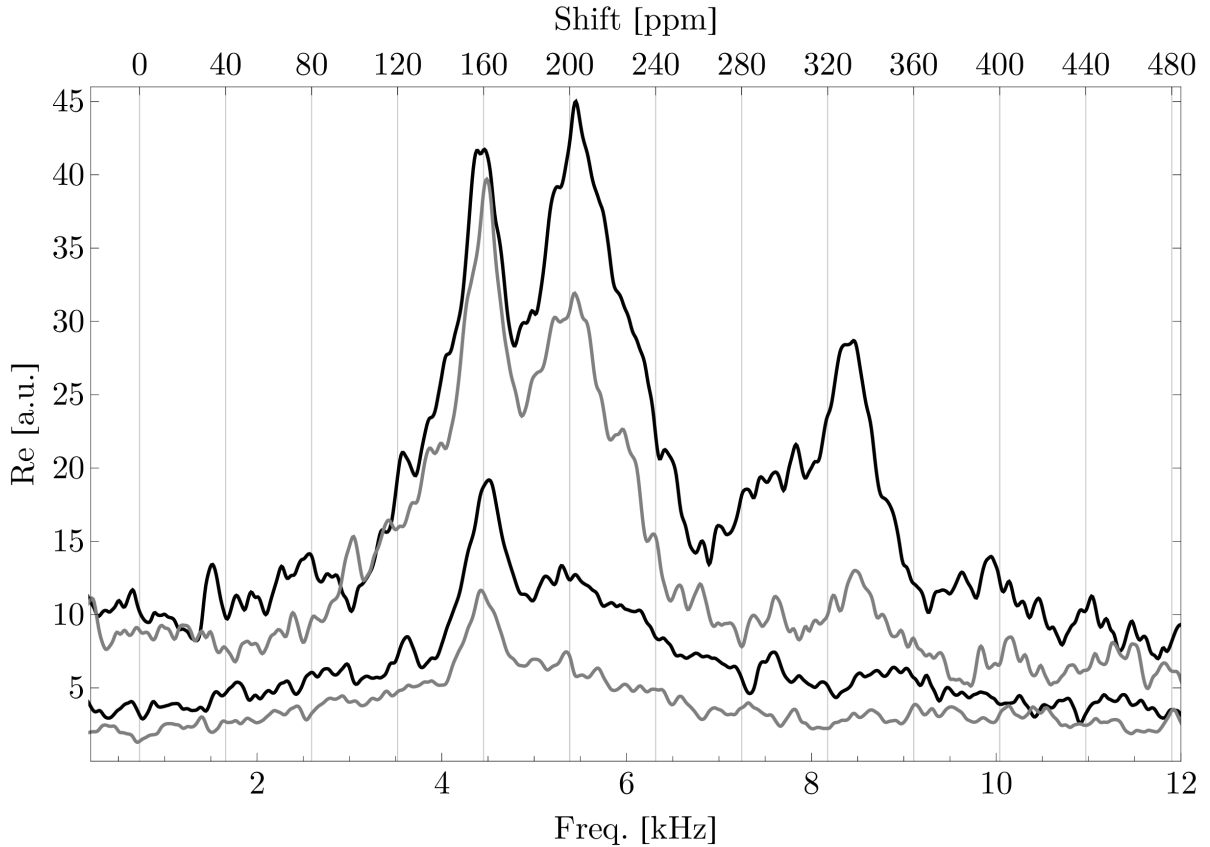


Figure 5.1: Xenon dosed on graphene/Ir(111) with 4 ML/s. The substrate temperature was $25 \text{ K} \pm 0.5 \text{ K}$ (without B-Correction). Measurement by a depolarization pulse followed by a simple RIDE sequence. From top to bottom, the curve parameters (number of averaged spectra, acquisition rate) are respectively: (512, 0.9/sec), (960, 1.6/sec), (2096, 4.4/sec), (3664, 7.3/sec). The curves are shifted vertically by equal steps for clarity.

The xenon dosing rate decreases only slightly as long as a huge amount of xenon is stored in the cool trap, and the rate is well reproducible from experiment to experiment which shows up here as well as in earlier works [28, 35, 17]. Also the total durations of intensive gas flow, namely $(15 \pm 1) \text{ min}$ for the slow dosage and $(70 \pm 10) \text{ sec}$ for the fast dosage, do not vary significantly from experiment to experiment. Therefore, the previously given impinge rates are assumed to be valid for this experiment and also the following ones.

Figure 2.3 of sec. 2.2.1 can be utilized to interpret the visible lines of fig. 5.1. In the top most graph of fig. 5.1, a peak at about 320 ppm can be identified as the signal from xenon nuclei located in a bulky structure. Two more peaks can be seen shifted by 156 ppm and 203 ppm. By means of comparing to experiments at higher temperatures, the 203 ppm peak can be identified as the signal related to xenon on a smooth surface. In contrast the 156 ppm peak has not yet been seen. Since the shift is mainly due to electron influences the 156 ppm peak must be connected to atoms located at sites with less neighbors than in a smooth surface, for example at an edge of an island in an incomplete layer.

By means of the depolarization pulse before the RIDE sequence the amount of signal giving nuclei is well defined. Regarding the shown spectra in fig. 5.1 the signals must arise from the first 4.4, 2.5, 0.9, 0.5 topmost layers of the film. With increasing measuring rates, polarized interior layers have less time to grow. Therefore, the bulk signal at 320 ppm is reduced with increased measuring rate.

If the growth mechanism was layer-by-layer then this should be seen in the topmost graph by the signal at about 320 ppm which is related to xenon at a bulky site. 3 of the 4 layers should have fully coordinated xenon atoms, however the ratio of the bulk signal strength to surface signal strength is clearly not 3:1. So the effective surface must be greater than expected which, again, can be explained by a rough surface. This means that the island edges are not a hint for the least detectable amount of nuclei since it is neither known how many islands are formed nor how they are stacked on each other. Strictly spoken, further investigations are imperative to prove the location of the xenon. Thus 'edge xenon' is not more than a label up to this point.

At 25 K the xenon atoms are so immobile that the peaks at 156 ppm and 203 ppm can be resolved. By heating the xenon film diffusion on the surface is introduced and at a temperature between 40 K and 45 K the sites cannot be distinguished anymore, as it can be seen in figure 5.2.

Motional Broadening

The molecule dynamic is too slow to narrow the 156 ppm and 203 ppm lines. Instead the motion leads to a broadening. If an exchange between two different ensembles is assumed, respective to the two corresponding frequencies, the coalescence can be discussed by the theory described in section 2.3. However, equation (2.51) cannot be applied since the linewidth is considerably broad due to other influences, probably dipole dipole interactions. Further, figure 5.2 suggests that the populations of the respective ensembles differ. So, a more general formulation of eqn. (2.51) is necessary when parameters, like the exchange rate between the ensembles, shall be determined by fitting of a suitable function to the graph. The broadening by the dipole interaction and the molecule motion cannot be distinguished however. The fitting algorithm prefers the one effect or the other, according to which start parameters are given. Thus no estimates are given here.

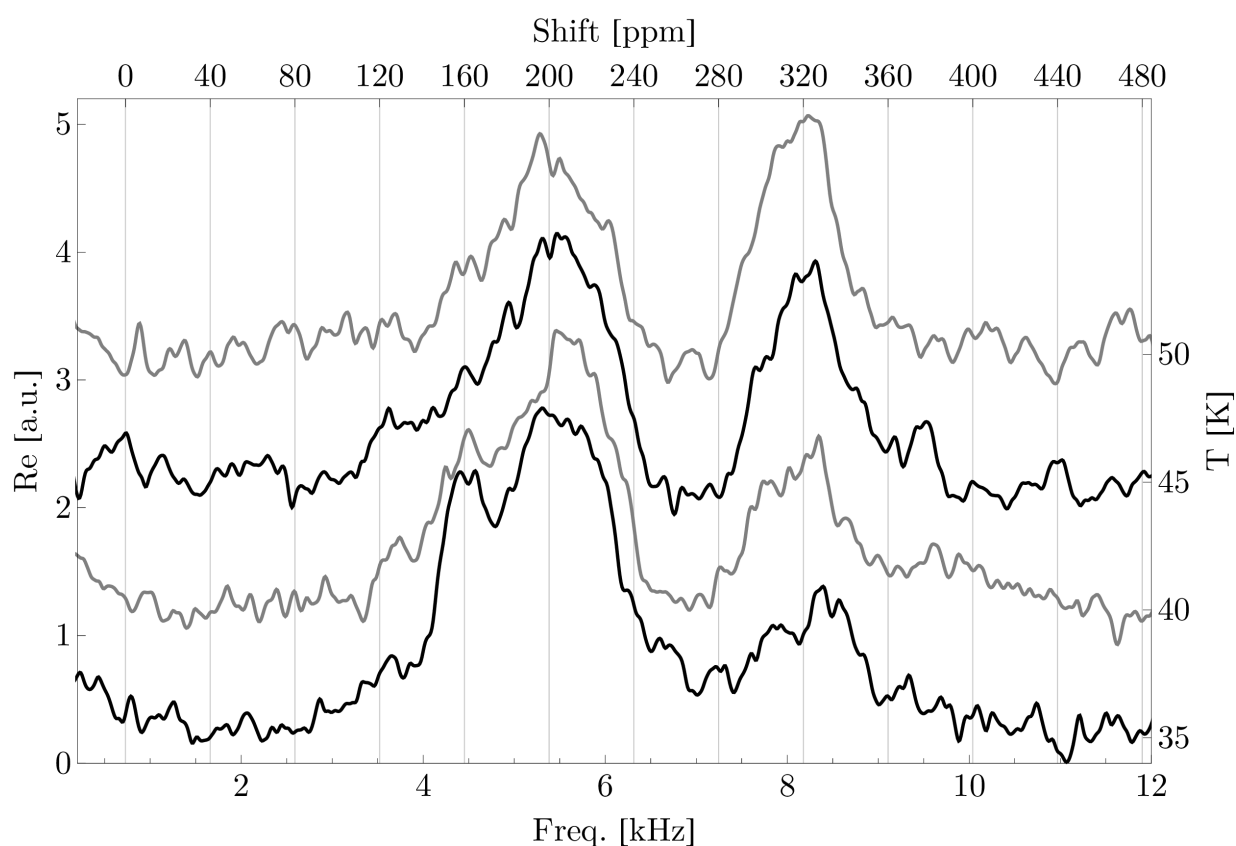


Figure 5.2: Xenon dosed on graphene/Ir(111) with 4 ML/s. The acquisition rate is kept constant at 2.1/sec. The substrate temperature changed in the runs as indicated at the right side. For each curve 900 spectra were averaged approximately. The curves were shifted vertically by equal steps for clarity.

Fast Dosage

Finally the experiment was performed with the fast dosage and the result is shown in fig. 5.3. This way demands for an increase of the measuring rate because of the ten times shorter dosing period. In order to save time, the depolarization pulse was left out which causes an exaggerated bulk signal ^b. Heating periods and delays after were included albeit no heating current was active.

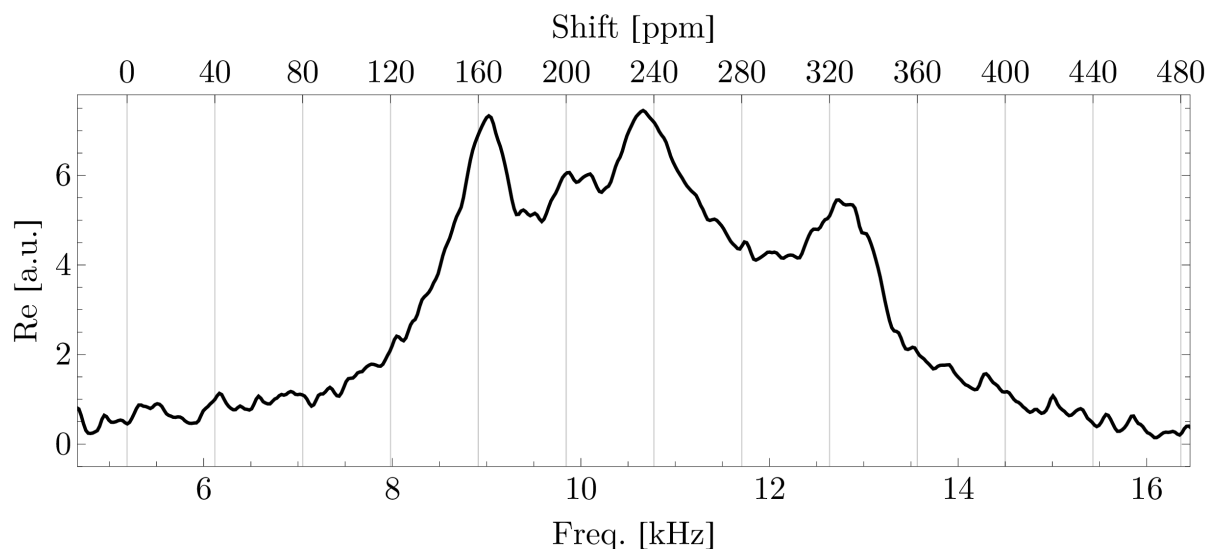


Figure 5.3: Xenon dosed on a xenon film at 32 K substrate temperature. Dosage: 40 ML/s by liquid Ar cooled xenon reservoir. Measuring rate: 8.2 spec./sec. without depolarization pulse. To show that all peaks are B-field dependent the B-field is changed slightly, so that the resonance frequencies are shifted by 4.4 kHz. The ppm scale is shifted accordingly. The origin of the signal at 235 ppm is unidentified in contrast to the other signals.

Under the present conditions the peak corresponding to the island edges is shifted to 165 ppm whereas the smooth surface peak at about 200 ppm and the bulk peak at approx. 320 ppm remain at their known positions. In contrast a new peak at 235 ppm emerges whose origin is not understood so far. Chemical shift variations due to differently coordinated xenon atoms could be the reason. A support for this idea can be found in [75] where ^{129}Xe shifts are simulated for various Xe cluster sizes. For instance, 160 ppm corresponds to a Xe_7 cluster (6 neighbors) and 240 ppm corresponds to a Xe_{10} cluster (9 neighbors).

^bThe repetition loop of the NMR sequence has regular breaks for the data transfer from the spectrometer card to the PC. During these breaks, xenon accumulates more than it does during the pauses within the NMR sequence runs. Thus, the first spectrum after a break contains an exaggerated bulk signal.

5.2 Xenon Crystal Structure

It is known that xenon solid growth mode is dependent on the substrate [76, 77], for example layer by layer growth can be found on graphite. Thereby and on many other substrates, xenon films are often filled with imperfections [78, 79]. However, heat treatments showed a beneficial effect on the crystal structure.

Here it is tested if the crystallinity can be improved by annealing. Therefore, an analysis of the spectral linewidth is made. Since the linewidth in a crystalline or microcrystalline solid of fcc structure is mainly dependent on the nuclear dipole-dipole interaction the ^{129}Xe are strongly diluted by spinless ^{132}Xe . This way, for instance polarization dependent effects on the linewidth are suppressed and influences of crystal structure changes are emphasized. The expected influence of the isotopic abundance of ^{129}Xe in the used mixture and its polarization can be seen in figure 5.4.

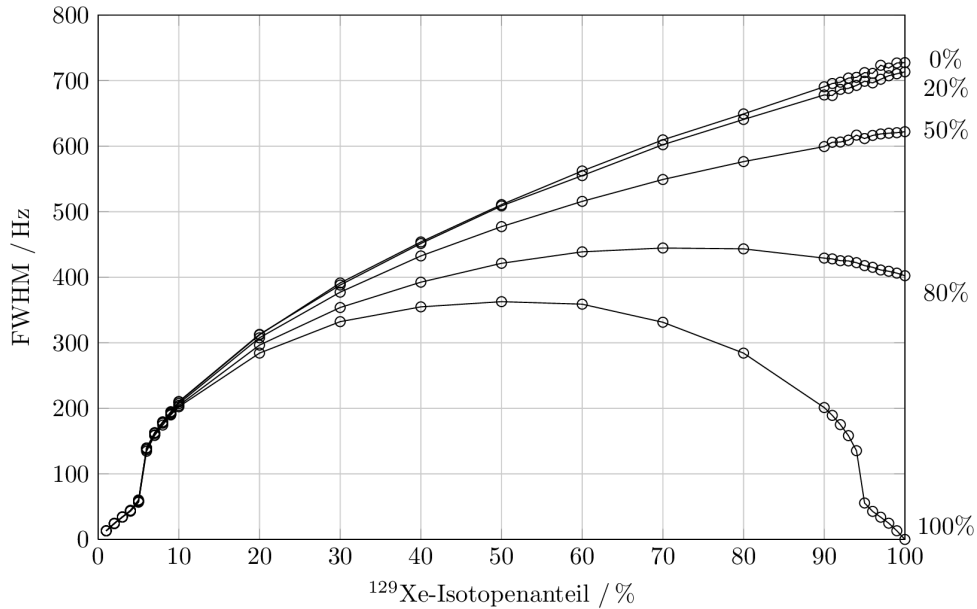


Figure 5.4: Simulated linewidth dependence on isotope abundance and polarization (written on the right ordinate) of ^{129}Xe in a $^{129}\text{Xe}/^{132}\text{Xe}$ mixed crystal. This picture was taken from [80].

5.2.1 Experiment

^{129}Xe was polarized as usual (described in section 3.8) in the optical pumping cell whereas ^{132}Xe was kept in the bobble (see fig. 3.6). The bobble was immersed into liquid N_2 so that the ^{132}Xe was frozen when the pumping cell was connected to the bobble. It was waited

until the bobble heated up again. This way the gases mixed. The transfer to the sample crystal was performed as usual^c with N₂ backfilling and an 'instant dosage' of the xenon (i.e. thawing by removing the coolant) onto the substrate.

By application of small angle pulses for the readout the FID's were recorded. Then the sample was heated to a certain temperature and cooled down again. The maximum temperature was increased gradually and after each step NMR spectra were acquired to examine the linewidth and the spectral position.

As a check, a stacked film was build, by first absorbing a film of ¹³²Xe and then the same amount of ¹²⁹Xe onto the substrate.

5.2.2 Results and Discussion

The first mixed film was grown on graphene on Ir(111). The lines of the real parts in the acquired spectra were fitted to Lorentzian functions and the respective parameters are shown in figure 5.5. At this, Δf represents the Full Width Half Maximum (FWHM) of the line and the heights are the maximum values of the Lorentzians. Δf is far narrower than in pure ¹²⁹Xe films.

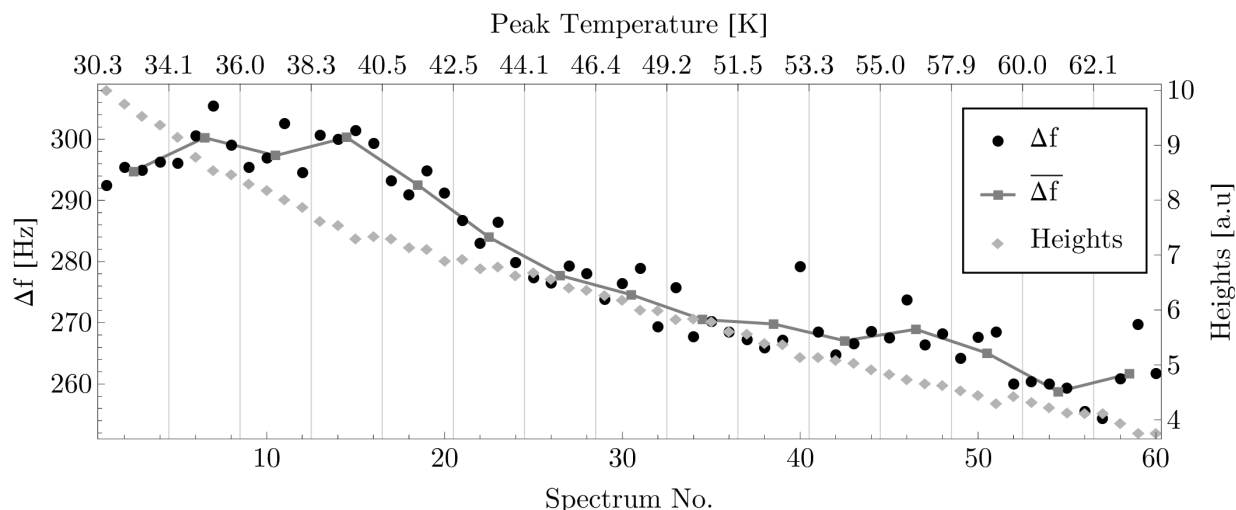


Figure 5.5: Influence of annealing on the linewidth of a ¹²⁹Xe/¹³²Xe mixed film on graphene/Ir(111) with a ¹²⁹Xe concentration of 13%. Each measurement was executed at 30 K. The film was flash annealed stepwise to the given peak temperatures.

In contrast to fig. 3.14, the line skewness is suppressed here. Thus, Lorentz functions are well suited to describe the line shape of a hyperpolarized Xe film of about 2000 layers, as it can be seen in fig. 5.6.

^cAll mentioned concentrations are affected by the uncertainties of the preparation process. No further checks on the precision of the used amounts were made.

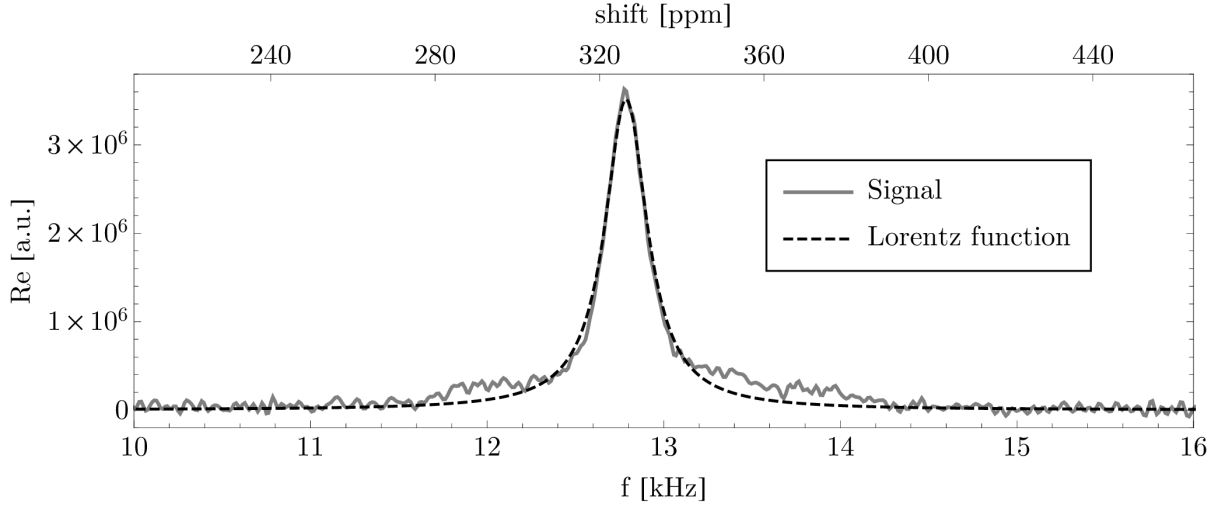


Figure 5.6: Justification for the Lorentz function fit in diluted samples. The first spectrum of fig. 5.5 and the fitted Lorentzian is shown. In contrast to fig. 3.14, the line skewness is reduced, when ^{129}Xe is present with approx. 13% isotopic abundance in the $^{129}\text{Xe}/^{132}\text{Xe}$ mixed film.

By assuming no loss of xenon in the mixing procedure, the ^{129}Xe concentration was roughly 13%. Thus, in an fcc crystal, one ^{129}Xe atom has 1.6 ^{129}Xe atoms on average in its closest neighborhood which means that dipole-dipole interactions are strongly reduced but not completely. A concentration of 13 % and the final linewidth of figure 5.5 correspond well with the respective values of the simulation, see fig. 5.4. With every measurement, polarization is lost so that dipole-dipole interaction broadens Δf . However, this effect is diminished strongly, according to the simulation. Thus, the narrowing effect must be due to an ordering process induced at temperatures above 38 K.

The decrease in the Lorentzian curve height is steady for temperatures far below 60 K which is due to the loss in polarization. But, in the vicinity of the bulk desorption temperature, the loss of magnetization also arises from the loss of xenon atoms. Because no abrupt changes in height are seen the desorption in the shown heating range seems to be uncritical.

The results for the stacked film can be seen in fig. 5.7. The first spectra show no difference in Δf from a usual 99% ^{129}Xe film.

However, heating the crystal above 38 K reveals a similar narrowing effect as it can be seen in the mixed film. Since a significant intermingling of the two films is not expected at these temperatures, the reduction in linewidth is expected to be connected to the restructuring process. The broadening by depolarization and the narrowing due to reconstruction are competing here. It is noticeable that the final $\Delta f \approx 680$ Hz corresponds well with the theoretical expectation calculated by the van Vleck formula (D.7) in appendix D.3.

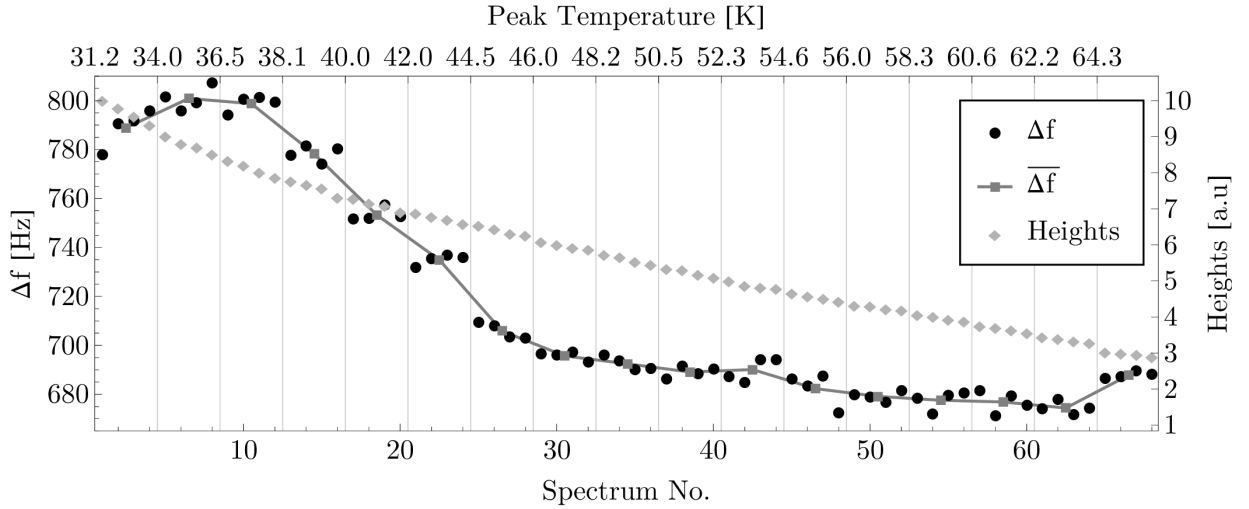


Figure 5.7: Influence of annealing on the linewidth of a $^{129}\text{Xe}/^{132}\text{Xe}$ layered film on graphene/Ir(111): The $^{129}\text{Xe}/^{132}\text{Xe}$ ratio is 1:1. Each measurement was executed at 31 K. The film was flash annealed stepwise to the given temperatures. Although the ^{129}Xe film is not diluted, a presumed ordering effect is governing the linewidth. The final linewidth is very similar to the expected value calculated in eqn. (D.7).

Because the origin of the broadening effect (the first few spectra in fig. 5.5) is still unclear the mixing experiment was repeated with a ^{129}Xe concentration of 6%. So, one ^{129}Xe has 0.7 spin carrying neighbors on average. Δf , depicted in figure 5.8, is systematically smaller due to the reduced dipole interactions. The minimum measurable linewidth could be determined to 193 Hz.

Dipole interactions are strongly suppressed here. The influence on the line broadening can be estimated by multiplying Δf , acquired by the van Vleck formula, with the ^{129}Xe isotopic abundance. Thus, the broadening by dipole interactions in the last experiment was $680 \text{ Hz} \cdot 6\% = 41 \text{ Hz}$, which is far smaller than the observed linewidth. Hence, the next strongest interactions have to be taken into account to explain the progress of the annealing.

In all three experiments a noticeable broadening effect is visible for annealing temperatures below 35 K. An increasing density of the xenon film is probably the cause. As mentioned before, a lot of defects can occur during the growth of the film and heating can 'heal' dislocations.

Heating the film to temperatures above 36 K might induce an ordering effect, best seen in the second experiment with the layered film. An increased crystallinity is connected to more uniform fields within the film, resulting in narrower NMR lines.

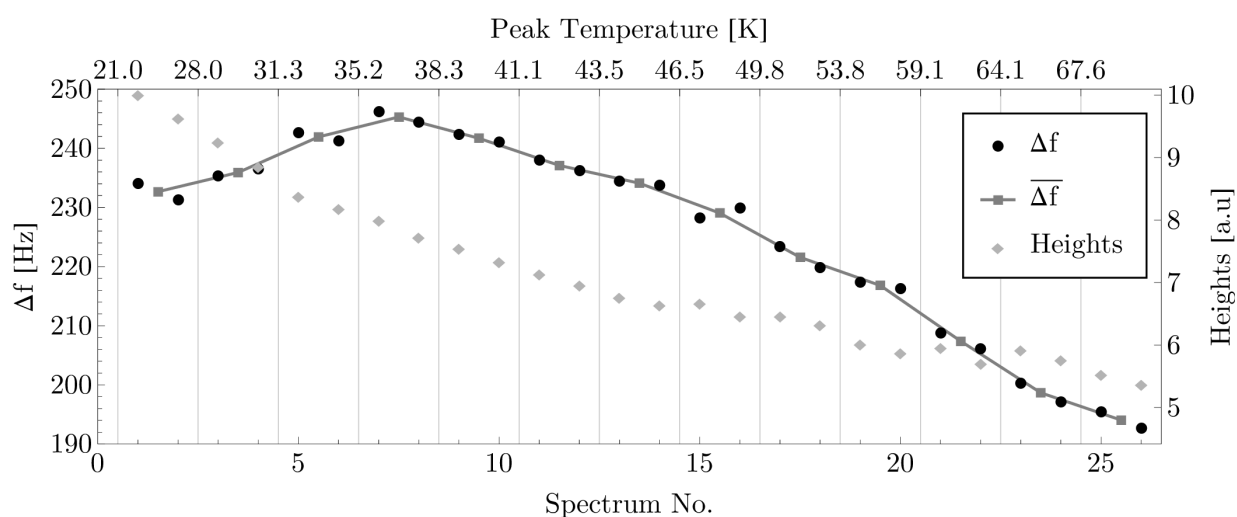


Figure 5.8: Influence of annealing on the linewidth of a $^{129}\text{Xe}/^{132}\text{Xe}$ mixed film on Cu(100) with a ^{129}Xe concentration of 6%: Each measurement was executed at 21 K. The film was flash annealed stepwise to the given temperatures.

Chapter 6

Conclusion

Xenon monolayers adsorbed on three different samples, prepared on well defined metal single crystal surfaces, were studied by NMR with hyperpolarized ^{129}Xe as the probe. The monolayer coverage was adjusted by a constant adsorption rate, defined by the polarized ^{129}Xe dosage, of 40 ML/s and the desorption that was varied by the sample temperature. During the dynamic exchange, repetitive NMR measurements were performed and the spectra were averaged to increase the signal-to-noise ratio.

The first sample was a carbon monoxide layer adsorbed on Cu(100). An NMR signal of ^{129}Xe in Xe/CO/Cu(100) was found. It was shifted by 164 ppm, with respect to the xenon gas line, at a sample temperature of 68 K. By increasing the temperature, the signal shifted gradually to 155 ppm at 70 K.

Secondly, the NMR was performed on xenon in direct contact with Cu(100). Two signals at 687 ppm and 772 ppm shift were found in a temperature range between 84 and 100 K. It is believed that one of the peaks is connected to xenon located in the interior of an island whereas the other is on the edge. However, this cannot be stated with certainty. Further knowledge is necessary. The derived Knight shift is determined to 615 ppm which is less than 1297 ppm on Cu(111) [17]. The missing surface state on Cu(100) in contrast to Cu(111) and, thus, the reduced electron density could explain the difference.

Thirdly, xenon was probed on a graphene sheet synthesized on an Ir(111) surface. Here, the shift was 173 ppm. So, the influence of metallic electrons could not be detected. The signal was visible within a temperature scope from 84 K to 92 K. Signal strength was considerably lower than for the other specimens. It is believed that this is caused by paramagnetic centers. So far, little is known about the actual state of the graphene. It is possible that an air contamination has caused a modification.

Further, ^{129}Xe NMR experiments were performed on xenon films. At a substrate temperature of about 30 K xenon desorption was negligible. By dosing the xenon with 4 ML/s onto the substrate, the xenon film grew. During the growth process repetitive NMR measurements were performed so that only the film surface was visible. The interior layers are depolarized, and therefore undetectable, due to previous measurements. Here, three peaks were found in the spectra. A signal at 321 ppm, corresponding to the xenon bulk, and another signal at 200 ppm corresponding to the smooth film surface were already identi-

fied in other works [28, 17]. In contrast, a peak at 160 ppm was unknown till now. It is probably related to an uncompleted layer on top of the film. At a substrate temperature of 45 K the signals at 160 ppm and 200 ppm were completely coalesced. With an increased dosing rate of 40 ML/s and at a substrate temperature of 30 K, an additional signal at 240 ppm appeared. Its origin is unknown till now.

Finally, a heat induced structural change within a xenon film was observed. In order to examine this phenomenon, xenon films with isotopic mixtures of ^{129}Xe and ^{132}Xe were prepared with various ratios. These samples were annealed stepwise and analyzed by the change of their linewidths. Dipole interactions could be reduced enough so that an annealing effect was observed at each concentration studied. Even at a concentration, as low as 5% of ^{129}Xe , a line broadening effect was revealed at annealing temperatures below 35 K. So, the broadening could not be caused by dipole interactions. In contrast, annealing temperatures above 35 K made the lines narrower. It is believed that the broadening is due to an increased density that originates from the reduction of dislocations in the film structure. The narrowing could arise from an increased homogeneity of the structure.

Chapter 7

Outlook

The knowledge about the resonance frequency of ^{129}Xe on non-conducting graphene enables one to perform a double resonance experiment to transfer the polarization from ^{129}Xe to ^{13}C in graphene. In order to increase the signal intensity further, the graphene could be created from a ^{13}C enriched carbon source.

The original idea was to use a hyperpolarized xenon film as a polarization source for the graphene. In this system the ^{129}Xe layer in direct contact with the graphene would lose its polarization because of the spin transfer to ^{13}C . Before the experiment could be repeated a spin transfer from the Xe film to the contact layer has to take place. This would be achieved by spin diffusion. Since spin diffusion is dependent on the dipole interactions within the xenon solid, the examination of the crystal structure was performed in this thesis. However, spin diffusion also drives the relaxation if paramagnetic centers are present. Thereby the repolarization of the contact layer is questionable, as it has become obvious by the conducted research. An alternative approach, to polarize the contact layer, could be the dynamic exchange of the xenon in the very same fashion as it was shown.

However, the quality of the graphene must be far higher than the one in use. Avoiding paramagnetic impurities is mandatory to increase the relaxation time. In order to perform a polarization transfer by double resonance, it is a prerequisite that the transfer time is shorter than the relaxation time for both participating nuclei.

A study on relaxation of ^{129}Xe on graphene is the next step in line. At it, the quantity in question is the relaxation induced by RF, the so called relaxation in rotating frame. It is related to the relaxation time $T_{1,\rho}$ which is naturally shorter than T_2 and T_1 . Hence, by determining $T_{1,\rho}$ also a lower limit can be found for the other times.

A realization of an experiment could inherit the same technique as it has been utilized for the xenon monolayer experiments. Again, it will be necessary to perform the experiment several times to increase the SNR by signal averaging. Only the RIDE sequence, shown in figure 3.11, is in need of a small adjustment. Namely, part (II) and (IV) need to be furnished with $180^\circ_{(\pm y)}$ -pulses in the same fashion as part (I) and (III). Then all $180^\circ_{(\pm y)}$ -pulses must be reduced in amplitude and replaced by $2n \times 180^\circ_{(\pm y)}$ -pulses where n is a large natural number, varied over the experimental series. This sequence which shall be called RIDEPT is depicted in figure 7.1.

If $T_{1,\rho}$ is in the order of milliseconds, a Hartmann Hahn cross polarization experiment can be performed. Therefore, the RIDEPT can be utilized under the very same conditions as it was the case for the $T_{1,\rho}$ determination. Here, it is simultaneously deployed on the ^{129}Xe and the ^{13}C channel, respectively with the according frequencies and amplitudes. If the contact time is longer than the ring down time, then the first pulse for each part of the RIDE can be left out on the ^{13}C channel.

During a monolayer experiment the mean residence time of a xenon atom on the surface can be adjusted to a time as long as 25 ms or even longer, so that a signal can still be acquired. Further, the nuclear contact can be held long when xenon is adsorbed in form of a 2D-solid. This means that the polarization recovery of ^{129}Xe by gas exchange would be no restriction for the double resonance experiment but T_1 of ^{13}C .

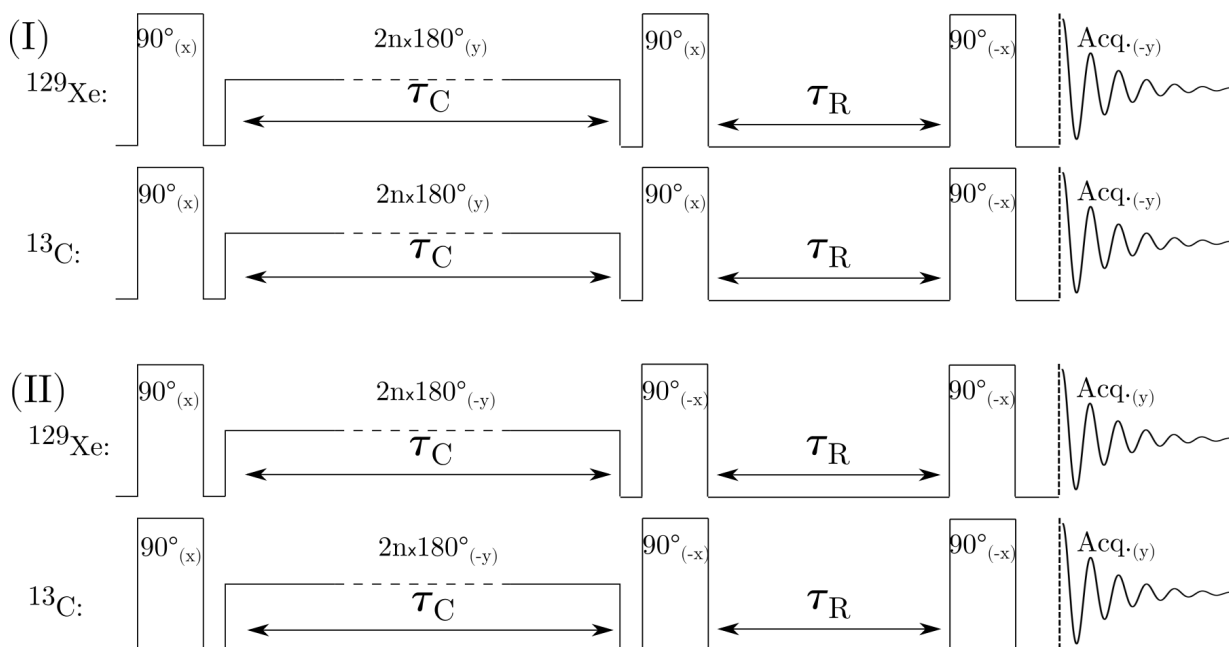


Figure 7.1: The Ring Down Elimination and Polarization Transfer (RIDEPT) sequence. τ_R is the ring down time, τ_C the spin contact time and n is a large natural number. If $\tau_C > \tau_R$ holds, the first pulse of the ^{13}C channel is optionally. In single nucleus mode, it can be also utilized for $T_{1,\rho}$ measurement.

Appendix A

Validation

A.1 Signal Validation by Field Shift

To assure that the monolayer signals of Xe/Cu(100) and Xe/graphene are really related to ^{129}Xe NMR answers the monolayer experiments were performed under respectively suitable conditions and a varied B_0 .

A.1.1 Xe/Cu(100) Monolayer Line

The experiment was conducted at 93 K at 3 different external field settings. In particular, by means of the hydrogen NMR magnetometer the field was set to a value so that the ^1H resonance is at 84.170440 MHz. This frequency, i.e. the field, was shifted by ± 20 kHz which implies a shift $\Delta f = 5.562$ kHz for ^{129}Xe . The respective results and additional details can be found in figure A.1.

Provided that the xenon is located on the substrate the signal strength must rise with decreasing frequency offset which seems to be fulfilled. On the opposite if the signal would belong to another ensemble in the background the pulses are not defined well, so the signal phase would be connected to the spacial distribution of the coil's fringe field and, on the average, the offset would not have a significant effect.

A.1.2 Xe/Graphene/Ir(111) Monolayer Line

Xenon was dosed on graphene under liquid argon cooling. The substrate temperature was 87 K. B_0 was shifted in the fashion of app. A.1.1. The expected frequencies are marked above the graphs in figure A.2. The left and the right experiments were performed with minimized offset. In contrast the center spectrum was excited at 9.6 kHz. There is also a measurement at $f_0 + 2\Delta f$ with an excitation at 9.6 kHz but this is not shown here, since no signal was found.

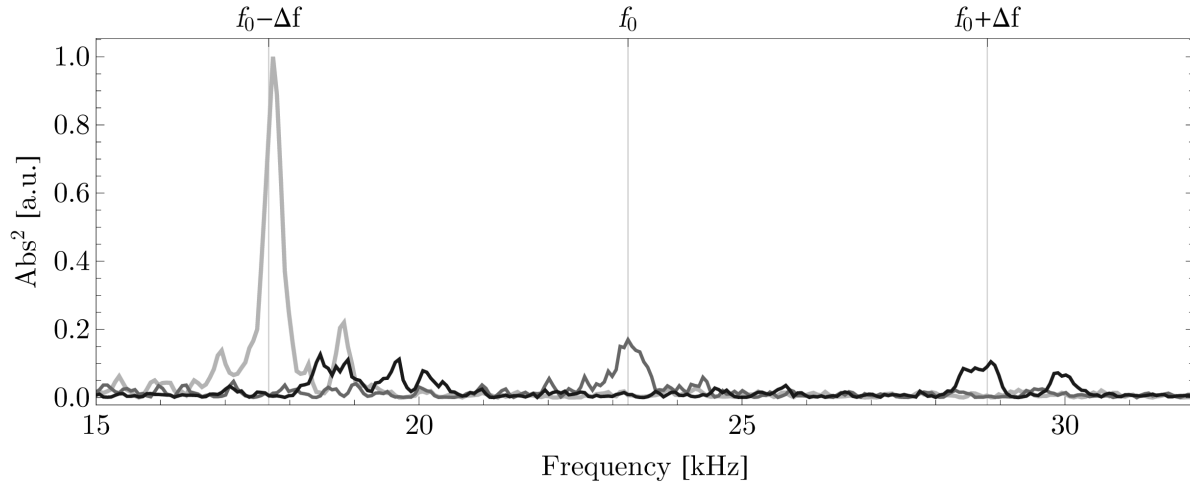


Figure A.1: Monolayer experiment on Cu(100) @ 93 K; Xe dosage: 40 ML/s –field shift. Measuring rate was 8.3 spectra per sec. For each plot between 450 and 700 spectra were averaged. f_0 was taken as the 'normal' frequency, where Δf is the calculated shift. The excitation frequency was 13 kHz for all spectra.

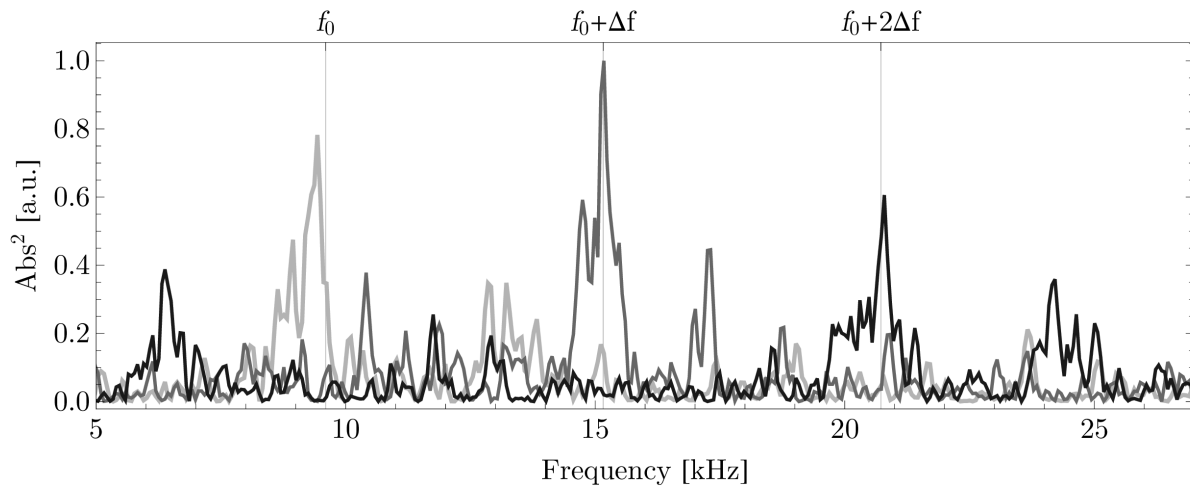


Figure A.2: Monolayer experiment on graphene @ 87 K; Xe dosage: 40 ML/s – field shift. The left-most curve was acquired by measuring 10.4 spectra per second, the others by 8.3 spectra per second.

A.2 Signal Validation by Repetition

A.2.1 Xe/Cu(100)

The monolayer experiment was performed under comparable conditions like in section 4.2.1. Here the excitation frequency was set to 13 kHz instead of 23 kHz which should lead to a loss in signal strength at most. The results are shown in figure A.3 and it can

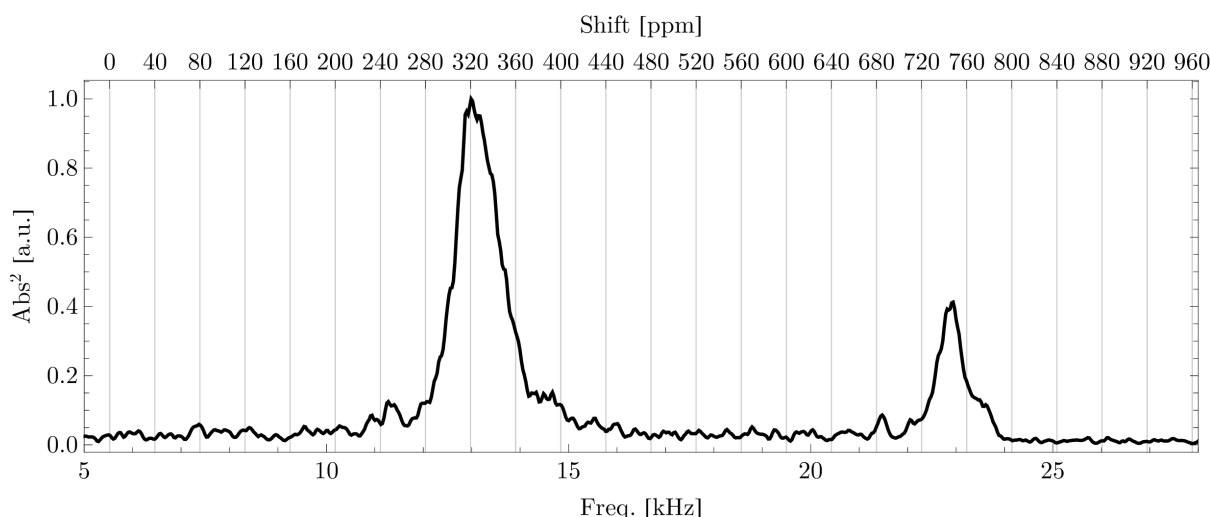


Figure A.3: Monolayer experiment on Cu(100) @ T=91...98 K; Xe dosage: 40 ML/s –freq. shift. Mean over the temperature range. Excitation frequency: 13 kHz.

be seen that one of the monolayer signals could be reproduced although slightly moved to less shift of about 770 ppm. The other signal originally found at 690 ppm appears only vaguely here. In addition it is slightly down shifted.

Also the second layer regime was probed an additional time, where the excitation frequency was set from 13 kHz to 23 kHz. As it can be seen from figure A.4 the line shift to 230 ppm could be reproduced. Here, it is noticeable that a small hint for the signal at 680 ppm is present.

A.2.2 Xe/graphene

Graphene was synthesized another time. Also here the sample was exposed to air. In a similar manner to the experiment shown in fig. 4.12 a temperature range was measured by means of monolayer Xe NMR. The external field was set to a different value and thus the frequency is shifted. The signal at 170 ppm could be reproduced, albeit with the same low signal intensity. Additionally, a hardly reproducible signal at 120 ppm can be seen.

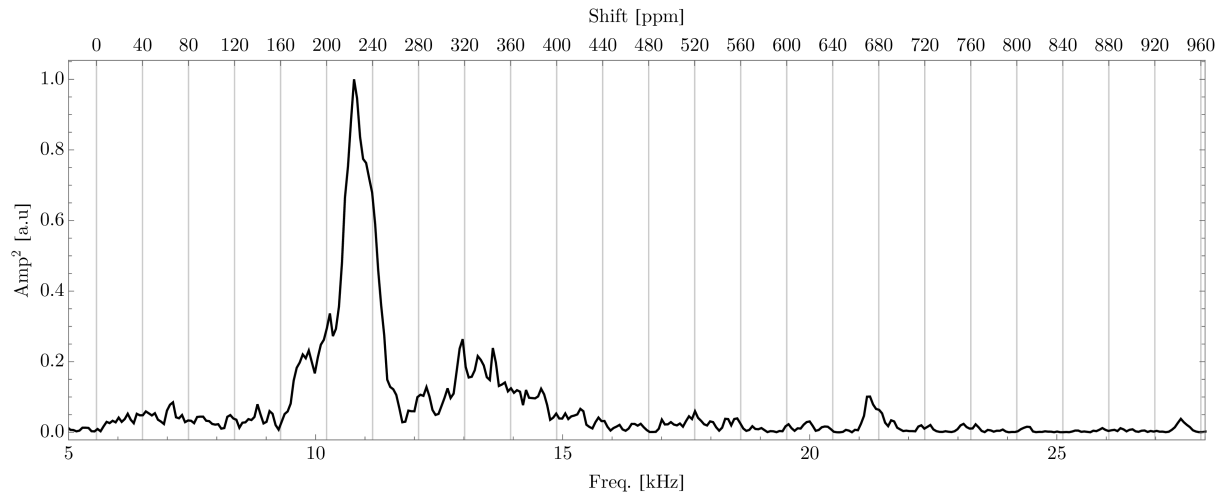


Figure A.4: 2nd layer examination on Cu(100) @ T=69 K; Xe dosage: 40 ML/s –freq. shift. Excitation frequency: 23 kHz.

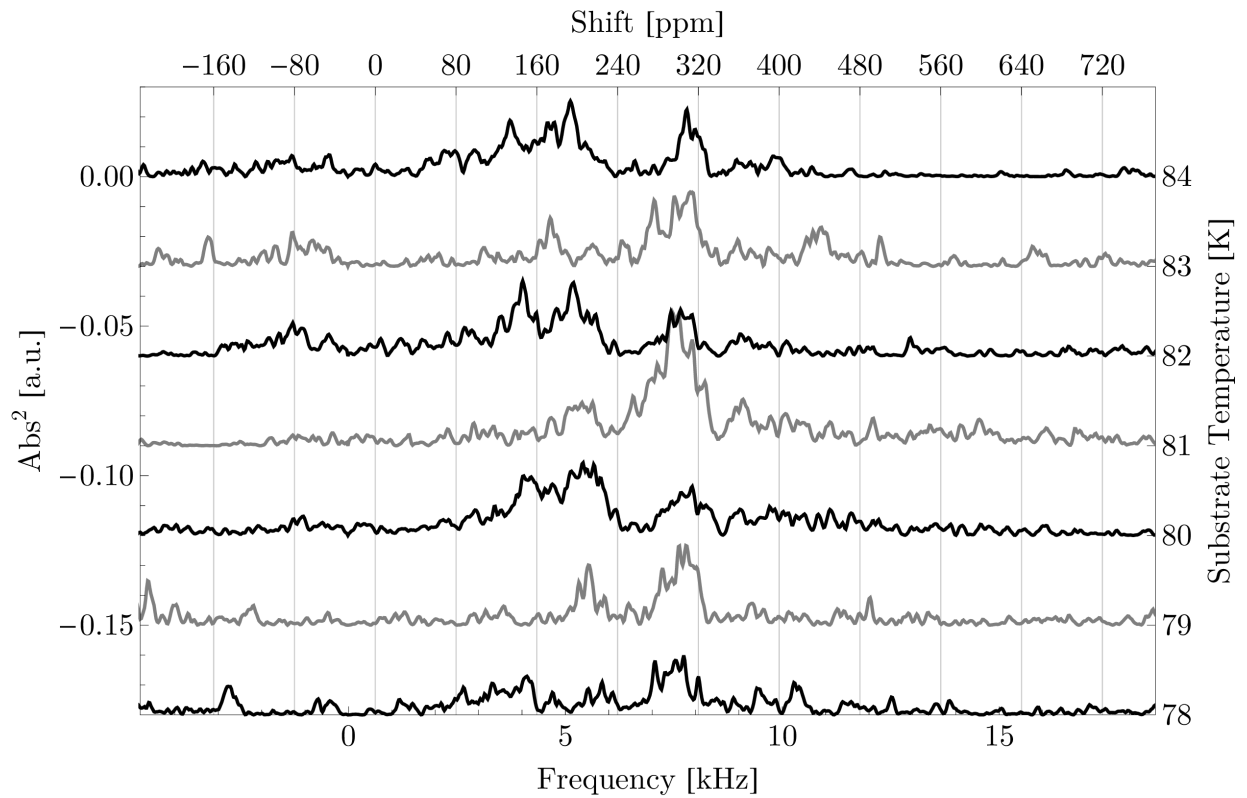


Figure A.5: Monolayer experiment on graphene @ T=78...84 K; Xe dosage: 40 ML/s. This graphene is newly synthesized.

Appendix B

Accuracy of Measurements

B.1 Xe/Cu(100) Second Layer Line

The signal of the second xenon layer on Cu(100) was fitted to a Lorentz function shown in the fig. B.1. Firstly the sample holder peak was fitted to a Lorentzian and subtracted from the spectrum. Another Lorentzian was secondly fitted to the resulting difference spectrum. Since the right peak is thought to be connected to the sample holder, only the other one is discussed. Derived from the fit parameters for the surface peak the broadness was determined to $\text{FWHM} = (579 \pm 10)$ Hz and the center frequency was $f_0 = (11041 \pm 7)$ Hz. Hence, the shift was calculated to $\sigma = 235.2 \pm 0.3$ ppm.

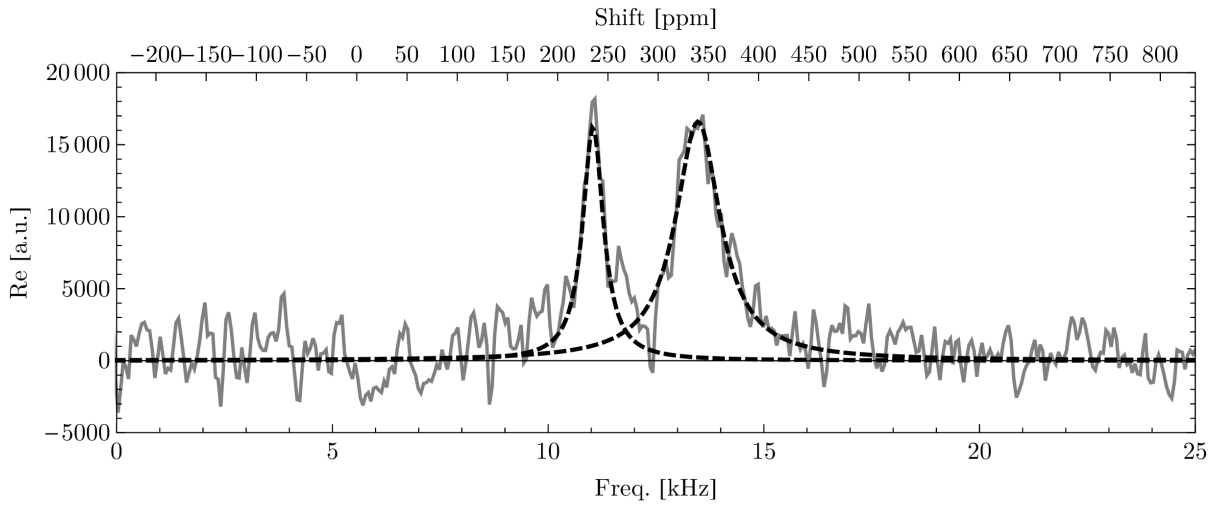


Figure B.1: Xenon dosed with 40 ML/sec. on Cu(100) at 70 K. The data are fitted to Lorentz functions.

B.2 Xe/Graphene/Ir(111) Monolayer Line

By the very same procedure as in appendix B.1 the xenon monolayer signal on graphene was surveyed. The spectrum at 90 K was taken from the temperature range shown in figure 4.12. In figure B.2 the result of the fitting procedure is given. The left peak is the signal of interest, whereas the right one is again the sample holder peak. From the parameters of the Lorentz line fitted to the monolayer peak can be determined: $f_0 = (9264 \pm 3)$ Hz, corresponding to $\sigma = 172.7 \pm 0.3$ ppm and the FWHM = (181 ± 9) Hz.

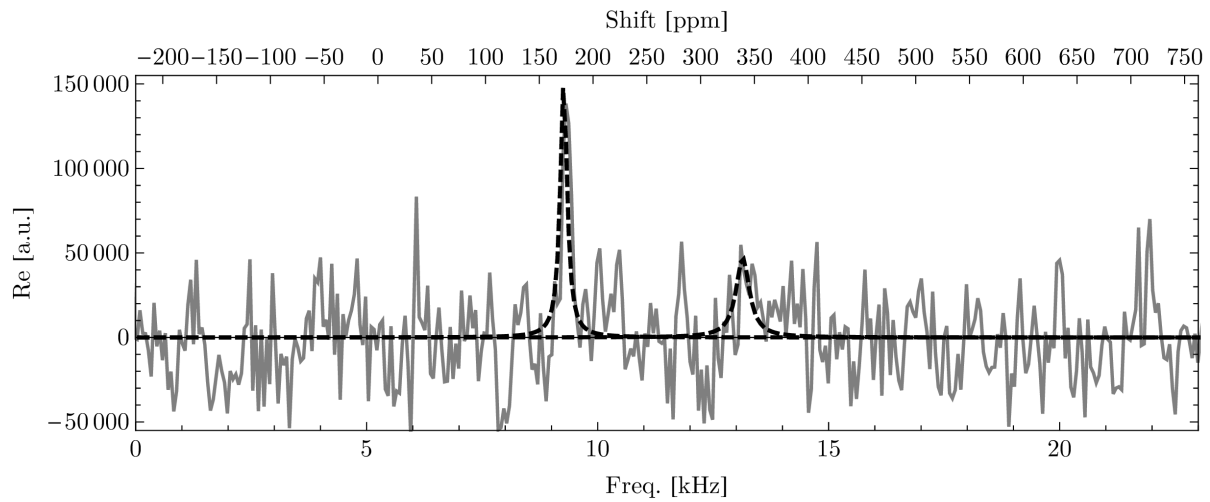


Figure B.2: Xenon dosed with 40 ML/sec. on graphene. The spectrum was acquired at 90 K. The data are fitted to Lorentz functions.

Appendix C

Setup Imperfections

C.1 Temperature Measurement

The stated temperatures in this work are not calibrated and given as measured. Additionally, it must be noted that these values are not consistent for several reasons.

Firstly, the attachment of the thermocouples to the sample crystals was executed in differing ways. In particular, the thermowires were clamped in a small copper wire connected to the copper crystal in a distance of 2 cm whereas the connection was established by laser welding directly on the iridium crystal. So, the measured temperatures are dependent on the substrates in use. They can be calibrated respectively, by means of the recorded TPD's.

Secondly, the thermoelectric power is dependent on the applied magnetic field [81], especially in the used temperature range. For our setup a temperature of 28.0 K at $B = 0$ T corresponds to 26.4 K at $B = 2$ T. This means in particular that indicated values in the TPD spectra differ from the ones of NMR experiments. The creation of a correspondence table for several temperatures was not feasible with the present setup.

C.2 Background Signal

In the regime of strong desorption from a sample surface, dosing xenon under liquid argon cooling generates a xenon film on the cold areas of the sample holder. This xenon film is still polarized because the measuring rate is usually chosen smaller than the adsorption rate of 40 ML/sec. Additionally, the effective pulse angles at the position of the sample holder are less than on the sample surface. The signal of the xenon on the sample holder is immanently acquired in NMR monolayer experiments under these circumstances.

To avoid wrong conclusions, an experiment was performed at 70 K on the Cu(100)-surface while xenon is dosed with 40 ML/sec. The measurement was executed in two ways: Firstly with the RIDE sequence, and, secondly with a simple 90°-pulse-and-readout sequence. At this, parameters like preparation, acquisition rate, the number of averaged spectra, and spectral resolution are kept similar for comparison. The results, depicted in

figure C.1, show clearly the suppression of the 340 ppm-peak which is most probable due to dephasing because of badly defined 90° - and 180° -pulses used in the RIDE sequence at the site of the xenon ensemble. This can only be possible if the sample is located outside the homogeneous field volume of the coil which hence means that the xenon does not stick to the tungsten clamp but, more probable, on the copper ingots.

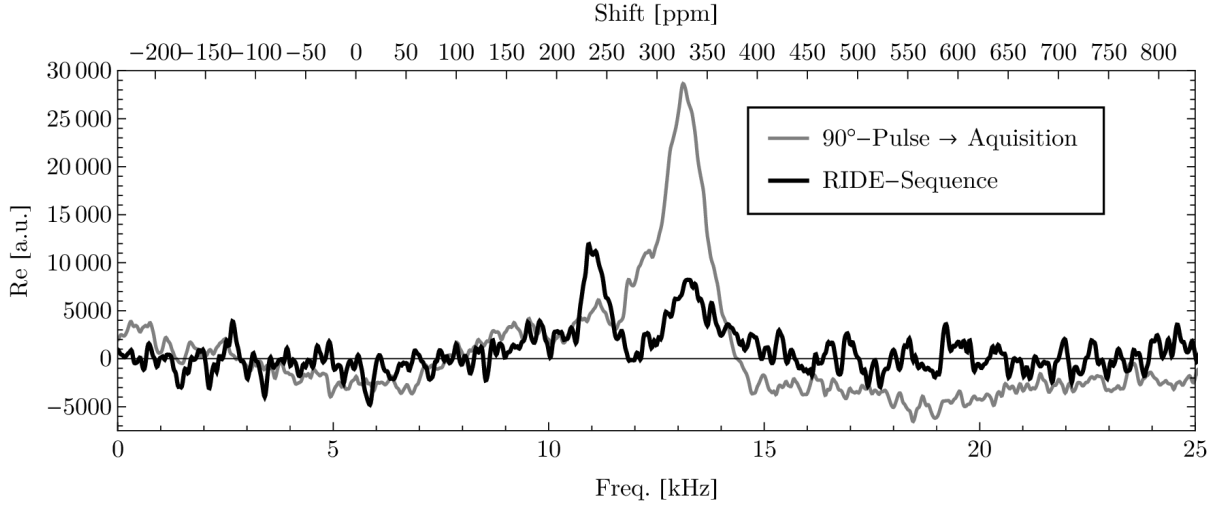


Figure C.1: Comparison of a simple readout-pulse-sequence and the RIDE sequence. Xenon was dosed with 40 ML/sec. on Cu(100) at 70 K. The measuring rate was approximately 8 spec./sec.. 144 spectra are averaged per graph. The obvious difference in the noise levels is not understood.

In the face of adversity the 'holder-peak' provides some beneficial informations after all, i.e. the shape of the peak is a measure for fluctuations of the experimental conditions per run. Especially the rise and fall of the xenon flow can be identified, which improves the credibility of other signals.

Appendix D

Supplementary Materials

D.1 Synthesis of Graphene

Firstly, the Ir(111)-surface was cleaned by several sputter- and annealing cycles. Each sputter step was performed for 20 min., with Ar^+ ions accelerated by 1200 V resulting in an ion current of about $2 \mu\text{A}$, while the crystal temperature was kept at (900 ± 20) K. Shortly afterwards, the crystal was heated up to (1200 ± 10) K for 20 min. The cleanliness was checked by TPD during randomly chosen breaks between the runs. A satisfying result could first be achieved after increasing the ion energy to 1400 eV.

Secondly, graphene was synthesized. For this, the crystal temperature was held in a range between 1050 and 1100 K. For 600 sec. ethylene (C_2H_4) was led into the chamber so that the background pressure (measured with the usual ion gauge) reached $(4.3 \pm 0.2) \cdot 10^{-8}$ mbar^a. Then the crystal temperature was increased to (1220 ± 5) K for 2 min. To assure a complete coverage the procedure was repeated two more times, but with dosing times of about 320 sec. and 180 sec. respectively.

Afterwards the sample was unavoidably exposed to air due to a setup imperfection. I.e. the heating limit of the sample is determined by the WRe-wire clamping the sample crystal. Because of its resistance it is the hottest spot in the environment. Unfortunately by the long and high heating periods the WRe-wire is deformed in such a way that the crystal turns loose which results in a movement of the crystal, a bad heat conduction, and a tension at the welding spot of the thermo wires. To prevent consecutive damage the grip has to be re-established before further usage. Thus, the vacuum chamber has to be opened and baked out as well.

^aBefore the dosage the background pressure was $2.3 \cdot 10^{-8}$ mbar and afterwards $1.6 \cdot 10^{-8}$ mbar. For comparison the pressure at about 1000 K was $5.5 \cdot 10^{-10}$ mbar before the cleaning procedure. The reason is unknown.

Since graphene was synthesized three times and the clamps lost their grip every single try the deformation is assumed not to be an accident. Nevertheless, the graphene synthesis was performed this way because on the one hand, graphene is known [82] to be stable in air, assuming graphene is created well and on the other hand the reconstruction of the sample holder is expected to be more sophisticated.

Nevertheless, by heating the crystal up to 1000 K for 5 min. the cleanliness could be restored.

D.2 Estimation of Adsorption/Desorption Equilibria

In order to perform a ^{129}Xe -NMR monolayer examination, equilibrium coverages have to be found while the xenon is dynamically exchanged. The effective adsorption rate was found to be $R_A = 40 \text{ ML/s}$ in earlier works [28] and here no difference in the sticking coefficient could be noticed. Hence, this rate is accepted. The highest signal strength within a monolayer experiment is expected, when the adsorption rate R_A is equal to the desorption rate R_D . Since R_A is fixed by the xenon vapor pressure in the cool trap, R_D is modified by adjusting the sample temperature till the equilibrium is reached.

Suitable temperatures T can be found by performing TDS and making an estimate by means of desorption theory. In particular, desorption is described by the Polanyi-Wigner equation. In first order it is given by

$$\frac{dn}{dT} = \frac{\nu}{\beta} n \exp\left(\frac{-E_d}{R T}\right) \quad (\text{D.1})$$

where n is the number of desorbing particles, ν the pre-exponential factor, β the heating rate, E_d the desorption enthalpy and R the ideal gas constant. In this case, the formula introduced by Readhead [83]

$$E_d = RT_p \left[\ln\left(\frac{\nu T_p}{\beta}\right) - 3.64 \right] \quad (\text{D.2})$$

can be applied by utilizing T_p , the temperature where desorption is at max. Under equilibrium conditions the desorption rate

$$R_D = \frac{dn}{dT} \underbrace{\frac{dT}{dt}}_{=\beta} = \nu \exp\left(\frac{-E_d}{R T}\right) \quad (\text{D.3})$$

is independent of the particles residing on the surface. Rearranging this, the temperature

$$T = \frac{T_p \left[\ln\left(\frac{\nu T_p}{\beta}\right) - 3.64 \right]}{\ln(\nu/R_D)} \quad (\text{D.4})$$

can be estimated at a given desorption rate R_D rate. Here $\nu = 10^{13}/\text{s}$ is a sufficient assumption.

D.3 Calculation of the Linewidth in a Rigid Xenon Solid

The effect on the resonance line shape induced by dipole interactions can be treated by means of the method of moments, which is explained elsewhere [38, 33]. One characteristic feature is the line broadening described by the second moment $\langle \Delta\nu^2 \rangle_{\text{Av}}$ of the spectral line. Van Vleck [84] has derived the physical connection between the nuclear dipole-dipole interaction and the second moment. For a rigid crystal powder sample, consisting of only one spin carrying nuclear species, the second moment can be calculated by

$$\langle \Delta\omega^2 \rangle_{\text{Av}} = \frac{3}{5} \left(\frac{\mu_0}{4\pi} \right)^2 \gamma_I^4 \hbar^2 I(I+1) \sum_{k \neq j} \frac{1}{r_{j,k}^6} \quad (\text{D.5})$$

where $r_{j,k}$ is the dislocation vector pointing from the position of a representative spin ' j ' to all other spins, denoted with ' k ', in the sample. Norberg and Yen [85] calculated the sum for a powder of fcc crystal and achieved

$$\sum_{k \neq j} \frac{1}{r_{j,k}^6} = 7.225 \, n_s^2 \, f \quad (\text{D.6})$$

with n_s , the atomic number density, and f , the concentration of probe nuclei. Because of symmetry the fcc single crystal is similar to a crystal powder. Therefore, the equation is used to model a ^{129}Xe film as it is created for our purposes. So, let the quantities be $I = 1/2$, $f = 99\%$, $\gamma_I = -7.4521 \cdot 10^7 \text{ rad/T}$ and the density for a xenon film at 30 K: $n_s = 17.25 \text{ atoms/nm}^3$ [56]. Within this thesis the FWHM is utilized to express the linewidth which is determined by assuming a Gaussian line shape. Presuming thermal polarization, the FWHM can be calculated by

$$\text{FWHM} = 2\sqrt{2 \ln 2} \sqrt{\langle \Delta\omega^2 \rangle_{\text{Av}}} / (2\pi) = 679 \text{ Hz}. \quad (\text{D.7})$$

D.4 Temperature Dependent Polarization Measurement

The nuclear polarization must be determined at least once on each sample to extrapolate, by means of the shift, the final frequency of a depolarized xenon film. This frequency can be used as the reference in subsequently acquired spectra. In earlier works [28, 17] the xenon solid line was found at 321 ppm shift regarding the gas line. As a convention in this thesis the frequency of a depolarized xenon solid at a temperature at 30 K is set to 321 ppm and can serve as a secondary standard.

The following measurement is one among many. It is known that the polarization varies from experiment to experiment because of a manifold of technical issues. During other experiments a constant polarization is desirable, in order to associate signal loss with physical phenomena different from preparation faults. Nevertheless, signal strengths prove to be reproducibly high which is why discrepancies in the estimation of the polarization may be assumed. The most suspicious point of criticism is the assumption of structural parameters. Hence, the temperature and polarization related behavior of the ^{129}Xe resonance line in solid xenon is studied.

D.4.1 Experiment

The substrate in use is the iridium crystal covered by graphene. Before the experiment the crystal was cleaned by heating at 800 K for 15 minutes.

Then 99% pure ^{129}Xe was polarized, in the fashion described in sec. 3.8, and transferred onto the substrate with an 'instant dosage' explained in sec. 3.9. The xenon film with a few thousands of layers was probed by the repetitive application of a simple NMR sequence, consisting of a small tip angle pulse and the readout. 100 spectra were taken in 44 seconds. Afterwards the film was desorbed by heating to 300 K.

The same procedure was performed several times at various sample temperatures. Except for the lowest used temperature, the sample was heated by chopped power supply. Not until the substrate crystal had reached its equilibrium temperature, the respective NMR experiments were started. The temperature fluctuated with $\Delta T = 0.5$ K around the set values when heating was applied whereas the experiments with only cooling were precise to $\Delta T = 0.2$ K.

All other conditions, including gas amounts in the preparation process, were tried to be kept as similar as possible.

D.4.2 Evaluation

Each acquired spectrum was fitted to a Lorentz function to determine the respective momentary center frequency. Following this, the thus resulting frequency ranges were respectively fitted to exponential asymptotes. The procedure was chiefly the same as in section 3.12 and the results are shown in figure D.1.

D.4.3 Discussion

Since the results are highly complicated due to many influences, figure D.1 is given as is. Many effects from the solid, i.e. nuclear dipole dipole interactions, varying film density, varying susceptibility effects, and probably imperfections of the setup or the evaluation algorithm cover the expected behavior of the course of the line shift. In order to make precise statements about the temperature dependent line shift, firstly a method needs to be applied that suppresses some of the effects.

D.5 Comments on the SEOP Setup

This section provides experiences and advises for working with the optical pumping setup which is shown in figure 3.6.

Special attention is given to the stop cocks which lead to small leakages when moved. Therefore, a differentially pumped volume, the upper part, is designed which improves the cleanliness of the working part, on the lower level, greatly. Additionally, the usage of gaskets made of Ethylene Propylene Diene Monomer rubber (EPDM), a polymer that is otherwise unsuitable in high vacuum applications, becomes feasible. In order to close the

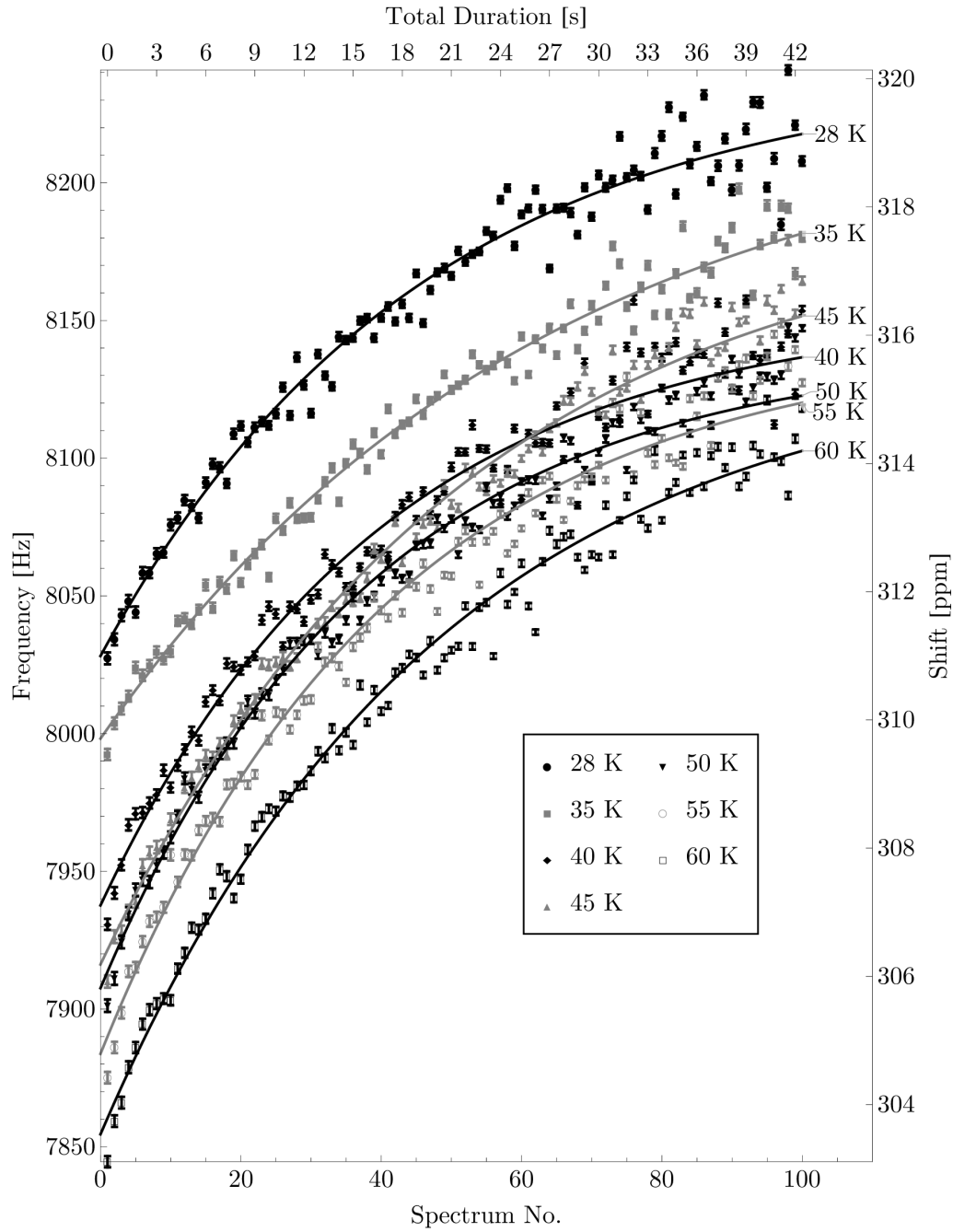


Figure D.1: Line shift dependent on temperature and polarization in (almost) similar xenon films with 99% ^{129}Xe partition; the data points represent the respective centers of the Lorentzians fitted to the NMR lines in the stepwise acquired spectra. Error bars represent the fit uncertainties. Continuous lines are the fits of the fits. Against the obvious down shift of the series with temperature, the range of 45 K ends up with a higher frequency than the one of 40 K. It should be mentioned that they are not mixed up. Temperature dependent (electron) susceptibility effects of the substrate or the xenon film and the density dependent chemical shift contribute to the offsets but not to the slope of the curves.

pumping cell an EPDM O-ring is used because of its chemical resistance against the highly reactive rubidium vapor. For the remaining sealings viton O-rings are used. All gaskets are lubricated with high vacuum grease consisting of a silicone compound. The lifetimes of a rubidium filled optical pumping cell exceed more than 20 months.

The optical pumping cell is heated by an oven that, in turn, is fed by hot silicone oil. Typically, the oil temperatures are regulated to 115°C which correspond to a cell temperature of approximately 100°C.

The precision of the used gas amounts is limited by the calibration of the pressure gauge and the unknown temperature distribution. Further the mixing behavior of the gases is not well controlled. Nevertheless, the pumping process proves to be robust against moderate changes. The polarization process suffers mainly from an instable laser intensity or a varying cell temperature. As long as the cell is held in thermodynamic equilibrium, i.e. even the room ventilation has to be controlled, the laser power of 2 W measured at the output of the Ti:sapphire laser is sufficient to polarize the used amounts of xenon greatly above the thermodynamic equilibrium.

Typically, the center frequency of the laser is adjusted by irradiating the pumping cell filled with pure rubidium vapor, i.e. no nitrogen and no quenching. If the D_1 line is hit, the rubidium luminescence can be seen. But even if this condition is not fulfilled precisely, the SEOP process can still work because of the line broadening effect of the N_2 . The crucial criterion for successful SEOP is rather a low light transmission of the pumping cell, while the Helmholtz field is shut down, whereas the transmission is high with an operating Helmholtz coil. The transmission power range for a filled cell in a magnetic field is dependent on the amount of xenon used. For high amounts as 8 mbar a low transmission is expected. On the contrary, a low amount like 2 mbar leads to a high transmission. Without the Helmholtz field, transmission gets invisible to the power meter which is then dominated by the thermal radiation of the oven housing.

SEOP works better when the rubidium vapor is dispersed uniformly throughout the cell. This can be achieved by a reasonable preparation: When a droplet of rubidium is put into the cell, then the volume shall be closed and heated, for example with a hot air blower, far above the usual working temperature, so that the rubidium evaporates strongly. Once the cell cools down again the vapor covers the glass walls. The procedure should be repeated till a metallic glance appears. In our case the heating is limited by the service temperature of the EPDM gasket, that is about 130 °C. However, a wet piece of cloth wrapped around the sensitive area provides a sufficient cooling. The same trick works well to compensate the side effects of the metalization, namely the unwanted coverage of the laser windows. In a second step the cylinder barrel of the cell should be wrapped up in wet cloth, whereas the windows are heated again. This way the rubidium migrates from the hottest to the coldest surfaces, so that the windows become transparent again. It can be necessary to check the transmission with the laser before and after the preparation.

D.6 Probe Head Double Resonance Extension Box

The single resonance probe head, described in section 3.6.2 can be extended to perform double resonance experiments. Therefore, a circuit box, as it can be seen in fig. D.2, is interconnected by cable. In the box the capacitors are *Arco Glimmer Trimmers*. All housings are made of aluminum.

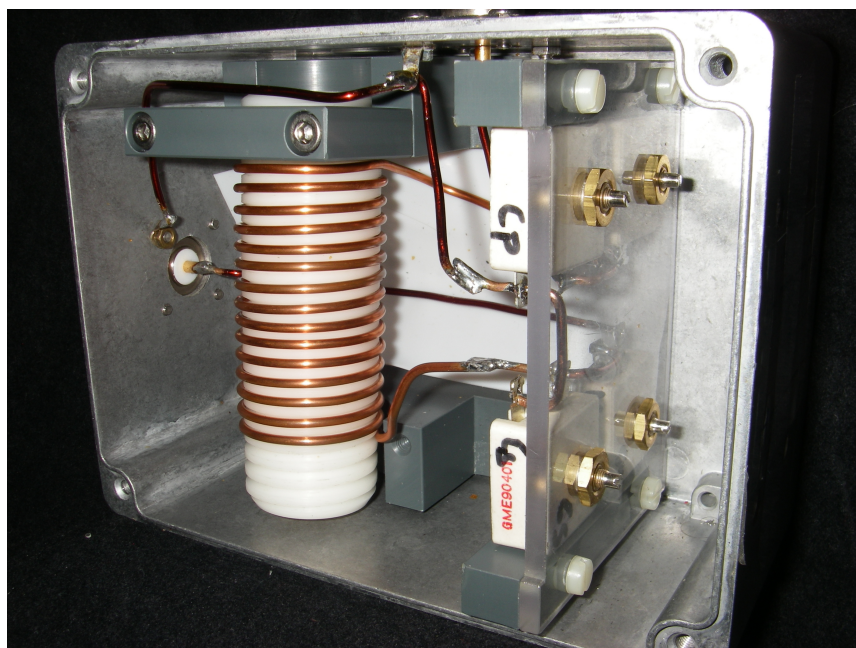


Figure D.2: Double resonance mode extendable circuit box

In principle the augmented probe head is depicted in fig. D.3. An estimate for the

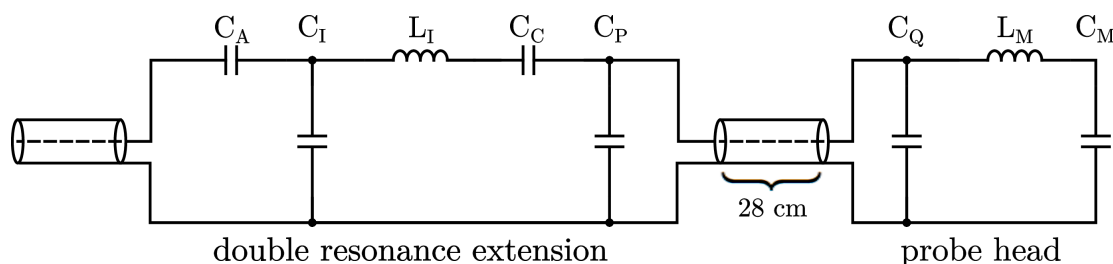


Figure D.3: Principle of the NMR probe head including the double resonance extension box

inductances can be calculated by the formula [86]

$$L/\text{nH} = \frac{22n^2 \cdot (d/\text{cm})}{1 + 22/10 \cdot (l/\text{cm})/(d/\text{cm})} \quad (\text{D.8})$$

whereat n is the number of windings, d is the diameter of the bore, and l the total length. This formula is valid for coils in which the distances between the wires and the wire diameter have the same size. A solution for this network can be found by estimating the dimensions

of the components and assuming preconditions, i.e. the total impedance must be set to 50Ω at a given frequency. An example estimate, calculated by means of a least square optimization algorithm, is given in table D.1. When the second resonator circuit is not

	Sum	Double Resonance Extension						Cable	
	Z_{ges}	C_A	C_I	L_I	R_I	C_C	C_P	C_K	L_K
quant.	50Ω	35 pF	126 pF	$3.6 \mu\text{H}$	1Ω	14 pF	17 pF	20 pF	50nH
U_{max}/V	141	550	600	7500	13	6600	1300	250	50
I_{max}/A	3	3	11	13	13	13	4	1	14

	Probe Head			
	C_Q	L_M	C_M	R_M
quant.	95 pF	$2.9 \mu\text{H}$	16 pF	1Ω
U_{max}/V	1300	7000	6300	15
I_{max}/A	20	15	15	15

Table D.1: An estimated realization of the probe head: Component names are related to the ones used in fig. D.3. The cable is assumed to be a combination of capacitors and coils with total capacity C_K and total inductance L_K respectively. The probe is impedance matched to 50Ω , simultaneously for $f_1 = 23.275 \text{ MHz}$ and $f_2 = 25.742 \text{ MHz}$. For L_I and L_M are assumed resistances connected in series. All estimated or set values are highlighted gray.

necessary it can be simply dislodged for a better performance. Therefore, the capacity C_Q must be increased to 700 pF so that the circuit is approximately resonant to 23.275 MHz.

Certainly, the given estimate is only one of many solutions. Disregarded influences, e.g. of the housings, were reconsidered in the realized range of the variable capacitors.

Bibliography

- [1] E. M. Purcell, H. C. Torrey, and R. V. Pound. Resonance Absorption by Nuclear Magnetic Moments in a Solid. *Phys. Rev.*, 69:37–38, Jan 1946.
- [2] F. Bloch, W. W. Hansen, and Martin Packard. Nuclear Induction. *Phys. Rev.*, 69:127–127, Feb 1946.
- [3] W. G. Proctor and F. C. Yu. On the Nuclear Magnetic Moments of Several Stable Isotopes. *Phys. Rev.*, 81:20–30, Jan 1951.
- [4] R. L. Streever and H. Y. Carr. Nuclear Magnetic Resonance of Xe^{129} in Natural Xenon. *Phys. Rev.*, 121:20–25, Jan 1961.
- [5] HC Torrey. Chemical Shift and Relaxation of Xe-129 in Xenon Gas. *Physical Review*, 130(6):2306–&, 1963.
- [6] D Lazdins, M Karplus, and CW Kern. Chemical Shifts in Xenon Fluorides. *Journal of Chemical Physics*, 39(6):1611–&, 1963.
- [7] Cynthia Juan Jameson and H. S. Gutowsky. Calculation of Chemical Shifts. II. The Xenon Fluorides. *The Journal of Chemical Physics*, 40(8):2285–2293, 1964.
- [8] D. Brinkmann and H.Y. Carr. Local Magnetic Field Shift in Liquid and Solid Xenon. *Physical Review*, 150(1):174–179, 1966.
- [9] T Ito and Jacques Fraissard. NMR study of the interaction between xenon and zeolites A, X and Y. In *Proceedings of the 5th International Conference on Zeolites*, 01 1980.
- [10] S. Ishi and B. Viswanathan. Adsorption of xenon atoms on metal surfaces. *Thin Solid Films*, 201(2):373–402, 1991.
- [11] J.-Ph. Ansermet, C.P. Slichter, and J.H. Sinfelt. Solid state NMR techniques for the study of surface phenomena. *Progress in Nuclear Magnetic Resonance Spectroscopy*, 22(5):401–421, 1990.
- [12] William Happer. Optical Pumping. *Rev. Mod. Phys.*, 44:169–249, Apr 1972.
- [13] B. C. Grover. Noble-Gas NMR Detection through Noble-Gas-Rubidium Hyperfine Contact Interaction. *Phys. Rev. Lett.*, 40:391–392, Feb 1978.

- [14] H. J. Jänsch, P. Gerhard, and M. Koch. ^{129}Xe on Ir(111): NMR study of xenon on a metal single crystal surface. *Proceedings of the National Academy of Sciences of the United States of America*, 101(38):13715–13719, 2004.
- [15] W. Jacob, V. Dose, U. Kolac, Th. Fauster, and A. Goldmann. Bulk, surface and thermal effects in inverse photoemission spectra from Cu(100), Cu(110) and Cu(111). *Zeitschrift für Physik B Condensed Matter*, 63(4):459–470, Dec 1986.
- [16] A. Hotzel. *Femtosekunden-Elektronendynamik der Adsorbatbedeckten Cu(111)-Oberfläche*. PhD thesis, Freie Universität Berlin, 1990.
- [17] M. Koch. *NMR-Experimente auf metallischen Einkristalloberflächen*. PhD thesis, Philipps-Universität Marburg, 2006.
- [18] K. S. Novoselov, A. K. Geim, S. V. Morozov, D. Jiang, Y. Zhang, S. V. Dubonos, I. V. Grigorieva, and A. A. Firsov. Electric Field Effect in Atomically Thin Carbon Films. *Science*, 306(5696):666–669, 2004.
- [19] Matthias Batzill. The surface science of graphene: Metal interfaces, CVD synthesis, nanoribbons, chemical modifications, and defects. *Surface Science Reports*, 67(3):83–115, 2012.
- [20] T. Shibanuma, H. Asada, S. Ishi, and T. Matsui. NMR of Xe Adsorbed on Graphite. *Japanese Journal of Applied Physics part 1-Regular Papers Short Notes & Review Papers*, 22(11):1656–1658, 1983.
- [21] G. Neue. A Xe-129 NMR-study of Xe Layers on Graphon. *Zeitschrift für physikalische Chemie Neue Folge*, 152(1-2):13–22, 1987.
- [22] D Raftery, H Long, T Meersmann, PJ Grandinetti, L Reven, and A Pines. High-field NMR of adsorbed xenon polarized by laser pumping. *Physical Review Letters*, 66(5):584, 1991.
- [23] D. Raftery, L. Reven, H. Long, A. Pines, P. Tang, and J. A. Reimer. Spin-polarized xenon-129 NMR study of a polymer surface. *The Journal of Physical Chemistry*, 97(8):1649–1655, 1993.
- [24] Dong Jin Suh, Tae Jin Park, Son Ki Ihm, and Ryong Ryoo. Xenon-129 NMR spectroscopy of xenon gas adsorbed on amorphous carbons. *The Journal of Physical Chemistry*, 95(9):3767–3771, 1991.
- [25] P.A. Simonov, S.V. Filimonova, G.N. Kryukova, E.M. Moroz, V.A. Likholobov, T. Kuretzky, and H.P. Boehm. ^{129}Xe NMR study of carbonaceous materials: effects of surface chemistry and nanotexture. *Carbon*, 37(4):591–600, 1999.

- [26] K.V. Romanenko, A. Fonseca, S. Dumonteil, J.B. Nagy, J.-B. d’Espinose de Lacaillerie, O.B. Lapina, and J. Fraissard. ^{129}Xe NMR study of Xe adsorption on multiwall carbon nanotubes. *Solid State Nuclear Magnetic Resonance*, 28(2):135–141, 2005. Special issue in honor of Prof. Jerzy Blicharski.
- [27] M. S. Syamala, R. James Cross, and Martin Saunders. ^{129}Xe NMR Spectrum of Xenon Inside C60. *Journal of the American Chemical Society*, 124(21):6216–6219, 2002. PMID: 12022857.
- [28] Peter Gerhard. *Konventionelle Puls-NMR an ^{129}Xe auf Einkristalloberflächen*. PhD thesis, Philipps-Universität Marburg, 2004.
- [29] Johann Coraux, Alpha T N’Diaye, Martin Engler, Carsten Busse, Dirk Wall, Niemma Buckanie, Frank-J Meyer zu Heringdorf, Raoul van Gastel, Bene Poelsema, and Thomas Michely. Growth of graphene on Ir(111). *New Journal of Physics*, 11(2):023006, 2009.
- [30] Alpha T. N’Diaye, Sebastian Bleikamp, Peter J. Feibelman, and Thomas Michely. Two-Dimensional Ir Cluster Lattice on a Graphene Moiré on Ir(111). *Phys. Rev. Lett.*, 97:215501, Nov 2006.
- [31] Johann Coraux, Alpha T. N’Diaye, Carsten Busse, and Thomas Michely. Structural Coherency of Graphene on Ir(111). *Nano Letters*, 8(2):565–570, 2008. PMID: 18189442.
- [32] M.H. Levitt. *Spin Dynamics: Basics of Nuclear Magnetic Resonance*. Wiley, 2001.
- [33] A. Abragam. *The Principles of Nuclear Magnetism*. International series of monographs on physics. Clarendon Press, 1961.
- [34] O. Tsyplatyev and D. M. Whittaker. Dipolar broadening of nuclear spin resonance under dynamical pumping. *Phys. Rev. B*, 85:125123, Mar 2012.
- [35] Alexander Potzuweit. *Nuclear dipole interactions in solid Xe-129 measured with NMR*. PhD thesis, Philipps-Universität Marburg, 2015.
- [36] Dan Raftery and Bradley F. Chmelka. Xenon NMR Spectroscopy. In Bernhard Blümich, editor, *Solid-State NMR I Methods*, pages 111–158, Berlin, Heidelberg, 1994. Springer Berlin Heidelberg.
- [37] C.J. Jameson, D.N. Sears, and A.C. de Dios. The Xe-129 nuclear shielding tensor surfaces for Xe interacting with rare gas atoms. *Journal of Chemical Physics*, 118(6):2575–2580, FEB 8 2003.
- [38] C.P. Slichter. *Principles of Magnetic Resonance*. Springer Series in Solid-State Sciences. Springer Berlin Heidelberg, 1996.

- [39] G. Schatz and A. Weidinger. *Nuclear Condensed Matter Physics: Nuclear Methods and Applications*. Wiley, 1996.
- [40] Ch. Kittel. *Introduction to Solid State Physics, 7th Edition*. Wiley India Pvt. Limited, 2007.
- [41] G.C. Carter, L.H. Bennett, and D.J. Kahan. *Metallic shifts in NMR: A review of the theory and comprehensive critical data compilation of metallic materials*. Number Bd. 1 in Progress in materials sciences. 20,1-4. Pergamon Press, 1977.
- [42] J.D. Jackson. *Classical Electrodynamics*. Wiley, 2012.
- [43] H.A. Lorentz. *The Theory of Electrons and Its Applications to the Phenomena of Light and Radiant Heat*. B.G. Teubners Sammlung von Lehrbüchern auf dem Gebiete der mathematischen Wissenschaften mit Einschluss ihrer Anwendungen. G.E. Stechert & Company, 1916.
- [44] Thad G. Walker and William Happer. Spin-exchange optical pumping of noble-gas nuclei. *Rev. Mod. Phys.*, 69:629–642, Apr 1997.
- [45] Graham Norquay, Steven R. Parnell, Xiaojun Xu, Juan Parra-Robles, and Jim M. Wild. Optimized production of hyperpolarized ^{129}Xe at 2 bars for in vivo lung magnetic resonance imaging. *Journal of Applied Physics*, 113(4):044908, 2013.
- [46] Thomas Meersmann and Eike Brunner, editors. *Hyperpolarized Xenon-129 Magnetic Resonance*. New Developments in NMR. The Royal Society of Chemistry, 2015.
- [47] Yuan-Yu Jau, Nicholas N. Kuzma, and William Happer. High-field measurement of the ^{129}Xe – Rb spin-exchange rate due to binary collisions. *Phys. Rev. A*, 66:052710, Nov 2002.
- [48] K. Borer and G. Frémont. The nuclear magnetic resonance magnetometer type 9298. *Nuclear Instruments and Methods*, 154(1):61–82, 1978.
- [49] M. L. Buess and G. L. Petersen. Acoustic ringing effects in pulsed nuclear magnetic resonance probes. *Review of Scientific Instruments*, 49(8):1151–1155, 1978.
- [50] Eiichi Fukushima and S.B.W Roeder. Spurious ringing in pulse NMR. *Journal of Magnetic Resonance (1969)*, 33(1):199–203, 1979.
- [51] Gareth A Morris and Michael J Toohey. Removal of “acoustic ringing” from NMR spectra. *Journal of Magnetic Resonance (1969)*, 63(3):629–633, 1985.
- [52] I.P. Gerathanassis. Methods of avoiding the effects of acoustic ringing in pulsed fourier transform nuclear magnetic resonance spectroscopy. *Progress in Nuclear Magnetic Resonance Spectroscopy*, 19(3):267–329, 1987.

- [53] Peter S. Belton, I. Jane Cox, and R. K. Harris. Experimental sulphur-33 nuclear magnetic resonance spectroscopy. *J. Chem. Soc., Faraday Trans. 2*, 81:63–75, 1985.
- [54] Malcolm H Levitt. Composite pulses. *Encyclopedia of nuclear magnetic resonance*, 2:1396, 1996.
- [55] D. Candela, M. E. Hayden, and P. J. Nacher. Steady-State Production of High Nuclear Polarization in ^3He - ^4He Mixtures. *Phys. Rev. Lett.*, 73:2587–2590, Nov 1994.
- [56] Gerald L. Pollack. The Solid State of Rare Gases. *Rev. Mod. Phys.*, 36:748–791, Jul 1964.
- [57] U. Bardi, A. Glachant, and M. Bienfait. Phase transitions on stepped and disordered surfaces: Xe adsorbed on Cu and NaCl single crystal surfaces. *Surface Science*, 97(1):137–157, 1980.
- [58] J.A. Venables, H.M. Kramer, and G.L. Price. Observation of an adsorbed monolayer by transmission high energy electron diffraction. *Surface Science*, 55(1):373–379, 1976.
- [59] L W Bruch, Milton W Cole, and Hye-Young Kim. Transitions of gases physisorbed on graphene. *Journal of Physics: Condensed Matter*, 22(30):304001, 2010.
- [60] L. Zhao, K.T. Rim, H. Zhou, R. He, T.F. Heinz, A. Pinczuk, G.W. Flynn, and A.N. Pasupathy. Influence of copper crystal surface on the CVD growth of large area monolayer graphene. *Solid State Communications*, 151(7):509–513, 2011.
- [61] C.J. Jameson. Modeling Xe chemical shifts on crystal surfaces. 2003.
- [62] A. Glachant and U. Bardi. Thermodynamics and kinetics of Xe monolayer adsorption on Cu(100) by LEED and AES. *Surface Science*, 87(1):187–202, 1979.
- [63] Evanildo G. Lacerda, Jr., Stephan P. A. Sauer, Kurt V. Mikkelsen, Kaline Coutinho, and Sylvio Canuto. Theoretical study of the NMR chemical shift of Xe in supercritical condition. *Journal of Molecular Modeling*, 24(3), MAR 2018. 19th Brazilian Symposium of Theoretical Chemistry (SBQT), Aguas de Lindoia, BRAZIL, NOV 12-17, 2017.
- [64] M.A. Chesters and J. Pritchard. Leed and surface potential study of carbon monoxide and xenon adsorbed on cu(100). *Surface Science*, 28(2):460 – 468, 1971.
- [65] S. Müller, A. Kinne, M. Kottcke, R. Metzler, P. Bayer, L. Hammer, and K. Heinz. In-plane lattice reconstruction of cu(100). *Phys. Rev. Lett.*, 75:2859–2862, Oct 1995.
- [66] Alpha T N’Diaye, Johann Coraux, Tim N Plasa, Carsten Busse, and Thomas Michely. Structure of epitaxial graphene on ir(111). *New Journal of Physics*, 10(4):043033, 2008.

- [67] R. Scott Smith, R. Alan May, and Bruce D. Kay. Desorption Kinetics of Ar, Kr, Xe, N₂, O₂, CO, Methane, Ethane, and Propane from Graphene and Amorphous Solid Water Surfaces. *The Journal of Physical Chemistry B*, 120(8):1979–1987, 2016. PMID: 26595145.
- [68] Hendrik Ulbricht, Renju Zacharia, Nesibe Cindir, and Tobias Hertel. Thermal desorption of gases and solvents from graphite and carbon nanotube surfaces. *Carbon*, 44(14):2931–2942, 2006.
- [69] Oleg V. Yazyev and Steven G. Louie. Topological defects in graphene: Dislocations and grain boundaries. *Phys. Rev. B*, 81:195420, May 2010.
- [70] D. W. Boukhvalov, V. Yu. Osipov, A. I. Shames, K. Takai, T. Hayashi, and T. Enoki. Charge transfer and weak bonding between molecular oxygen and graphene zigzag edges at low temperatures. *Carbon*, 107:800–810, OCT 2016.
- [71] Hendrik Ulbricht, Gunnar Moos, and Tobias Hertel. Physisorption of molecular oxygen on single-wall carbon nanotube bundles and graphite. *Phys. Rev. B*, 66:075404, Aug 2002.
- [72] Sebastian Standop, Ossi Lehtinen, Charlotte Herbig, Georgia Lewes-Malandrakis, Fabian Craes, Jani Kotakoski, Thomas Michely, Arkady V Krasheninnikov, and Carsten Busse. Ion impacts on graphene/Ir (111): interface channeling, vacancy funnels, and a nanomesh. *Nano letters*, 13(5):1948–1955, 2013.
- [73] Li Yan, Subramaniam Dinesh, Atodiresei Nicolae, Lazić Predrag, Caciuc Vasile, Pauly Christian, Georgi Alexander, Busse Carsten, Liebmann Marcus, Blügel Stefan, Pratzner Marco, Morgenstern Markus, and Mazzarello Riccardo. Absence of Edge States in Covalently Bonded Zigzag Edges of Graphene on Ir(111). *Advanced Materials*, 25(14):1967–1972, 2013.
- [74] Toshiaki Enoki and Manabu Kiguchi. Magnetism of nanographene-based microporous carbon and its applications: Interplay of edge geometry and chemistry details in the edge state. *Phys. Rev. Applied*, 9:037001, Mar 2018.
- [75] Matti Hanni, Perttu Lantto, and Juha Vaara. Pairwise additivity in the nuclear magnetic resonance interactions of atomic xenon. *Phys. Chem. Chem. Phys.*, 11:2485–2496, 2009.
- [76] G.L. Price and J.A. Venables. Layer growth of xenon on graphite. *Surface Science*, 49(1):264–274, 1975.
- [77] H.M. Kramer. Epitaxial growth of rare gas solids. *Journal of Crystal Growth*, 33(1):65–76, 1976.
- [78] R. J. Keyse and J. A. Venables. Crystal growth and microstructures of solid krypton and xenon. *Journal of Crystal Growth*, 71:525–537, June 1985.

- [79] Y. Sonnenblick, Z.H. Kalman, and I.T Steinberger. Growth and crystal-structures of solid xenon and krypton. *Journal of Crystal Growth*, 58(1):143–151, 1982.
- [80] M. Buschmann. *Xe-129 NMR an konzentrierten und verdünnten Xe-Isotopengemischen —Konstruktion und Test einer neuen Präparationsapparatur*. Diplomarbeit, Philipps-Universität Marburg, 2011.
- [81] A.V Inyushkin, K Leicht, and P Esquinazi. Magnetic field dependence of the sensitivity of a type E (chromel–constantan) thermocouple. *Cryogenics*, 38(3):299–304, 1998.
- [82] Zhen Hua Ni, Hao Min Wang, Zhi Qiang Luo, Ying Ying Wang, Ting Yu, Yi Hong Wu, and Ze Xiang Shen. The effect of vacuum annealing on graphene. *Journal of Raman Spectroscopy*, 41(5):479–483.
- [83] P.A. Redhead. Thermal desorption of gases. *Vacuum*, 12(4):203 – 211, 1962.
- [84] J. H. Van Vleck. The Dipolar Broadening of Magnetic Resonance Lines in Crystals. *Phys. Rev.*, 74:1168–1183, Nov 1948.
- [85] W. M. Yen and R. E. Norberg. Nuclear Magnetic Resonance of Xe^{129} in Solid and Liquid Xenon. *Phys. Rev.*, 131:269–275, Jul 1963.
- [86] H.H. Meinke and F.W. Gundlach. *Taschenbuch der Hochfrequenztechnik*. Springer-Verlag Berlin Heidelberg, 5 edition, 1992.

Danksagungen

Bevor ich den guten Seelen den wohlverdienten Dank ausspreche, möchte bekräftigen, dass diese ihn auch redlich verdient haben. Dieses Projekt durchzuführen hat mich nicht nur geistig gefordert sondern auch seelisch und körperlich an meine Grenzen gebracht. Es gibt Menschen, die sich ihren Hintern versichern lassen, aber gegen Zeitverlust, den man erleidet, wenn ein experimenteller Aufbau scheinbar irreparabel zu Bruch geht, gibt es meines Wissens bis heute keine Versicherung. Es ist fraglich, ob ich diese Arbeit hätte zu Ende führen können ohne die Unterstützung der im Folgenden Genannten:

Vor Allen gebührt mein Dank meinem Doktorvater Prof. Dr. Heinz J. Jänsch. Er ermöglichte mir diese Promotion und kümmerte sich auf fürsorglichste Weise auch um das Gelingen. Die regelmäßigen Diskussionen mit ihm waren nicht nur lehrreich, sondern haben auch inspiriert und mein schon vorhandenes wissenschaftlichen Interesse noch weiter gefördert. Letztlich zeigte er sich mir gegenüber auch immer menschlich und verständnisvoll.

Prof. Dr. Kerstin Volz möchte ich dafür danken, dass sie mir die Pforten ins Graduiertenkolleg (GRK) geöffnet hat. Das GRK 1782 unter der Schirmherrschaft der Deutschen Forschungsgemeinschaft (DFG) hat mich nicht nur in meiner Entwicklung als Doktorand gefördert, sondern auch die finanzielle Grundlage geschaffen, diese Arbeit überhaupt anzutreten. Vielen Dank!

Ein spezieller Dank gilt Prof. Dr. Gregor Witte. Er erwies ich als Retter in der Not und bot mir Platz in seiner Arbeitsgruppe, als bei uns das Labor drei Monate still stand.

Im Weiteren bin ich dankbar für die tolle Zeit und die Unterstützung vieler einzelner Mitglieder der Arbeitsgruppen an diesem Fachbereich. Zu Anfang genannt seien die aktuellen und ehemaligen Mitglieder und der AG Surface NMR: Alexander Potzuweit und Anuschka Schaffner, die mich in die Laborarbeit eingeführt haben, Prof. Dr. Dieter Fick und meine Bürogenossen Hagen und Christian.

Für die lustige Atmosphäre und natürlich auch für all die Ersatzteile bin ich zu Dank verpflichtet bei den Mitgliedern der AG von Prof. Jakob, wie Sebastian Thussing und Sebastian Flade. Das gleiche gilt für die AG von Prof. Höfer, besonders für Jens Güdde und Gerson Mette und natürlich für all die anderen. Auch habe ich die Zeit in der AG Witte genossen.

Carsten Schindler hat unermüdlichen Einsatz gezeigt, die altersschwachen elektronischen Geräte im Labor in Schuss zu halten. Er und sein Team aus dem Elektroniklabor des Fachbereichs haben so manch tot geglaubtem Gerät wieder Leben eingehaucht.

Ohne den tatkräftigen Einsatz von Hermann Günther und den Spezialisten der feinmechanischen Werkstatt wäre die Arbeit im Labor angesichts all meiner Sonderwünsche wohl auch nicht möglich gewesen.

Des weiteren bin ich meiner Familie dankbar, weil sie immer an mich geglaubt haben!

Außerdem gilt ein außerordentlicher Dank Vicky und Ina, dafür dass sie mein schreckliches Kauderwelsch in ein verständliches Englisch umgewandelt hat.

Wissenschaftlicher Werdegang

- 2005 – 2013 Studium der Physik an der Philipps-Universität Marburg,
mit Abschluss Diplom
- 2009 Vordiplom
- 2013 Diplomarbeit in der AG Oberflächen-NMR (Prof. Dr. H.J. Jänsch),
Thema:
*"Konstruktion eines hochvakuumtauglichen
Einlass- und Trennsystems von Gasen für NMR-Anwendungen"*
- 2013 – 2016 Mitgliedschaft im GRK 1782: Funktionalisierung von Halbleitern
- 2013 – 2018 Promotion in der AG NMR at Surfaces (Prof. Dr. H.J. Jänsch),
Thema:
*"Xe-129 NMR Study in Xenon Monolayers and Thin Films
Adsorbed on Single Crystal Metals and Carbonaceous Ad-Layers"*